Scanning probe lithography of chemically functionalised surfaces

Scott M. D. Watson

How to cite:

Watson, Scott M. D. (2008) Scanning probe lithography of chemically functionalised surfaces. Doctoral thesis, Durham University.

Scanning probe lithography of chemically functionalised surfaces

A thesis submitted for the partial fulfilment of the requirement for the

Degree of

Doctor of Philosophy

In the faculty of Science of

Durham University

By

Scott M. D. Watson

Durham University

Department of Chemistry

University Science Laboratories

South Road

Durham

2008

Copyright

Declaration

This work was conducted in the Department of Chemistry at Durham University between October 2004 and December 2007. The work has not been submitted for a degree in this, or any other university. It is my own work, unless otherwise indicated.

"It is no use saying "we are doing our best". You have got to succeed in doing what is necessary."

- Sir Winston Churchill

"If I have seen further it is by standing on the shoulders of giants."

- Sir Isaac Newton FRS

Acknowledgements

I would like to take this opportunity to thank all the people who have contributed in some way to the work described in this thesis. First and foremost, I would like to thank my academic supervisor, Dr. Karl S. Coleman, for giving me the opportunity to conduct my research within his research group. I would also like to thank him for all his support and the valuable discussions and advice he has offered during my research. My thanks to Dr. Richard Thompson who has provided invaluable assistance throughout my research, both with training and assisting me in the use of atomic force microscopy, ellipsometry, and X-ray reflectometry instrumentation. Without this, my research would not have been possible. My thanks to Sarah Lister and Dr. John S. O. Evans for their time and assistance in carrying out X-ray diffraction studies on my behalf, which has provided a valuable contribution to my research.

I also wish to thank Dr Graham Beamson of the National Centre for Electron Spectroscopy and Surface Analysis (NCESS) at Daresbury Laboratory for technical assistance and useful discussions on XPS measurements. My thanks here are also extended to Dr Amit K. Chakraborty from Dr. Colemans research group for the many hours he spent at Daresbury Laboratory running and analysing XPS experimental data on my behalf. This work would not be possible without the financial support of EPSRC.

I would like to thank all the members of the Laboratory 108 (past and present) for all the assistance, support, and enjoyment they have brought during over the past three and a half years. Particular thanks go to Anil Suri and Pippa K. Monks with whom I have worked with from the very beginning of my PhD, through to its completion. Finally, I would like thank my family (mum, dad, Marc, nana, gran) for all the support they have given me during my PhD (and for the 23 years prior to that….)

Table of Contents

Table of Contents

Table of Contents

Figures

Figures

Figures

Schemes and Tables

Abbreviations

AFM	Atomic force microscopy
APTES	3-Aminopropyltriethoxysilane
APTMS	3-Aminopropyltrimethoxysilane
AuNPs	Gold nanoparticles
cAFM	Conductive probe atomic force microscopy
DNA	Deoxyribose nucleic acid
E-beam	Electron beam
FTIR	Fourier transform infra-red
Fwhm	Full width at half-maximum
Hf-ODP	Hafnium-octadecylphosphonate
HMDS	Hexamethyldisilazane
LB	Langmuir-Blodgett
(LC)	Liquid-compressed
Magnesia-ODP	Magnesia-octadecylphosphonate
Mg-ODP	Magnesium-octadecylphosphonate
NC-AFM	Non-contact atomic force micrsocopy
NIL	Nanoimprint lithography
ODP	Octadecylphosphonate
ODP-H_2	Octadecylphosphonic acid
OTS	Octadecyltrichlorosilane
QCM	Quartz crystal microbalance
(S)	Solid
SAM	Self-assembled monolayer
SNOM	Scanning near-field optical microscopy

SNP	Scanning near-field photolithography
SPL	Scanning probe lithography
SPM	Scanning probe microscopy
STM	Scanning tunnelling microscopy
TMS	Trimethylsilyl
UHV	Ultrahigh vacuum
UV-light	Ultra-violet light
XPS	X-ray photoelectron spectroscopy
XRD	X-ray diffraction
XRR	X-ray reflectometry
Zr-ODP	Zirconium-octadecylphosphonate

Abstract

A facile route to the production of highly uniform, ultra-thin metal oxide films has been demonstrated using a combination of self-assembly and Langmuir-Blodgett techniques. Initial modification of a Si/SiO_2 substrate through self-assembly of an octadecylsiloxane monolayer provides a hydrophobic surface suitable for the "tail-down" deposition of a Langmuir-Blodgett monolayer of octadecylphosphonic acid, giving. The resulting -PO_3H_2 functionalised film provides a suitable surface for binding of metal ions (*e.g.* Zr^{4+}, Hf^{4+}, Mg^{2+}). The tendency of these metal species to form polymeric structures in aqueous solution allows for the assembly of nanometre thick inorganic metal layers upon the -PO_3H_2 surface. Thermal treatment of the Langmuir-Blodgett films was used to decompose the organic film components, whilst simultaneously calcining the inorganic metal layer, resulting in the formation of highly uniform metal oxide films, typically *ca.* 1.3 - 1.9 nm thick.

Nanoscale patterning of the metal-stabilised Langmuir-Blodgett monolayers has also been demonstrated, by using an AFM probe to apply sufficiently high vertical forces upon the Langmuir-Blodgett surface to selectively displace the monolayer film material within spatially defined surface regions. Pattern resolutions down to 30 nm were achieved using this AFM "nanodisplacement" lithographic process. Excellent levels of structural retention of the patterns were also observed upon decomposition of the organic film components to generate the final metal oxide. Similarly, nanodisplacement patterning of metal-stabilised Langmuir-Blodgett monolayers deposited upon amino-functionalised substrates has been used for the fabrication of amine patterned surfaces. Selective binding of Au nanoparticles within the amine regions was demonstrated, highlighting the potential of such patterned surfaces as chemical templates for directing the assembly and organisation of other materials.

Chapter 1

1. *Introduction*

1.1 Aims

The focus of this study concentrates upon the development of novel, new routes to the production of chemically patterned surfaces on a nanometre-scale. Combinations of monolayer self-assembly and Langmuir-Blodgett (LB) techniques, used in conjunction with scanning probe lithography (SPL) procedures, have been investigated as a means of generating two-dimensional nanostructures. In particular, SPL techniques based upon "nanodisplacement" of substrate-supported thin films are explored, reporting the conditions required for successful spatially-resolved surface modification, and the pattern resolutions achieved (the ability to achieve sub-100 nm features is desirable, to demonstrate this methodology can offer competitive resolutions limits to other contemporary lithographic techniques available today). Furthermore, these studies will extend to exploring the potential of these chemically patterned surfaces, and the spatially defined surface properties they exhibit, towards the development of miniaturised device technologies, (*e.g.* operating as chemical templates to facilitate selective binding of materials to build up more complex functional structures).

1.2 General

One of the central challenges in contemporary science and technology is the ability to control and manipulate the organisation of matter on a nanometre scale. The fabrication of structures with such small dimensions opens up a diverse range of potential applications ranging from the production of nanoelectronic and optical devices[1,2] to the development of biosensor technologies such as DNA,[3] protein,[4] and glyco arrays.[5]

In recent years, significant advancements in nanoscale technologies have been achieved utilising a combination of "top-down" and "bottom-up" strategies. Exploiting these approaches is integral to addressing the fundamental challenges associated with the development of miniaturised devices, such as the ability to fabricate the necessary "building blocks" (*i.e.* device components) with a high level of control over structure size and morphology. The range of synthetic nanoscale materials available for such use is vast, and includes nanoparticles,[6] nanowires,[7,8] and nanotubes,[9] as well as biological molecules such as. DNA,[10] proteins,[11] sugars.[12] However, perhaps the principal challenge of device fabrication lies in the ability to manipulate, organise, and position such structures with nanoscale precision for the assembly of more complex structures with tailored functionalities. One such approach to this problem is the use of chemically patterned surfaces which can facilitate spontaneous organisation of materials upon a substrate surface. The ability to fabricate chemical "templates" which can direct the surface assembly of functional nanomaterials provides a route to the construction of more complex three-dimensional structures in a controlled fashion.

1.3 Preparation of "soft" thin films

The construction of molecular assemblies upon a solid surface has been established as a fundamental concept in the tailoring the chemical and physical properties of interfaces. The fabrication of molecular film architectures has been largely dominated by the study and development of self-assembly and Langmuir-Blodgett (LB) processes. The following section will provide a brief review of the principles behind these surface modification techniques, examining the factors influencing formation of such molecular architectures, and highlighting some of the chief developments to date, in this field.

1.3.1 Self-assembled monolayers

Self-assembled monolayers (SAMs) are highly ordered molecular assemblies formed by adsorption of a surface active compound upon a solid support.[13] The formation of these two-dimensional structures is procedurally very simple, with spontaneous assembly taking place upon exposure of the substrate surface to a solution of the surface active material.

The origins of this field of study lie as far back as 1946, when Zisman reported the spontaneous adsorption of a monomolecular layer of an alkylamine from solution upon a platinum support.[14] Since then a plethora of SAM systems have been devised, employing numerous different substrate-amphiphile combinations, most commonly (though not necessarily restricted to) using long chain hydrocarbon molecules bearing a terminal functionality which exhibits a high binding affinity to the substrate.

1.3.1.1 Phosphonic acids

Several early studies into monolayer self-assembly investigated the formation of long-chain *n*-alkanoic acid monolayers upon a range of metal oxide substrates including Al_2O_3,[15,16] AgO,[17] and CuO.[18] The assembly of such monolayers is driven by the formation of salts between the anionic carboxylate headgroups of the acid molecules and metal cations at the substrate surface. The structure of the resulting monolayers was found to be strongly dependent upon the substrate employed, due to its influence upon the binding geometry of the carboxylate groups.[19]

More recently, the preparation of SAMs of alkylphosphonic acids upon several different substrates including mica,[20] SiO_2,[21] TiO_2,[22] ZrO_2,[23] Al_2O_3[24] have also been reported. Here, the nature of the binding of PO_3H_2 headgroups to the substrate surface is found to be dependent upon the substrate used. Woodward *et al.*[20] suggested the acid-substrate interactions upon mica surfaces to be largely non-specific, with the tilted orientations of the octadecylphosphonic acid (ODP-H_2) alkyl chains (indicated from AFM analysis) suggesting symmetrical binding of the OH and O groups of the headgroups to the surface.[25] In contrast, SAM formation upon Si/SiO_2 and metal oxide substrates takes place through condensation reactions between the PO_3H_2 headgroups and surface hydroxyl groups (Equation 1), forming covalent M–O–P linkages.

$$\mathrm{RPO(OH)_2} \; + \; \mathrm{–M–OH} \; \rightarrow \; \mathrm{R(OH)OP–O–M–} \; + \; \mathrm{H_2O} \qquad (1)$$

Organophosphonate SAMs prove significantly more robust and durable than siloxane based monolayers[26] (see Section 1.3.1.3), making them a desirable option for integration into commercial applications.[27]

1.3.1.2 Organothiolates

Possibly the most extensively studied group of SAM structures are alkanethiolates upon Au surfaces, which exploit the strong binding interactions that readily take place between gold and sulphur atoms. Formation of such SAM systems was first reported by Nuzzo and Allara,[28] describing the spontaneous formation of close-packed monolayer assemblies of di-*n*-alkyl disulfides from dilute solutions upon Au substrates. Since then, a range of organosulfur compounds have been described in SAM formation upon Au substrates including di-n-alkyl sulfides,[29] thiophenols,[30] mercaptopyridines,[31] mercaptoanilines,[32] thiocarbamates,[33] cysteines,[34] and thioureas.[35]

Binding of organosulfur molecules upon the Au surface is thought to take place through an oxidative addition mechanism (Equation 2),[13] with evidence of the binding SAM species being the thiolate having been shown by XPS,[36] and FTIR studies.[37]

$$\mathrm{R{-}S{-}H} \; + \; \mathrm{Au_n}^0 \; \rightarrow \; \mathrm{R{-}S^{-}Au\cdot Au_n}^0 \; + \; {}^1\!/_2\mathrm{H_2} \qquad (2)$$

The exact nature of the mechanism of SAM adsorption is still not fully understood however and remains a source of much debate. Alternative binding species have been suggested in studies by Fentor *et al.*[38] for example suggesting dimerisation of the alkanethiolates takes place upon the Au surface, forming dialkyl disulfides.

The use of organosulfur compounds in SAM formation has not been restricted to Au surfaces, with such compounds also strongly coordinating to a variety of other metals including silver,[39] copper,[40] platinum,[41] and iron.[42]

1.3.1.3 Organosilanes

The use of organosilane compounds in surface modification strategies has received considerable interest due their compatibility with Si/SiO_2 substrates, used throughout the semiconductor industry. The preparation of monolayers using alkylchlorosilanes[43,44,45] and alkylalkoxysilanes[46] upon Si/SiO_2 substrates is well-established, with the formation of a highly crosslinked Si–O–Si network of SAM molecules bound to the substrate surface. The mechanism of SAM growth is driven by hydrolysis of the Si–X groups (X = Cl, OR). Polymerisation of the hydrolysed organosilanes, through nucleophilic substitution reactions, leads to the formation of the final crosslinked SAM adsorbed upon the substrate, Scheme 1.

The growth behaviour of organosilane monolayers has been shown by AFM and X-ray diffraction studies of OTS SAMs to take place by "island aggregation". This mechanism describes film growth taking place through the formation of islands of OTS which adhere to the SiO_2 surface, and grow together to form the final, complete monolayer.[47,48] However, FTIR and X-ray reflectivity studies have also indicated an alternative "continuous" growth mechanism, in which an incomplete monolayer of OTS molecules initially bind across the substrate surface. Binding of further OTS molecules to the substrate gradually takes place over time, forming the complete monolayer.[49] Studies by Vallant *et al.*[50] have shown the film growth to take place by both mechanisms, with increased water concentrations in the solvent favouring an island aggregation mechanism.

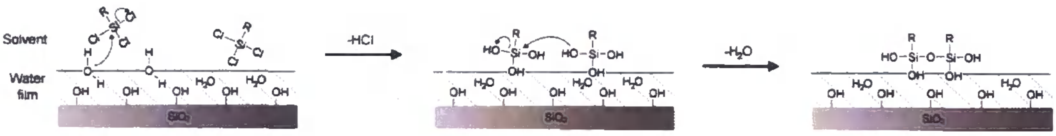

Scheme 1. Reaction scheme for the formation of OTS SAMs upon a hydrated SiO_2 surface.

The SAM structure is widely known to be strongly influenced by the solution water content, with Wasserman *et al.*[51] describing incomplete film growth of OTS SAMs in the absence of water. In contrast, SAM preparation in an excess of water promotes extensive polymerisation of the alkylsilane, forming large aggregates which bind to the substrate.[52] Studies by both Silberzan *et al.*[53] and Angst and Simmons[54] revealed the requirement for the presence of a thin water film on the silicon substrate to facilitate complete monolayer growth. FTIR studies by Tripp and Hair have since provided direct evidence of the hydrolysis of methylchlorosilanes[55] and OTS[56] upon hydrated silica surfaces, further supporting the role of such thin water films in organosilane SAM formation. These studies also revealed few Si–O–Si linkages to form between the hydrolysed OTS molecules and the SiO_2 surface.

More recently, the preparation of "ultrasmooth" OTS films was reported by Wang *et al.*[57] using dry OTS solutions in Isopar-G solvent, with film growth taking place through a "patch expansion" process (OTS SAM grows from several nucleation sites on substrate surface until a complete monolayer forms). The hydrophobicity of the solvent used was thought to help the thin water layer to remain upon the Si/SiO_2 substrate (*i.e.* restrict loss of water molecules from the substrate surface into the bulk solvent). The absence of water in the bulk solution ensures that only "free" (*i.e.* non-polymerised) OTS molecules are available for attachment to the substrate.

As well as water content, SAM formation has also been found to be sensitive to several other experimental conditions. The effect of the solvent used has been highlighted by McGovern *et al.*[58] who showed SAM growth to be influenced by a solvents ability to extract water from the hydrated silica surface (promoting OTS hydrolysis in the bulk solution). Temperature has also been shown to play an important role with OTS solutions required to be maintained below a threshold temperature (28 °C) in order to form reproducible and ordered monolayers.[53,59] Temperatures below this threshold value are believed to reduce the solubility of the alkylsilane and water molecules in the solvent, leading to an increase in their kinetics of physisorption upon the substrate.

Studies of organosilane SAMs have not been restricted to alkylsilanes, with extensive work also reported into monolayer formation using aminosilanes. The preparation of aminated silane films has attracted considerable interest from both industry and scientific research due to their ability to function as coupling agents for further modification of SiO_2 surfaces.[60,61]

Formation of the aminosilane films is again driven by silane hydrolysis, with water concentration influencing final film structure as previously discussed.[58,62] However, the bifunctional character of the aminosilane molecules leads to additional considerations in the reaction mechanism. The ability of the molecules to form zwitterions in solution for example, can lead to head-to-tail interactions of the molecules resulting in the build-up of multilayer films.[63,64] Such films are also prone to exhibit higher levels of disorder than non-aminated alkylsilane films due to the formation of hydrogen bonds between the amine and surface silanol groups.[65] The flexibility within the molecules also lends to bending of the surface bound aminosilanes such that both the head and tail groups are orientated towards the substrate surface.[66] Recently, Howarter *et al.*[62] have shown that control over amine concentration, temperature, and reaction time can be used to control the film structure, with three basic film morphologies ("smooth, thin", "smooth, thick", and "roughened thick") reported. Although surface modification using such aminosilanes remains commonly referred to as a self-assembly process, the disorder exhibited in film structures, along with their inability to self-limit film growth, suggests they should not be considered as true SAM structures.

The preparation of organosilane films discussed here so far has primarily focussed upon their preparation upon Si/SiO_2 substrates, which perhaps reflects the potential significance of such surface modifications processes to the semiconductor industry.

However, the facile nature of film formation using alkyl and aminosilanes has also seen them successfully applied to a range of alternative substrates including quartz,[67] glass,[68] aluminium oxide,[69] and mica.[46,70]

1.3.2 Langmuir-Blodgett films

The introduction of the Langmuir-Blodgett (LB) technique, as first described by Blodgett,[71,72] enables the controlled transfer of organised monolayers of amphiphilic molecules from an air-water interface to a solid substrate surface. Transfer of the monolayer film (also referred to as a "Langmuir" monolayer) is achieved through passing the substrate vertically through the monolayer supported upon the water subphase (the preparation and mechanism of formation of Langmuir and LB films is discussed more extensively in Section 2.1).

Probably the most widely employed amphiphilic molecules in Langmuir and LB films preparation have been long chain fatty acids ($C_nH_{2n+1}CO_2H$) due to their ability to form stable monolayers upon an aqueous subphase surface.[73] Investigations into the effect of structural modifications to the hydrocarbon "tails" of such fatty acids have also been widely reported. Studies by Elbert[74] for example, have shown the incorporation of fluorinated alkyl chains into the amphiphile structure can improve the monolayer stability, due to the increased hydrophobic character of the tail groups. The effects of introducing *cis* and *trans* C=C double bonds into the alkyl chain has also been shown to have a significant impact upon the molecular order of the monolayers formed, as indicated in π–A isotherm studies.[75] Further extensions in this area of research have seen a wide range of functionalised alkyl chains containing alternative terminal functionalities including alcohols, esters, amides, amines, nitriles, phosphonic acids, and phospholipids also successfully applied in Langmuir film preparation.[73,76,77]

Influences upon the structure of Langmuir and LB films are not just limited to structure of the amphiphilic molecules employed, with the incorporation of metal cations into the aqueous subphase also able to have a significant impact upon monolayer formation.[78] The following sections provide a brief overview of two well-established LB systems (long chain carboxylic acids, and phosphonic acids), which a have been extensively studied, with a range of different di- tri- and tetravalent metal cations incorporated into the LB film structure.

1.3.2.1 Metal carboxylates

The incorporation of metal cations into the Langmuir and LB films of long chain carboxylic acids has long been well-established.[78] The presence of the cations dissolved in the subphase typically leads to an acid-base reaction taking place, resulting in the formation of salts (also known as soaps) between the cations dissolved in the aqueous subphase, and the carboxylate headgroups in the monolayer.[79] Not surprisingly, the effects of the metal cations upon the monolayer structure are dependent upon the subphase pH. At low pH values the acidic headgroups tend not to dissociate for example, inhibiting salt formation and consequently having little influence upon the π–A isotherm shape. Therefore a sufficiently high pH is required under which the acid molecules are deprotonated, to facilitate salt formation. The pH range over which acid-salt conversion takes place is not only dependent upon the pK_a of the fatty acid, but is also specific to the metal ions used. This behaviour is thought to be due to differences in the competitive reactions between the metal ion and proton with the carboxylate group.[79]

Association of the metal ions to the subphase-supported monolayer can be exploited to enhance the rheological properties of the monolayer, and improve LB depositions (*i.e.* reduce defects).[80] By using a sequential LB deposition strategy, multilayered films containing layers of metal ions sandwiched between the carboxylate headgroups, can also be built up, Figure 1. The production of LB films using this strategy has been widely reported with an extensive range of divalent metal cations including Ba^{2+}, Cd^{2+}, Ca^{2+}, Co^{2+}, Cu^{2+}, and Pb^{2+} and have been comprehensively reviewed by Peng *et al.*[78]

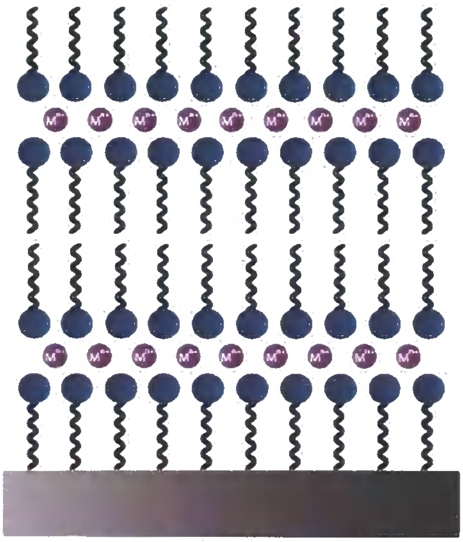

Figure 1. Y-type structure of typical multilayer LB film, consisting of layers of metal ions (M^{n+}, where n = 2 - 4) bound between headgroups of the layers of amphiphilic molecules.

The incorporation of trivalent metal ions into LB films of fatty acids provides a much greater challenge due to the rigid nature of the resulting metal carboxylate monolayers making subphase-to-substrate film transfer difficult. The preparation of yttrium carboxylate films from subphases containing extremely low concentrations of Y^{3+} (10^{-5} M) has been described by various groups. Johnson *et al.* [81] reported Rutherford backscattering experiments upon such films showed an yttrium to carboxylate ratio of 1 : 2, which was suggested to be the result of $Y(OH)^{2+}$ species present in the film structure. However, similar films as prepared by Ganguly *et al.* [82] proved consistent with the incorporation of Y^{3+} species, with XPS data showing an yttrium/carboxylate ratio of *ca.* 1 : 3. Subsequent quartz crystal microbalance (QCM) measurements carried out by Zotova *et al.*[83] upon yttrium stearate films, showed a pH dependency upon the type of yttrium species incorporated into the film structure, with basic yttrium salts ($Y(OH)^{2+}$) favoured at higher pH values. The preparation of europium and terbium arachidate LB films using a similar approach has been described by Silva *et al.*[84] where XPS data showed the metal ion species incorporated into the film to be M^{3+} ions.

1.3.2.2 Metal phosphonates

In an analogous approach to metal carboxylate films, the preparation of multilayered films of metal phosphonates have been extensively studied using alkylphosphonic acids with a range of different metal cations. These films are of particular interest as they act as LB analogues of solid state metal phosphonates, forming two-dimensional, ionic-covalent metal phosphonate layered structures. [85]

Talham and coworkers have reported extensive studies into the preparation and characterisation of LB films of octadecylphosphonates with Mg^{2+}, Mn^{2+}, Cd^{2+}, and Ca^{2+} divalent metal ions.[86] The studies showed the films formed to be consistent with the analogous layered solid structures, $M(O_3PR)\cdot H_2O$ (where M = Mg, Mn, Cd) and $M(HO_3PR)_2$ (where M = Ca) previously identified by Cao and coworkers.[87, 88] Each phosphonate in these structures, bridge four metal ions which in turn are coordinated by five oxygen atoms from four different phosphonates groups. Coordination of a water molecule completes the distorted octahedral geometry of the metal centre. Control over the subphase pH was required for optimum LB film transfer, with the metal phosphonates having a tendency to be soluble at low a pH. The pH range over which optimum film deposition takes place was observed to be specific to the metal ion used.

The occurrence of other solid-state metal phosphonates structures containing trivalent and tetravalent metal species have also provided motivation for the investigation of similar LB analogues. The formation of LB films of lanthanide phosphonates have previously been reported for example, with XPS and FTIR characterisation confirming the film structures to be the same as that found in their solid-state analogues, $LnH(O_3PR)_2$ (where Ln = La^{3+}, Ce^{3+}, Sm^{3+}, Gd^{3+}).[89] Such trivalent metal phosphonates also showed an increased stability towards acidic subphase pH values with stable LB deposition achieved at a lower pH range (2.7 - 3.3) than observed for divalent metal ions (pH 5.2 - 8.1). The onset of trivalent metal association with the monolayer headgroups at lower pH values indicates the affinity of the metal ions towards phosphonate groups parallels the relative acidities of the ions in aqueous media. This behaviour is particularly prominent in the preparation of metal phosphonates of tetravalent ions, where the formation of monolayers upon subphases containing Zr^{4+} cations result in highly rigid films, due to the strong oxophilicity of the metal species, preventing LB deposition even in highly acidic conditions (pH 1).[89,90] An alternative deposition strategy introduced by Talham *et al.*[90,91] circumvents these limitations, providing a route to the production of multilayer zirconium alkylphosphonates films. In this method, assembly of the Zr^{4+} ions upon the phosphonate monolayer surface is carried out following LB transfer of an octadecylphosphonic acid monolayer from a pure water subphase to a hydrophobic support. XPS and FTIR characterisation shows the tetravalent systems form with a stoichiometry $Zr(O_3PC_{17}H_{35})_2$, with the metal-phosphonate binding[92] thought to be similar to that observed in α-$Zr(HPO_4)\cdot H_2O$ solid-state structures.

This approach has also been extended to other systems, more recently being described in the formation of thin films of Prussian blue analogues. Here, the initial LB substrate modification deposited a monolayer consisting of two-dimensional Fe–CN–Ni grid network, upon which sequential solution assembly of Fe^{2+} ions and $[Fe(CN)_6]^{3-}$ complexes can be carried out.[93]

1.4 Preparation of "hard" thin films

1.4.1 Chemical vapour and atomic layer deposition

The surface modification techniques described so far have focused upon the preparation of "soft" organic molecular films using self-assembly and LB techniques. Surface coatings of solid state materials such as metal oxide films have also attracted considerable interest due to their potential application in electronics industry (*e.g.* high dielectric films, see Section 3.1),[94,95] and as optical[96] and protective coatings.[97]

A range of different techniques are available for the growth of metal oxide films, with chemical vapour deposition (CVD) and atomic layer deposition (ALD) in particular being extensively reported. These methods allow for the production of highly uniform and conformal films, with high levels of control offered over the obtained film thickness (typically range from several to several hundred nanometres). The formation of high purity films using CVD processes is carried out through simultaneous delivery of (one or more) gaseous precursor compounds to a heated substrate surface (under reduced pressures), where they react or decompose, and become incorporated into the growing film.[98] ALD differs to CVD in that the reactant precursor compounds are alternately delivered to the substrate surface, upon which they then undergo self-limiting reactions with each other.[99] The requirement for delivery of the precursor compounds in a gaseous state when using these techniques, leads to the need for such compounds to be volatile, whilst also being stable enough to be delivered to the substrate surface. Compounds suitable for such processing in CVD and ALD techniques include halides, hydrides, and metal-organic compounds such as metal alkoxides, alkylamides, diketonates, and carbonyls[100,101] which have been used in the successful production of a range of metal oxide films including SnO_2,[102] TiO_2,[103] Y_2O_3,[104] ZrO_2,[105] and HfO_2.[106]

Although CVD and ALD are perhaps two of the most commonly employed techniques for the fabrication of thin metal oxides films, several other methods are also available, including filtered cathodic vacuum arc (FCVA),[107] electron beam deposition,[108] sputtering[109] and sol-gel synthesis.[110]

1.4.2 Langmuir-Blodgett templated thin metal oxide films

A more novel method towards the fabrication of thin metal oxide films has been previously reported using LB films of metal carboxylate salts. Here, the decomposition of the organic components of LB films, coupled with calcining of the ionic metal layers in the film structure, has been shown to provide a route to the formation of metal oxide films, with high levels of control offered over the film thickness, through regulation of the number of LB layers initially deposited.[111] One of the first examples of this approach was reported by Kalachev *et al.*[112] who described the conversion of LB films of cadmium arachidate to cadmium oxide (CdO) using a low temperature, oxygen plasma at reduced pressure. Plasma treatment of the surface was shown to lead to a reduction in the organic material present in the film as a result of physical ablation and chemical etching processes. Following on from this work, Mirley *et al.* reported similar preparations of thin metal oxide films of SiO_2[113] and CdO[114] using UV-light and ozone. The UV radiation was employed to generate ozone which subsequently oxidises the organic film components, producing volatile species such as carbon dioxide and water. Gang and coworkers[115] demonstrated the preparation of Y_2O_3-stabilised ZrO_2 films by UV/ozone decomposition of LB films of arachidic acid with zirconium and yttrium β-diketonate complexes incorporated into the structure. An additional thermal treatment step was employed to calcine the residual LB film to the final oxide structure.

Thermal treatment of LB films has also been successfully applied in formation of uniform films of several oxides including Y_2O_3, Eu_2O_3, La_2O_3, and TiO_2, using a single high temperature step for simultaneously removal of organic material and calcining of the metal species.[81, 116, 117] The application of such thermal processing has proved limited however with oxide formation from carboxylate LB films of divalent metals such as Pb^{2+}, Ba^{2+}, Zn^{2+}, and Cd^{2+} found to lead to the films coalescing into islands or droplets, preventing the formation of uniform and continuous oxide film structures.[118,119]

1.5 Conventional lithography

Much of the development of early, contemporary lithographic techniques was motivated by the desire to downsize microelectronics. Smaller device components enable the fabrication of microprocessors, offering higher transistor densities, faster performance, reduced power consumption, and reduced production costs. The introduction of photolithography,[120] using UV-light and photosensitive film resists as a route to spatially resolved modification of substrates, has proved of great significance to the semiconductor industry, establishing itself as a mainstay in microfabrication technology. Current state-of-the-art photolithography tools used in industrial scale fabrication of complementary metal oxide semiconductor-field effect transistors (CMOS-FET), offer feature sizes down to 65 nm.[121]

Electron-beam (e-beam) lithography is another long established technique which operates using similar principles as photolithography, employing an e-beam source and electron-sensitive photoresists, cast upon a substrate surface. The shorter wavelengths associated with the electrons (*c.f.* UV-light) enables the generation of patterns with resolutions beyond the limits of conventional optical lithography techniques. Modern e-beam systems, which can generate electrons beams of suitably small spot sizes, when used in conjunction with an appropriate electron-sensitive resist (*e.g.* polymethyl methacrylate, PMMA) can provide patterning resolutions of < 20 nm.[122] Today, e-beam lithography is most commonly used in the production of high resolution masks for use in photolithography and soft lithography processes.

One of the primary drawbacks of both current and future photolithography and e-beam lithography techniques are the associated financial and technical constraints. In response to this, considerable research has been carried out into the development of alternative lithographic methods. One of the most well-established of these is soft lithography,[120,123] as pioneered by George Whitesides during the 1980s, and which has since been widely employed using a variety of different materials (*e.g.* alkylsilanes,[124] alkylthiols,[125] sol-gels,[126,127] polymers,[128] and colloidal materials[129]) for creating the patterned structures. The term "soft lithography" encompasses a range of different methodologies including microcontact printing,[130,131] replica molding (REM),[132] microtransfer molding (μTM),[133] and solvent-assisted micromolding (SAMIM).[134] The principles of these techniques each focus upon the use of an elastomeric stamp (or "mold") to transfer patterned structures of organic molecules or materials to a surface. The production of the master templates using high-resolution lithographic tools (*e.g.* e-beam, UV lithography) enable the fabrication of elastomeric stamps which offer feature sizes down to *ca.* 30 nm.[135]

A less conventional lithographic technique which has undergone rapid development over the past decade has been nanoimprint lithography (NIL).[136] The theory behind this technique is built upon the ability to construct surface structures by direct mechanical deformation of polymeric films cast upon a substrate surface, Scheme 2. An early example of this principle was demonstrated by Chou *et al.*[137] using a mold containing nanoscale surface-relief features, pressed into a thin thermoplastic polymer film ("resist"), spin-cast upon a Si/SiO_2 substrate surface. This technique not only offers the potential for high resolutions in nanofabrication, but is also a relatively simple and low cost process, with high-throughputs achievable using parallel printing set-ups. Typically e-beam lithography is used in the mold fabrication, offering high resolutions down to *ca.* 20 nm.[138]

Scheme 2. Schematic of principle processes used in NIL.

1.6 Scanning probe lithography

Further developments in lithographic technology (largely witnessed since the 1990s) have seen the introduction of non-conventional patterning techniques which move away from the principles of the well-established lithographic strategies such as photo- and soft lithography. Of particular significance has been the development of "scanning probe lithography" (SPL)[139] techniques, which are considered to be a viable route forward in nanofabrication, avoiding the diffraction limitations associated with photolithography, and enabling surface structures with sub-30 nm resolutions to be crafted.

SPL provides a versatile tool for manipulating matter from the nanometre, down to atomic precision. One of the novel benefits of this technique is that the scanning probe microscopy (SPM) tools used in SPL not only provide a means of chemically patterning substrate surfaces, but can also be used in their more conventional fashion to map the topography of the structures created. The three principle techniques of SPM today are scanning tunnelling microscopy (STM), atomic force microscopy (AFM), and scanning near-field optical microscopy (SNOM).

1.6.1 Scanning tunnelling microscopy

STM was the first of the SPM techniques to be developed in the early 1980s[140] which initially enabled surfaces to be imaged under an ultrahigh vacuum (UHV). Today, commercial STMs can operate under ambient conditions if desired, avoiding the need for expensive UHV equipment.

Atomically resolved three-dimensional maps of sample surfaces can be obtained from STM, using an atomically sharp platinum/iridium, or tungsten tip which probes the electron density of the sample surface as it is raster scans across it, Figure 2. A potential difference applied to the tip results in electron 'tunnelling' across the gap (of nanometre range) between the tip and sample. Changes in the tunnelling current generated as the tip raster scans across the sample is monitored by the STM and used to build up an image of surface. The use of STMs as an imaging tool has proved of particular value in the characterisation of SAMs, providing detail of the packing and order within the surface assembly.[141,142]

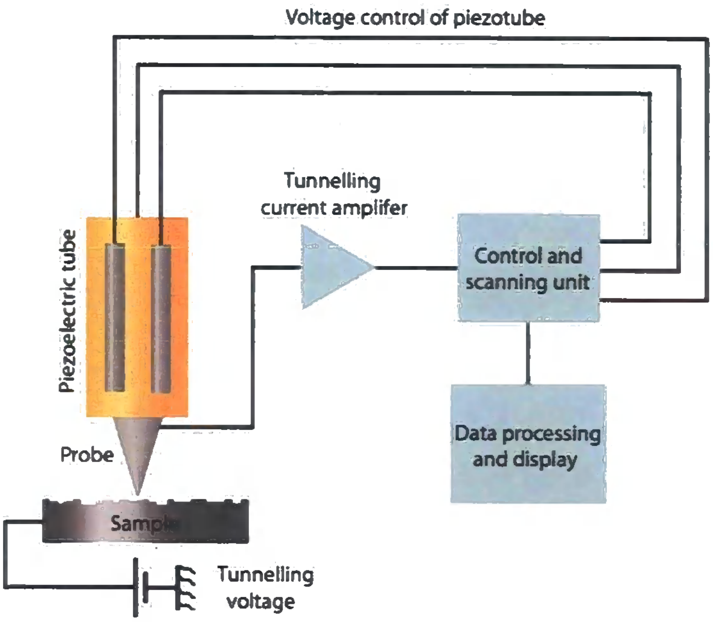

Figure 2. Schematic of the principle operation of a STM.

The development of STM as a lithographic tool has extended its application beyond SAM characterisation, using the STM tip to control and direct surface modification of substrate-supported SAMs and thin polymeric films.[139] Surface structures generated using this technique, have been reported with resolutions down to 15 nm.[143]

The mechanism of the STM-induced surface modification takes place by an elimination mechanism in which surface-bound material is selectively displaced to generate "shaved" features within the film structure. One of the first examples of STM lithography was reported by Kim and Bard[144] who described the modification of *n*-octadecanethiolate SAMs upon Au (111) under ambient conditions. Here, application of a sufficiently low bias voltage and tunnelling current was proposed to bring the STM tip into close contact with the SAM surface, resulting in mechanical removal of the SAM molecules by the tip. The occurrence of this displacement process was evident in STM images, showing holes within the SAM accompanied by an accumulation of material around the periphery of these features.

STM has also been exploited as a low energy electron source in SPL applications, used to selectively degrade regions of substrate-supported thin films. Surface modification of this nature has been demonstrated upon a range of organic monolayers such as alkylthiolate SAMs upon Au and GaAs,[143] and alkylsilane SAMs[145] supported upon Si/SiO_2 substrates.

Surface modification using such low energy electron beams, was described by Crooks *et al.*[146] to take place *via* a Faradaic electrochemical process in which a native thin water layer present upon the film surface acts as an electrochemical cell, and impurities in the water film are proposed to function as an electrolyte, Figure 3. This theory was supported by STM patterning studies which showed changes in the relative humidity of the surrounding environment to have a significant impact upon the surface modification process. This humidity dependency was manifested in failure of the SAM molecules to be displaced from the substrate surface by the applied electron beam at humidities below *ca.* 25 %.

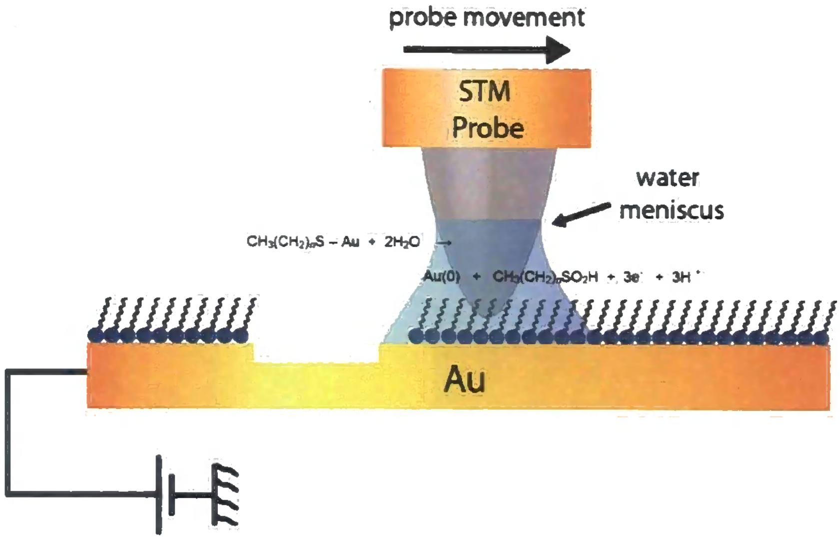

Figure 3. Proposed mechanism of oxidative stripping of alkanethiolate monolayers from a Au substrate using an AFM probe, showing the electrochemical process taking place under acidic conditions. Etching into the substrate is shown to occur, arising from dissolution of the Au.

Although the exact nature of the electrochemical processes which take place during patterning are yet to be fully established, SAM removal observed at a positive applied bias is consistent with oxidative stripping of the SAM molecules, occurring *via* possible reactions such as those shown in Equations 3 (pH < 4) and 4 (pH > 7).

$$\mathrm{CH_3(CH_2)}_n\mathrm{S - Au} + 2\mathrm{H_2O} \rightarrow \mathrm{Au(0)} + \mathrm{CH_3(CH_2)}_n\mathrm{SO_2H} + 3e^- + 3\mathrm{H}^+ \qquad (3)$$

$$\mathrm{CH_3(CH_2)}_n\mathrm{S - Au} + 2\mathrm{H_2O} \rightarrow \mathrm{Au(0)} + \mathrm{CH_3(CH_2)}_n\mathrm{SO_2}^- + 3e^- + 4\mathrm{H}^+ \qquad (4)$$

Further studies by Schoer and Crooks upon Au-supported alkanethiolate SAMs, demonstrated that the fabricated patterned structures are influenced by total amount of current used ('Coulomb dose'), the applied bias, and the number of scans of the tip over the patterned regions.[147] Deeper features, which exceed the length of the SAM molecules, are observed upon increasing the applied bias and number of scans (effectively increasing the total amount of current) for example, suggesting that STM-induced stripping of the SAM molecules is followed by dissolution of the Au substrate.

The development of these STM strategies for the surface modification of SAMs, not only demonstrates the potential of STM technology as a lithographic tool, but also highlights the role SAMs can offer as resists in lithographic processes. SAMs exhibit a number of properties which make them highly desirable for use as resists. Despite being only a single monolayer thick, such films commonly prove highly effective in passivating the underlying substrate, providing protection from a range of "wet" chemical modification processes. This ability of SAMs to act as resists has lead to the extension of STM lithography to incorporate *ex-situ* modification steps, used to further alter the chemical composition of the patterned surfaces. An early example of this strategy was demonstrated by Sugimura and Nakagiri,[145] who described trimethylsilyl (TMS) monolayers as effective resists for protecting Si/SiO_2 substrates from chemical oxidation. In a two-step process, STM patterning was used to selectively degrade regions of the TMS monolayer to reveal the underlying substrate in the patterned regions. Subsequent chemical oxidation of the modified substrate using a H_2O_2 treatment was found to render the patterned regions hydrophilic as indicated by condensation of atmospheric H_2O within the patterns. Further evidence of effective passivation of the substrate was demonstrated by selective "wet" etching of the exposed substrate regions in the patterned SAM using a NH_4F/H_2O_2 solution.

Similar work by Crooks and coworkers carried out upon alkanethiolate SAMs on Au using a subsequent *ex-situ* substrate modification step to selectively deposit copper by chemical vapour deposition (CVD) into the patterned substrate regions.[148]

In-situ substrate modifications have since been demonstrated, in which STM-induced shaving of an alkanethiolate SAM is coupled with backfilling of the exposed Au substrate in the patterned regions with a second alkanethiol of a different chain length.[149] "Substitution" lithography of this nature is achieved through carrying out the SAM patterning process in a non-polar solvent (*e.g.* dodecane) containing the second alkanethiol.

1.6.2 Conductive probe atomic force microscopy

The development of SPL strategies using electrochemically-induced surface modification processes has not been restricted to STM technology. The introduction of atomic force microscopy (AFM) provided an alternative scanning probe technique to STM, using a small tip on the end of a cantilever which physically tracks the sample in an analogous fashion to the stylus on a vinyl record player, enabling a map of the surface topography to be constructed (the principles and operation of this technique are discussed in further detail in Chapter 2). The development of conductive probe AFM (cAFM) not only allowed topographical information to be gathered, but also for currents between a sample surface and a conductive AFM probe (typically using a silicon tip) to be monitored. Localised oxidation of Si/SiO_2 substrates with sub-100 nm resolutions was first demonstrated using a cAFM, under ambient conditions, by Allee *et al.*[150] Local anodic oxidation of the substrate takes place in a similar fashion to conventional anodic oxidation processes, using the AFM probe as the cathode, whilst the naturally occurring water meniscus (formed by capillary condensation) bridging the tip and substrate (anode) acts as the electrolyte, effectively giving a nanoscale electrochemical cell. Application of a negative bias to the AFM probe induces a high electric field leading to ionization of the meniscus water molecules with the resultant OH^- ions acting as the oxidant for electrochemical reactions which take place at the substrate surface (Equation 5). The electrochemical reaction is completed with hydrogen generated at the cathode (Equation 6).

$$M + nH_2O \rightarrow MO_n + 2nH^+ + 2ne^- \quad (5)$$

$$2H^+ + 2e^- \rightarrow H_2 \quad (6)$$

Anodic oxidation using conductive AFM is well documented using SAM-modified substrates. In a similar fashion to previous STM patterning studies, Sugimura *et al.*[151] demonstrated oxidative stripping of Si/SiO_2-supported TMS SAMs *via* electrochemical processes induced by the application of an appropriate voltage bias, with line features down to 30 nm achieved. Further studies by these authors demonstrated transfer of the SAM patterns into the underlying substrate by a wet etch treatment ($NH_4F/H_2O_2/H_2O$) in an analogous process to that described using STM patterned TMS SAMs.[145] Conductive probe AFM patterning upon a range of different monolayer and multilayer films have since been reported including alkanethiolate SAMs on Au,[152] alkyl monolayers upon hydride-terminated silicon,[153] LB monolayers upon Si/SiO_2,[154] and dendritic monolayer films.[155, 156]

Many of these studies have introduced *ex-situ* modification steps, extending the range of chemically heterogeneous patterns that can be produced. Sugimura *et al.*[157] treated patterned TMS SAMs with a second organosilane compound, 3-

aminopropyltriethoxysilane (APTES), for example. The APTES molecules bind to the exposed SiO_2 (see Section 1.3.1.3) in the patterned regions, generating amino-functionalised surface domains. Selective growth of amino-functionalised films within the patterned substrate regions was confirmed by reaction with aldehyde-modified, fluorescently tagged, latex nanoparticles. Using a similar approach Zheng *et al.*[158] demonstrated selective binding of Au nanoparticles (AuNPs) upon amino-functionalised patterns within a Si/SiO_2-supported OTS SAM.

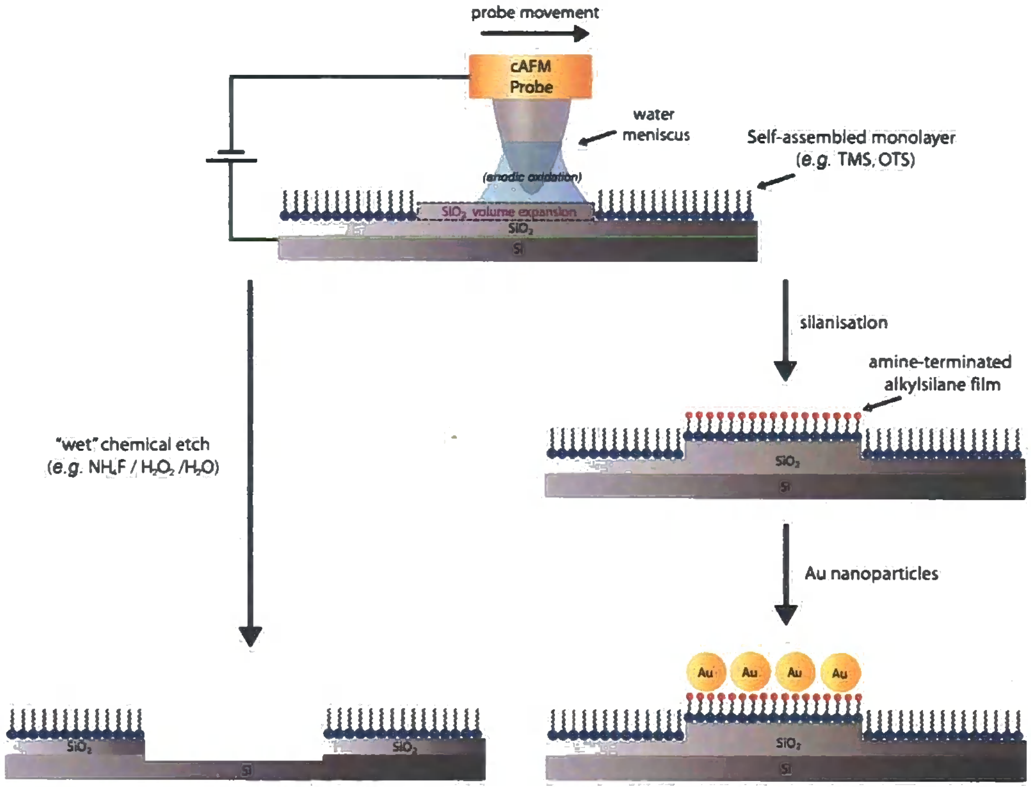

Figure 4. Schematic showing spatially-resolved anodic oxidation of alkylsilane SAMs using cAFM probe. Further modification techniques are highlighted showing the role of organic monolayers as resists, and (amine) functionalisation of patterned regions for template-directed binding of materials (*e.g.* AuNPs).

The examples of cAFM-induced surface modification discussed so far have focussed upon employing an applied bias across the AFM probe and substrate to induce localised degradation of the SAM. However, through careful control over the applied bias, cAFM can also be used to induce electrochemical oxidation of the functional groups at the terminus of the SAM molecules. This approach was first reported by Sagiv *et al.* [159] who demonstrated site-selective oxidation of the terminal CH_3 and vinyl ($-CH=CH_2$) groups of Si/SiO_2-supported OTS and nonadecenyltrichlorosilane (NTS) SAMs respectively, yielding terminal hydroxyl groups. Chemical oxidation of the surface functionalities was observed to occur within a specific applied bias "regime". Below the voltage threshold of this regime, oxidation of the SAM terminal functionality was found to be negligible. Application of a bias voltage in excess of this regime however, resulted in oxidation of the underlying Si/SiO_2 substrate surface. Terminal group oxidation of this nature has since been applied to thiol-terminated organosilane SAMS, with conversion of the thiol group to thiosulfinates or thiolsulonates.[160]

In recent years more novel examples of cAFM surface modification have been reported. The use of an applied bias between a cAFM probe and a substrate to promote localised activation of SAM molecules has yielded encouraging results, for example. The principles of this method rely upon the use of SAMs containing a protecting group that is readily cleaved under electrical stimulation to liberate the protected functionality. This strategy has been elegantly described by Fréchet and coworkers, employing Si/SiO_2-supported SAMs containing a thiocarbonate.[161] Application of a potential bias between the cAFM probe and substrate at localised SAM regions was used to promote bond cleavage of the thiocarbonate, leading to the production of a thiol-terminated SAM surface. This process is carried out under a dry atmosphere to inhibit water meniscus formation between the tip and substrate, which would otherwise facilitate anodic oxidation of the SAM. Template-directed binding AuNPs, through the formation of Au–S bonds was demonstrated upon the patterned surfaces, with the high pattern resolutions (line widths down to 10 nm) enabling a high level of control over the placement of AuNPs. Fréchet has since demonstrated a similar approach upon amine-protected SAMs, with the generated patterns used for covalent immobilisation of fullerenes and aldehyde-functionalised dendrimers *via* hydroamination reactions and imine formation, respectively.[162]

1.6.3 Nanoshaving and nanografting by atomic force microscopy

The earliest forms of AFM operated in contact mode, where the AFM probe drags across a sample, remaining in constant contact with the surface to track the topography. This direct-contact nature, along with the extremely fine radius (typically 10 - 20 nm) of the AFM tip typically leads to significant vertical forces being exerted upon the sample surface. Although during standard AFM operation (in which the surface topography is mapped), it is desirable to restrict the applied vertical forces upon the sample surface (to restrict sample damage and deformation), the generation of such high forces has been utilised in the fabrication of nanoscale surface structures. An early example of this principle demonstrated by Xu and Liu[163] showed reversible, mechanical displacement of a $C_{10}S$- and $C_{18}S$-SAMs upon Au, when an AFM probe is scanned across the surface with above a critical load (*ca.* 280 nN). This "nanoshaving" principle has since been exploited upon a more diverse range of functionalised substrates including SAMs of thiol-modified DNA on Au,[164,165] alkylsilane monolayers on mica,[166] and alkyl monolayers upon hydride-terminated silicon substrates.[167]

Xu and coworkers[168] have also elaborated upon this "nanoshaving" principle, mechanically etching alkanethiolate SAMs under solutions containing a second alkanethiol of a different chain length, Figure 5. The use of a second alkanethiol proved effective for backfilling the Au surface regions exposed by the nanoshaving process, as indicated by the observed height differences in AFM images between the patterned regions and surrounding SAM. This strategy, dubbed "nanografting", was demonstrated to produce nanostructures with line widths down to 10 nm. A variety of different thiol compounds, have since been successfully nanografted within an alkanethiol SAM matrix including carboxylic acid and aldehyde-terminated thiol which have been exploited for template-directed immobilisation of proteins.[169,170]

An alternative approach towards AFM-directed substitution lithography has since been described by Liu[171] using a technique known as "nano pen reader and writer" (NPRW). Here, the AFM probe carries out the dual role of both exerting high applied loads to displace the SAM molecules from the substrate surface, and delivering the "replacement" molecules which bind to the exposed substrate. This was achieved through the use of an AFM probe coated with the replacement molecules prior to mechanical displacement of the SAM molecules. Proof-of-concept of this technique was demonstrated using an alkanethiols offering a range of different terminal functionalities (*e.g.* -CH_3, -CF_3, -CHO, -COOH, -OH) to create surface nanostructures within an alkanethiol SAM matrix.

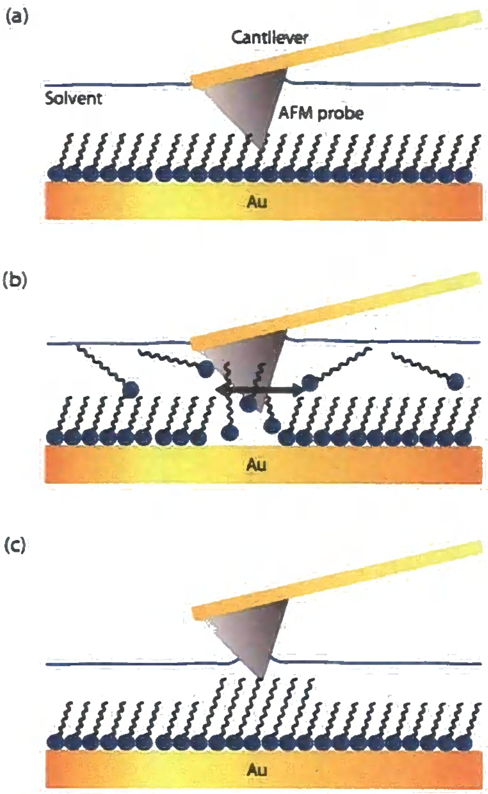

Figure 5. Schematic of AFM nanografting process: (a) Alkanethiolate SAM on Au imaged by AFM to fined suitable area for patterning, (b) SAM undergoes nanoshaving (through application of high vertical forces by the AFM probe) under a solution containing a second alkanethiol of a different chain length (c) The resulting patterned SAM, containing domains of the second alkanethiol, is imaged by AFM.

1.6.4 Dip-pen nanolithography

Since the introduction of SPL to the scientific community, one technique which has generated some of the greatest interest has been the development of dip-pen nanolithography (DPN), as described by Mirkin *et al.*[172] Dip-pen technology is a 4000 year old concept[173] in which ink, coated upon a sharp object, is transported to a paper substrate *via* capillary forces. Utilising this concept in combination with (contact mode) AFM operation, Mirkin developed DPN as a direct-write method towards fabricating nanostructures upon flat substrate surfaces. Mirkin achieved this using the AFM in analogous fashion to a dip-pen with the AFM probe acting as a "nib", delivering "ink" molecules to a solid substrate (acting as the "paper"). Early dip-pen experiments demonstrated the fabrication of well-defined nanostructures of alkanethiol SAMs upon Au, with line widths as narrow (30 nm).[172,174]

Delivery of the "ink" molecules from the AFM tip to the substrate surface was proposed by Mirkin to take place *via* capillary transport through a water meniscus which condenses between the tip and substrate under ambient conditions (*c.f.* electrochemical mechanism of STM and cAFM surface modification), Figure 6. The transported molecules subsequently immobilise upon the substrate surface *via* some form of chemical process (dependent upon the ink-substrate system used). Evidence supporting the formation of a meniscus was shown in experiments carried out by Mirkin in which an AFM probe was brought into close contact with the surface of a NaCl crystal substrate.[175] Subsequent imaging of the substrate surface showed the presence of pits at the points of substrate-probe contact, suggested to occur through dissolution of the NaCl in the condensed water meniscus. The pit sizes were also observed to exhibit a dependency upon the relative humidity of the environment, due to its effects upon the meniscus size.

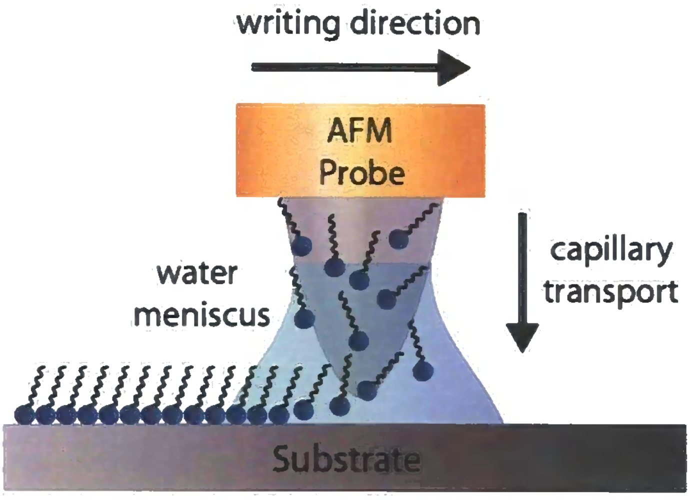

Figure 6. Mechanism of capillary transport of the ink molecules from the AFM probe to the substrate surface, during DPN.

A range of parameters along with humidity are proposed to influence capillary transport of the ink molecules, including temperature, probe-substrate contact time, and water solubility of the molecules.[175,176,177]

Beyond the use thiol-Au systems, and of potential significance to the semiconductor industry, DPN processes using silicon substrates have also been described. Early studies upon Si/SiO_2 substrates were carried out using hexamethyldisilazane (HMDS) which readily reacts, *via* its silazane groups, with the oxide surface producing a TMS monolayer upon the substrate and liberating NH_3.[178] HMDS was chosen as the ink over standard trichlorosilanes and trialkoxysilanes (commonly used in SAM formation upon Si/SiO_2, see Section 1.3.1.3) to avoid polymerisation of the ink molecules in the water meniscus. Controlled DPN patterning of such moisture sensitive compounds has since been demonstrated upon glass[179,180] substrates with careful regulation of the humidity to limit polymerisation. DPN has furthermore been shown to be compatible with a diverse range of inks including fluorescent dyes,[181] conjugated polymers, [182] and colloidal particles.[183] Biomolecules such as proteins,[184,185] peptides[186] and oligonucleotides[187] have also been successfully delivered to substrate surfaces, for the potential development of biosensing devices.

One of the more novel approaches to DPN however, has been the use of sol-based inks for the fabrication of organic/inorganic composite and solid state nanostructures.[188] This method exploits the formation of the water meniscus not only for probe-to-substrate delivery of the metal precursor compound used, but also to onset hydrolysis and sol formation, Equation 7.

$$2MCl_n \quad + \quad nH_2O \quad \rightarrow \quad M_2O_n \quad + \quad 2nHCl \qquad (7)$$

The metal salts employed (*e.g.* $AlCl_3$, $SnCl_2$) as inks typically contain polymeric surfactants, which act to disperse and stabilise the inorganic precursor, and act as structure-directing agents for the resulting patterned sol structures. Formation of metal oxide nanostructures was demonstrated using high temperature treatment of the sol patterns to decompose the organic components (*i.e.* surfactant) of the organic/inorganic hybrid composite. This work was followed by a similar approach to the production of magnetic barium hexaferrite nanostructures using a precursor ink mix of iron nitrate and barium carbonate in ethylene glycol.[189] Hard magnetic nanostructures with dimensions down to 90 nm were produced, offering potential application in the development of high density data storage devices.

1.6.5 Alternative atomic force microscopy lithographic techniques

More recently, an alternative approach to AFM directed lithography has been reported, in which catalytic AFM probes are employed to induce reactions at a functionalised substrate surface. Here, site-directed Suzuki coupling reactions upon arylbromide modified surface were demonstrated using a Pd-coated AFM probe.[190] Spatially resolved coupling was induced at the functionalised substrate by scanning the catalytic probe over the SAM whilst under a solution containing an appropriate coupling agent (*e.g.* phenylboronic acid).

1.6.6 Scanning near-field optical microscopy

The use of STM and AFM as tools towards developing non-conventional lithographic techniques have largely focussed upon using a SPM probe to modify the chemical composition of a sample surface by electrochemical or physical processes. The development of scanning near-field optical microscopy (SNOM) has seen the introduction of a unique SPL technique, employing the principles of photolithography in combination with SPM technology.

At the most fundamental level, SNOM operates following the basic principles of optical microscopy, *i.e.* a light source is used to illuminate the sample, and the reflected light is collected by the microscope. SNOM offers greatly improved resolutions over conventional optical microscopy however, by exploiting the properties of evanescent or non-propagating waves which exist only near the sample surface. The intensities of these waves, which consist of high frequency spatial information about the sample, drop off exponentially with distance from the sample. Their detection therefore requires positioning of the detector at a distance to the sample surface which is much less than the wavelength of light. In a similar fashion to STM and AFM operation, raster scanning of the probe across the sample surface is controlled by piezoceramic elements. A feedback mechanism is typically used to regulate the position of the light source relative to the sample surface.

The collected light is typically detected using a photodiode, with changes in the light intensity as the probe scans across the sample used to construct an image of the surface. The resolution of the offered by SNOM imaging is determined by the size of the point light source (typically 50 - 100 nm).

The use of a SNOM to create nanoscale surface structures, in a process referred to as "scanning near-field photolithography" (SNP) was first demonstrated by Leggett *et al.*[191,192] upon $C_{12}S$ alkanethiol and mercaptoundecanol SAMs on Au. Spatially resolved photopatterning was achieved using the SNOM to deliver UV-light ($\lambda = 254$ nm) to selected regions of the SAM surface, oxidising the alkanethiols to alkylsulfonates (Equation 8) which are much more weakly bound to the substrate. Patterned SAMs were subsequently treated in solutions containing a second thiol, which act to displace the weakly bound sulfonates, or alternatively underwent a wet chemical etch for structuring of the underlying Au in the patterned regions. Contrast between the patterned and non-patterned SAM regions was observed in friction force AFM images of the surface, arising from differences in the frictional characteristics between the patterns and surrounding SAM matrix.

$$\mathrm{Au-S(CH_2)}_n\mathrm{X} \;+\; {}^{3}\!/_{2}\mathrm{O_2} \;\rightarrow\; \mathrm{Au^+} \;+\; \mathrm{X(CH_2)}_n\mathrm{SO_3^-} \qquad (8)$$

By exploiting SNOM technology and its operation within the optical near field, pattern resolutions significantly smaller than the wavelength of the UV-light employed can be achieved, with pattern features of line widths down to 25 nm reported to be achieved. More recently, SNP has been demonstrated in the fabrication of DNA surface nanostructures, through modification of Si/SiO_2-supported SAMs of chloromethylphenylsiloxane (CMPS).[193] Site-selective exposure of the SAM surface to 254 nm UV-light was used to oxidise the terminal chloromethyl functionalities to carboxylic acid groups, with DNA immobilisation upon the patterned regions facilitated using well-established coupling chemistry strategies.

Chapter 2

2. *Characterisation techniques and Langmuir-Blodgett methodology*

2.1 *The Langmuir-Blodgett technique*

The preparation of monolayer and multilayer films using the Langmuir-Blodgett (LB) deposition technique is achieved through the transfer of organised monolayers (known as "Langmuir" monolayers) of amphiphilic molecules from an air-water interface to a solid substrate surface. Amphiphilic molecules, typically comprising of a long hydrocarbon "tail" and a polar "headgroup", tend to be used in LB processes due to their ability to form insoluble, stable monolayer films at an air-water interface, as described by Langmuir.[194] It is a careful balance between the opposing solubilities of the polar headgroup (pulls the molecule into the subphase) and hydrocarbon chain (remain orientated towards the air), which act to maintain a stable monolayer at the interface. Reducing the length of the hydrocarbon chain increases the solubility of the molecule, with an insufficiently long chain length preventing the formation of stable monolayers. Similarly, changes in the polarity of the headgroup will influence monolayer stability, with weakly polar headgroups resulting in aggregation of the molecules into drops upon the water surface. Conversely, a highly polar headgroup can render the molecules too soluble in the subphase for stable monolayer formation.

2.1.1 *Langmuir monolayers*

Langmuir monolayers are commonly prepared through deposition of a known number of amphiphilic molecules from a dilute solution (prepared in a volatile organic solvent, *e.g.* chloroform, hexane) upon an aqueous subphase surface. Upon delivery, the amphiphiles spontaneously spread as a monolayer across the subphase surface, with the organic solvent rapidly evaporating. A movable barrier is used to reduce the subphase surface area, compressing the amphiphilic molecules together into an increasingly condensed monolayer film.

Information about the monolayer properties can be obtained through measurement of the surface pressure as a function of the molecular area (at a constant temperature), to produce a "pressure versus area" (π–A) isotherm. Surface pressure is calculated as the reduction in surface tension of the pure subphase by the surface active molecules, Equation 9. Experimentally this is most commonly determined through monitoring of the subphase surface tension (γ) using the Wilhelmy plate method.[195]

$$\pi = \gamma_0 - \gamma \qquad (9)$$

Figure 7 shows an example of a typical π–A isotherm comprising of several distinct regions from which information about the molecular order of the monolayer structure can be elucidated. Features of the isotherm such as plateau regions and gradient changes generally represent phase changes in the monolayer structure. Harkin assigned these distinctive isotherm regions to represent the different two-dimensional phases or states of the monolayer. A gaseous state (G) was proposed to be first observed within the monolayer, which upon compression undergoes a phase transition to a liquid-expanded (L_1) state. Further compression leads a transition to a liquid-condensed (L_2) state, followed by a highly ordered solid (S), crystalline state finally being observed. At high surface pressures film collapse takes place, typically represented in the isotherm by a decrease in surface pressure, or as a horizontal break (if the monolayer is in a liquid state). The precise shape of the isotherm produced is dependent upon the physical and chemical properties of the amphiphile, and the subphase composition and temperature.

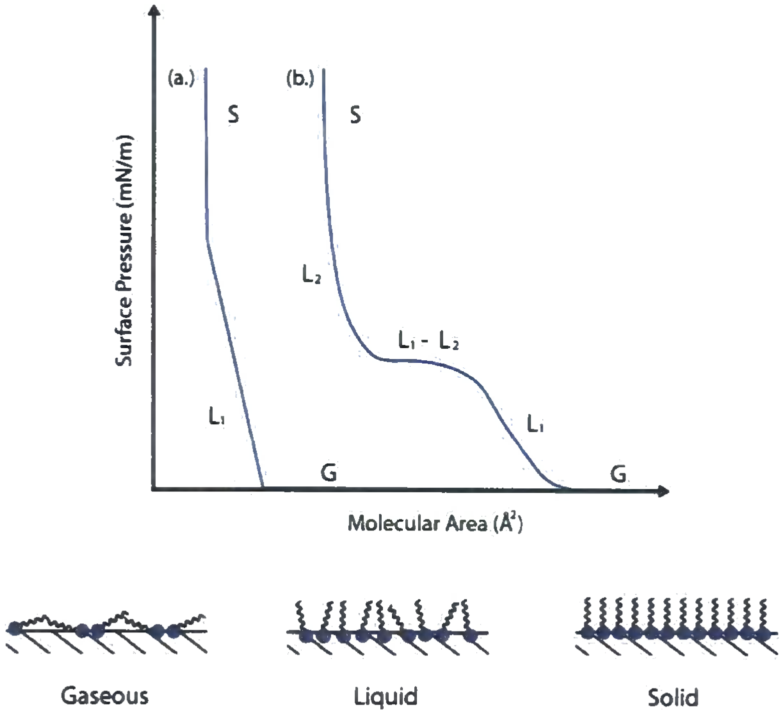

Figure 7. Typical pressure–area (π–A) isotherms of (a) a fatty acid and (b) a phospholipid, showing the two-dimensional gaseous (G), liquid-expanded (L_1), liquid-compressed (L_2), and solid (S) phases observed. Representations of the two-dimensional phases of the monolayers are shown below the isotherm.

Modifications to the chemical composition of the aqueous subphase can also have a significant impact upon the monolayer structure, and the isotherm shape. Extensive studies have been made into the effect of dissolving metal cations in the subphase.[78] Association of the metal cations to the monolayer headgroups can often lead to contraction of the monolayer with the (LC) → (S) phase transition occurring at a lower surface pressure.[196] The extent of this influence has been shown to be dependent upon the metal ions used, with the greater covalent character associated with the interaction of Cd^{2+} and Pb^{2+} ions with the carboxylate headgroups (for fatty acid monolayers), in comparison to divalent alkaline earth cations (where the interaction is predominantly ionic) for example, resulting in greater contraction of the monolayer.[197]

2.1.2 *Langmuir-Blodgett monolayer and multilayer films*

The formation of a LB monolayer relies upon the transfer of a Langmuir monolayer from the air-water interface (maintained at a constant surface pressure, typically with the film in a liquid-expanded/compressed, or solid state) to a solid surface.[73] The structure of the deposited monolayer is dependent upon the film transfer technique employed. The most commonly used method is monolayer transfer to a hydrophilic support, by passing the substrate upwards through a subphase-supported Langmuir monolayer. The resulting LB monolayer deposits with the polar headgroups adhered to the hydrophilic surface, Figure 8a. Monolayers can also be deposited in a "tail-down" fashion upon a hydrophobic surface through vertical passing of the substrate through the monolayer, into the subphase, Figure 8b.

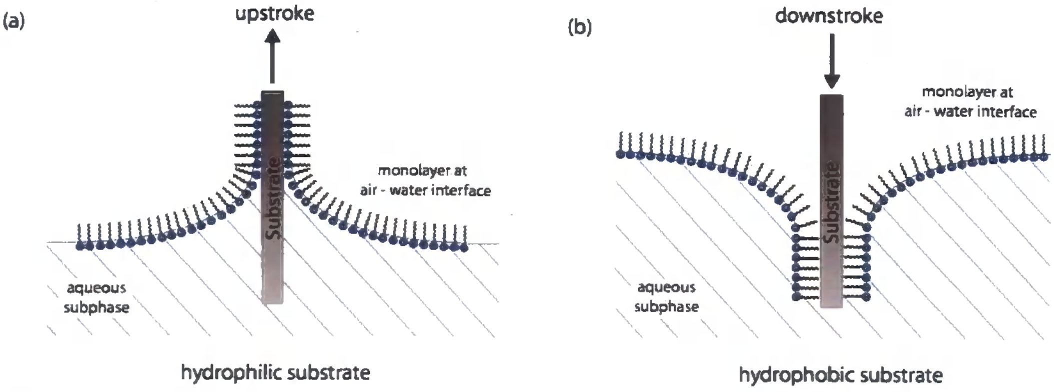

Figure 8. Schematic diagrams showing mechanisms of transfer of LB monolayers from an aqueous subphase surface to an (a) hydrophilic and (b) hydrophobic substrate.

The surface character of the substrate (*i.e.* hydrophilic/hydrophobic) is crucial to successful film transfer. Transfer upon a hydrophilic substrate will only take place upon the upstroke for example, as the hydrocarbon tails tend not to adhere to such surfaces upon the substrate downstroke. A similar principle is also observed during deposition upon hydrophobic substrates, with no monolayer deposition taking place during the substrate upstroke.

Multilayer LB films can also be built up through repeated upstroke and downstroke depositions of the Langmuir monolayer upon the substrate. This typically results in film transfer taking place upon each traversal of the monolayer-air interface, with the monolayers stacking in head-to-head and tail-to-tail orientations, referred to as a Y-type structure, Figure 9. Other multilayer LB structures are also known however, which occur when film transfer takes place during only the upstroke or downstroke of the substrate through the monolayer-air interface. This results in multilayer films which exhibit head-to-tail arrangements of their constituent monolayers, known as X-type (downstroke deposition only) and Z-type (upstroke deposition only) structures respectively.

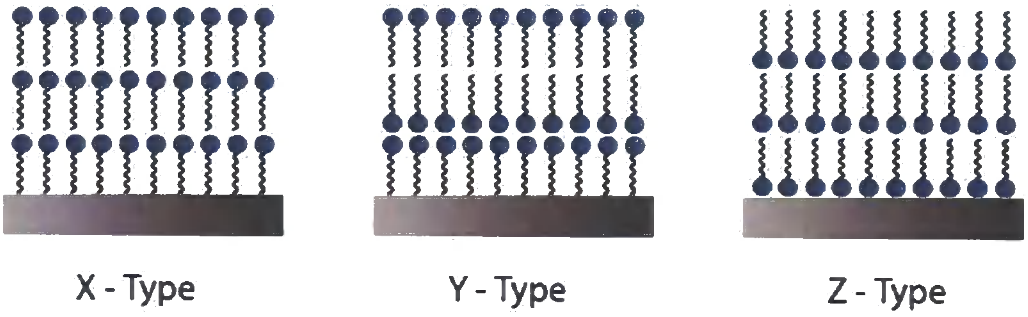

Figure 9. Cartoon representation showing the possible structures produced by multilayered LB depositions.

The efficiency of the LB film transfer is conventionally evaluated using a "transfer ratio". This provides a quantitative measurement of the coverage of the deposited film upon the substrate surface, and is defined as the observed decrease in the Langmuir monolayer area (whilst held at a constant pressure), divided by the surface area of the substrate, Equation 10.

$$\text{Transfer ratio (TR)} = \frac{\text{decrease in Langmuir monolayer surface area}}{\text{total surface area of substrate}} \qquad (10)$$

Although this provides an indication of the deposited film quality, transfer ratios are also subject to limitations. The simple nature of this calculation assumes that the molecular packing and order of the deposited film is the same as that in the initial subphase-supported monolayer, for example. Changes which may take place within the film structure during deposition, fail to be accounted for, meaning a transfer ratio of "1" does not necessarily confirm the presence of a defect-free film.

Poor stability of the Langmuir monolayer upon the subphase also introduces error into calculated transfer ratios. In such a scenario, contributions to the reduction in the monolayer area upon the subphase surface during LB deposition, arising from partial dissolving of the monolayer into the subphase, can lead to transfer ratios > 1. A final consideration during multilayer depositions is the stability of the deposited monolayer. Poorly adhered monolayers deposited upon the upstroke for example may be prone to "peeling" from the substrate surface upon the subsequent downstroke. Transfer ratios fail to account for "peeling" of the monolayers from the substrate during such film preparations.

2.2 Atomic force microscopy

The first atomic force microscope, developed in 1986 by Gerd Binnig, Calvin Quate, and Christoph Gerber,[198] provided a method of mapping surface topographies with atomic resolution. The principles of this microscopy technique are based around the use of a cantilever with a tip or probe (typically 10 - 20 nm in radius) at the end, which is used to track the sample surface as it is raster scanned across it, Figure 10. Control of the probe movement in the x- , y- and z-directions is achieved using x - , y- and z-piezoceramic elements respectively, with an appropriately applied voltage across them. Though it is commonplace to describe movement of the AFM probe across a stationary sample surface, several models of AFM feature a stationary tip under which direct movement of the sample is controlled by piezoceramic elements (such as Multimode AFMs used in the studies here). The probe is maintained at a constant vertical force (determined by the position of the cantilever relative the sample surface, in the z-direction), controlled by the voltage applied to the z-piezoceramic element.

Deflections of the cantilever (in the z-direction), caused as the probe encounters surface features during raster scanning, are monitored by a laser (typically HeNe, 632.8 nm) reflected from the top of the cantilever onto a four-segment, position sensitive photodetector. Changes in the position of the laser along the photodectors y-axes are used to build up a three-dimensional map of the sample. A feedback loop is used to maintain a constant vertical force exerted upon the sample surface by appropriately adjusting the height of the sample relative to the probes z-position (through regulation of the voltage applied to the z-piezoceramic element) to compensate for surface features encountered.

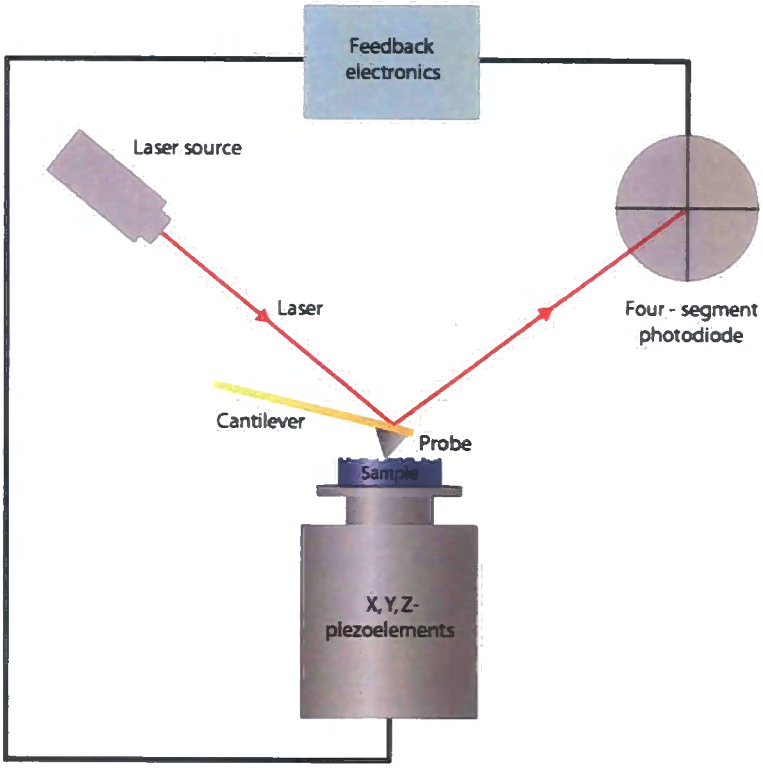

Figure 10. Schematic diagram of principle operation of a (multimode) AFM.

Current AFM technology offers several different techniques by which a sample surface can be probed, with each offering different benefits. The most well established modes of imaging are “contact”, “non-contact”, and “TappingMode^{TM}” AFM.

2.2.1 *Contact mode atomic force microscopy*

The earliest forms of AFM developed operated in contact mode in which the AFM tip remains in constant contact with the surface at a defined setpoint value[198] whilst raster scanned across the sample surface, Figure 11. Contact mode probes are typically fabricated from hard, robust materials such as silicon nitride (Si_3N_4) to limit tip damage (*e.g.* blunting) as a result of the high vertical forces experienced between the probe and sample surface during imaging. These forces are typically of the order of nano Newtons (nN) which although may be considered relatively low values, equate to significantly high pressures exerted upon the sample surface, due to the extremely small radius of the probe tip.

The generation of such high applied forces is one of the primary drawbacks of contact mode AFM operation, potentially causing deformation or damage of the sample surface. This problem is exacerbated in particular when imaging soft samples such as organic monolayers, or biological materials.

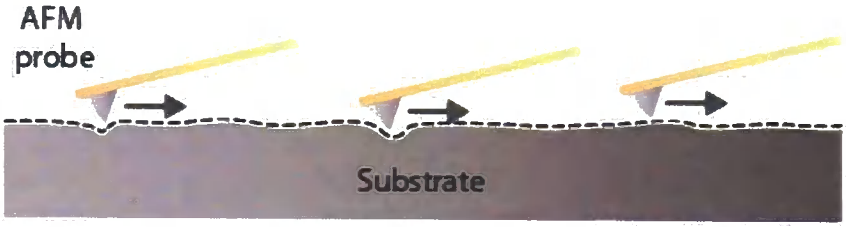

Figure 11. Principle of contact mode AFM operation.

2.2.1.1 Force curves

Information relating to the tip-sample interactions experienced during AFM imaging by can be elucidated using "force curves" in which the deflection of the cantilever as a function of it's displacement in the z-direction, can be monitored. The cantilever deflection is plotted in a force curve as the probe contacts and separates from the sample surface during z-piezo extension and retraction at a single surface point. The resulting plot can be interpreted in terms of the attractive, repulsive, and adhesive tip-sample interactions which take place, as shown in Figure 12.

Quantitative data about the vertical forces generated by the AFM probe upon the sample surface can be extracted from the observed displacement of the cantilever (if the cantilever spring constant (k) is known) using "Hookes Law" (Equation 11) where "k" represents the cantilever spring constant, and "x" is the displacement of the spring (*i.e.* the cantilever).

$$\text{Force} = -\,k \cdot x \tag{11}$$

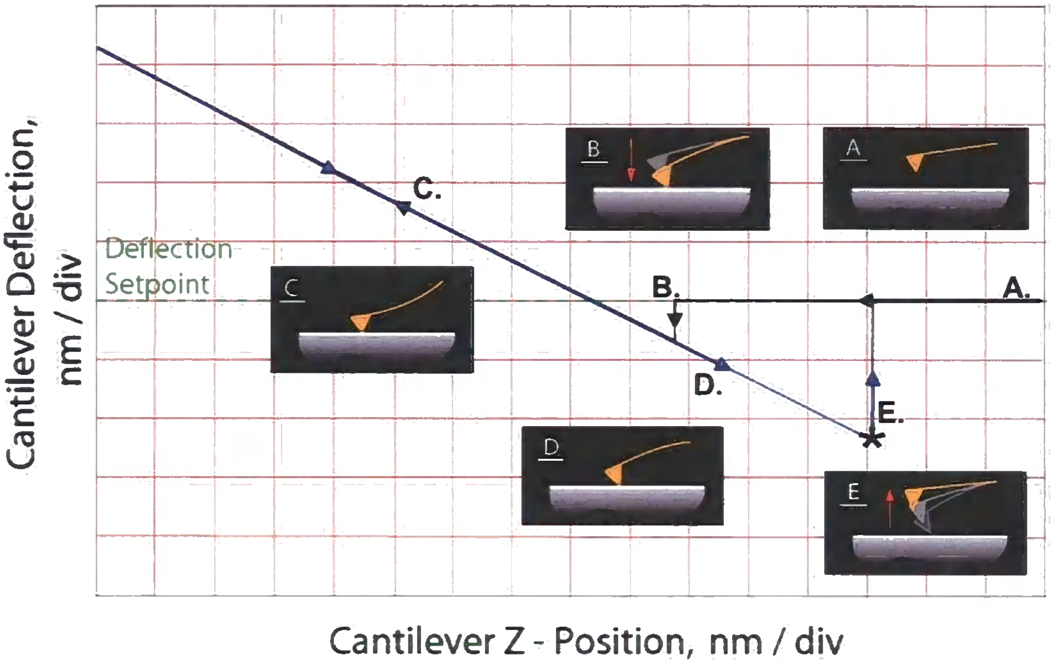

Figure 12. Typical "force-distance" curve generated by a single cycle of the probe extension/retraction. The onset of the curve begins with a large probe-sample separation distance, where no interactions are experienced between the probe and sample (A). As the probe approaches the sample surface, a sudden slight deflection can be distinguished in the curve (B) arising from attractive forces causing the probe to jump into contact with the surface. As the probe continues to extend towards the sample surface, short-range repulsive forces begin to arise, causing a linear increase in the cantilever deflection (C). Upon reaching the maximum force, the probe retracts from the substrate surface, causing a linear decrease in cantilever deflection (D). This retracting curve region crosses the free cantilever deflection (A) due to the attractive probe-surface forces experienced. This minimum provides a measure of the adhesion force causing the probe to "stick" to the sample surface prior to "pull-off". Finally the attractive forces are no longer great enough for tip to remain in contact with the surface leading to sudden "pull-off" of the probe (E), returning the cantilever to its original deflection value. This point, highlighted by the "*" symbol, represents the point at which the vertical forces applied to the sample surface are at a minimum.

2.2.1.2 Friction force microscopy

Contact mode AFM also allows for information other than topographical to be obtained about a sample surface. Friction force microscopy for example, allows compositional differences of heterogeneous surfaces to be identified by mapping differences in surface frictional characteristics. Here the probe is scanned perpendicular to its length with the torsion, or twisting of the cantilever increasing or decreasing depending upon the frictional characteristics of the surface (*i.e.* greater torsion experienced from increased friction). The resulting deflection of the laser along the x-axis of the four-segment photodiode is used to build up an image of the frictional forces experienced by the probe across the sample surface. The use of a four-segment detector enables simultaneous acquisition topographical and frictional data.

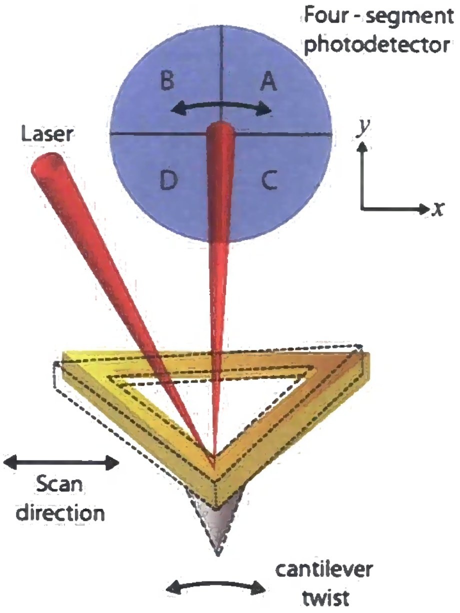

Figure 13. Schematic diagram showing the principles of friction force microscopy, where torsional twisting of the AFM cantilever is monitored through detection of deflections of the reflected laser along the x-axis of the photodiode.

2.2.2 *Non-contact mode and TappingMode^{TM} atomic force micrsocopy*

Non-contact AFM (NC-AFM) provides an alternative means to contact mode AFM for imaging surface topography, using a stiff AFM cantilever which is oscillated (typically at 100 – 400 kHz) at low amplitude near the sample surface, Figure 14. No direct contact between the probe and sample surface takes place. In contrast to contact mode AFM where the probe is brought within a distance of the sample surface and repulsive forces dominate the tip-sample interactions, the spacing between the tip and sample in NC-AFM (typically in the order of tens to hundreds of Ångströms) leads to tip-sample interactions occurring in the attractive force (van der Waals) regime.

These forces are measured through monitoring the resonant frequency or vibrational amplitude of the oscillating cantilever. As the probe encounters surface features, changes in the oscillation amplitude are used to identify and map surface features. In an analogous fashion to maintaining a constant vertical force during contact mode imaging, a feedback system is used to maintain a constant frequency and/or amplitude, also keeping a constant tip-sample distance.

The non-contact nature of this imaging mechanism virtually eliminates lateral forces such as drag, alleviating issues of surface damage and deformation commonly associated with contact mode imaging. This less abrasive imaging mechanism makes NC-AFM techniques a more suitable option for imaging soft organic and biological samples.

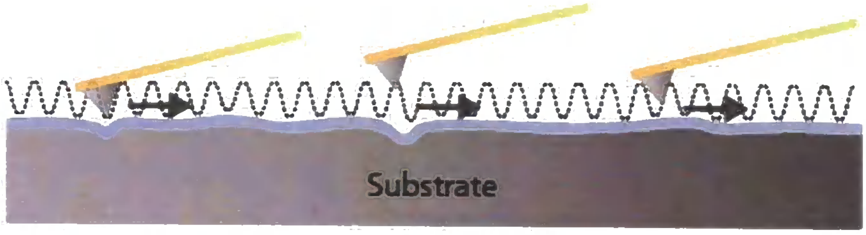

Non-Contact

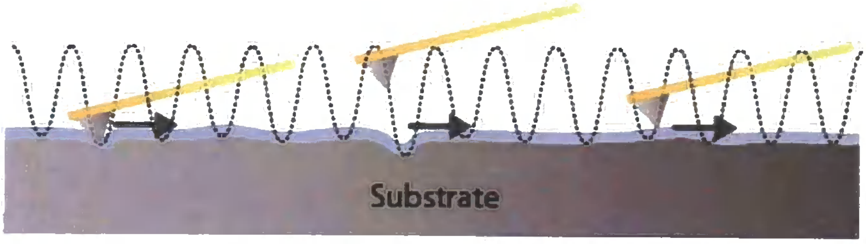

TappingMode™

Figure 14. Principles of non-contact (top) and TappingMode™ (bottom) AFM operation, showing the substrate and the thin liquid layer present upon the surface.

However, potential problems associated with NC-AFM occur when the tip comes into accidental contact with the sample surface. This can result in the tip sticking to the surface due to the meniscus force of the thin liquid film present upon the sample. Upon such events occurring, the z-scanner must retract the tip far enough to detach from the surface, resulting in anomalies in the acquired AFM image.

The introduction of TappingMode™ AFM[199] overcame this problem using larger oscillation amplitudes of the cantilever, Figure 14. The cantilever and probe (typically made of silicon) generally oscillates with a frequency of 50 to 500 kHz. Reduced resolutions are commonly associated with TappingMode™ in comparison to NC-AFM however, with the (intermittent) direct contact of the probe with the sample surface leading to gradual blunting of the fragile silicon tip.

2.3 Ellipsometry

Ellipsometry provides a non-destructive, contactless optical technique for measuring the thickness and optical properties of thin films (ranging from sub-nanometre to micron thickness), by measuring and interpreting changes in the state of polarised light reflected from a sample surface. These observed changes in polarisation state are dictated by the optical properties (refractive index, η, extinction coefficient, κ) and thickness of the sample. Samples suitable for ellipsometry studies must consist of a small number of discrete, well-defined layers which are optically homogeneous, isotropic, and reflect significant amounts of light.

Modern ellipsometers consist of a monochromatic light source (typically a HeNe laser, 632.8 nm) which is first passed through a polariser, Figure 15. The resulting linearly polarised light is incident upon the sample surface at a defined angle of incidence (Φ) (commonly 70 ^{o}). Upon reflection of the light from the sample surface, the linearly polarised light becomes elliptically polarised due to the "*s*" (oscillates perpendicular to the plane of incidence) and "*p*" (oscillating parallel to the plane of incidence) components of the polarised light experiencing a different attenuation and phase shift. The elliptically polarised light passes through a second polariser, known as the analyser, before falling upon a detector. From the reflected light, the ratio of the r_s and r_p reflection coefficients (which describe the amplitudes of the polarised lights *s* and *p* components) is measured.

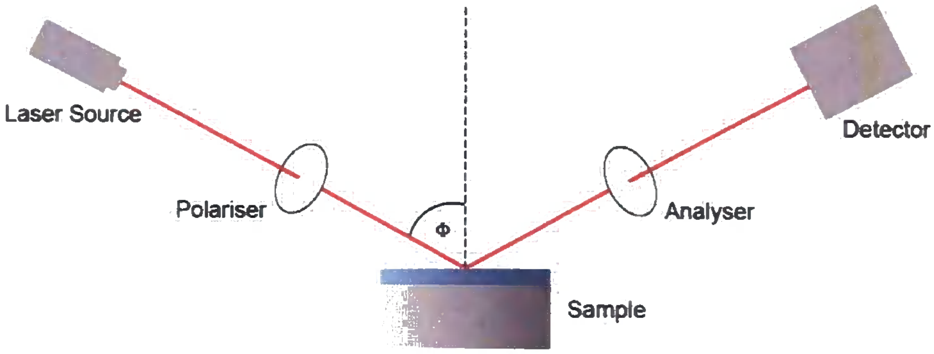

Figure 15. Schematic diagram of the operation of an ellipsometer, where Φ defines the angle of incidence of the laser upon the sample surface.

The film properties (thickness, refractive index, η, extinction coefficient, κ) are subsequently be evaluated using the measured r_s/r_p ratio and calculating the Stoke parameters, ψ and Δ, as a function of wavelength and angle of incidence. These parameters are related to ratio of the reflection coefficients by Equation 12 where tan (ψ) describes the reflection amplitude ratio, and Δ is the phase shift.

$$r_p / r_s = \tan(\psi)\, e^{i\Delta} \qquad (12)$$

The optical constants of the sample under scrutiny are determined by fitting of the calculated parameters to a model which considers the refractive index and thickness of all individual layers of the film structure. Software analysis using an iterative procedure, in which the unknown optical constants and thickness parameters are varied, is used to calculate the Ψ and Δ parameters. The calculated Ψ and Δ values which offer the "best fit" match to the experimental data provide optical constants and thickness parameters for the sample.

As this technique is based upon measuring the ratio of two values (r_p / r_s), rather than recording absolute values, it can provide highly accurate and reproducible results, and requires no standard reference.

2.4 X-ray reflectometry

X-ray reflectometry (XRR) provides a non-destructive method for measuring the physical properties of thin films such as surface roughness, density, and film thickness. The principles of this technique are based upon monitoring changes in the reflectivity of X-rays incident upon the substrate surface (covered by the thin film under analysis) as a function of the angle of incidence.

Changes in the X-ray reflectivity (as the angle of incidence is varied) arise from the X -ray beam as it strikes the surface and penetrates into the film structure, resulting in X-rays reflecting from both the top and bottom surfaces of the film, Figure 16. Interference of the X-rays reflected from the top and bottom film surfaces lead to changes in the intensity of reflected light. Interference between the reflected X-rays (*i.e.* constructive/destructive) is dependent upon the angle at which they are incident upon the film surface.

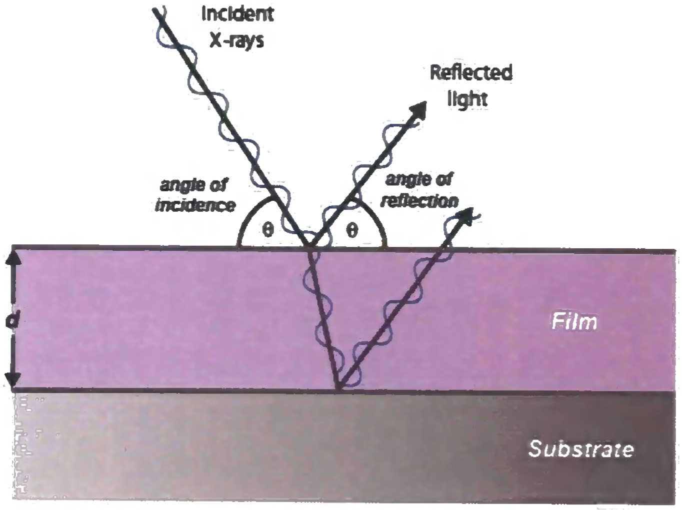

Figure 16. Interference of X-rays reflected at the top and bottom of the film surfaces.

A typical X-ray reflectometer comprises of a monochromatic X-ray source which irradiates the sample at a grazing angle, $\omega = \theta$. The intensity of the reflected beam is collected by a detector (at a 2θ angle, Figure 17.) from which an X-ray intensity pattern is constructed as a function of the angle of incidence.

Quantitative values of the film properties (thickness, roughness, density) can be extracted from the X-ray pattern using data model analysis. Here, estimates of these unknown film parameters are input into a theoretical computational layered film model, used to represent the substrate/film sample structure. Software analysis, using an iterative procedure, varies and refines the thickness, roughness and density values of the theoretical model to find a "best fit" which most accurately represents the experimental data. From this "best fit", values of the film thickness, roughness and density are obtained.

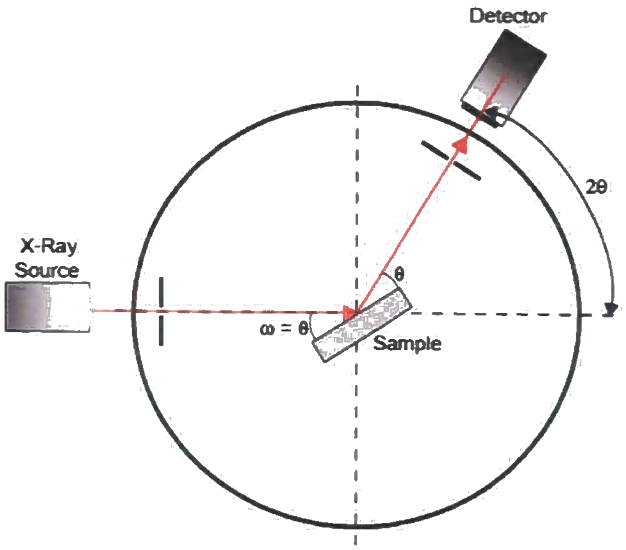

Figure 17. Diagram showing the operation of an X-ray reflectometer.

Further information can often be elucidated directly from the X-ray pattern as well, such as in the analysis of multilayer films (*e.g.* LB films exhibiting multilamellar structures). Such films exhibit reflectivity curves of a typical shape in which Bragg peaks are commonly observed, separated by interference, or 'Kiessig' fringes (which arise from interference of the X-rays reflected from the top and bottom surfaces of the film). The distance in q-space between two Bragg peaks is inversely proportional to the periodicity of a film consisting of a multilamellar structure (*e.g.* multilayer LB films), which can be determined using the relationship shown in Equation 13.

$$d = 2\pi / \Delta q \qquad (13)$$

Similarly, a value for the total thickness of the multilayer film can be derived from the spacing of the Kiessig fringes using this same relationship. The number of repeat layers (*i.e.* bilayers in the multilayer LB film) can also directly related to the number of

Kiessig fringes observed between two adjacent Bragg peaks using the relationship "N - 2" (where N represents the number of bilayers).

2.5 *X-ray photoelectron spectroscopy*

X-ray photoelectron spectroscopy (XPS) is one of the most powerful and valuable surface sensitive analysis techniques (with a typical probing depth of *ca.* 0.5 – 5 nm, *i.e.* the first *ca.* 2 - 25 atomic layers), providing quantitative information about the chemical make-up of sample surfaces.

The theory behind this technique focusses upon bombarding a sample with X-rays of sufficiently high energies (in excess of 1000 eV) to stimulate (photo)emission of electrons from the core energy levels of atoms. The requirement for such high energy photons (hυ) in this process arises from the large binding energies (BE) of the core electrons which must be overcome for successful photoemission. The energy considerations of this process are described by Equation 14 whereby the emitted electron has a defined kinetic energy governed by the input photon energy and the core electrons binding energy.

$$E_{kin} = h\nu - BE \qquad (14)$$

The resulting 'vacancies' produced in the core electronic energy levels are subsequently filled by valence electrons from an outer electronic energy level 'dropping down' to the lower energy core shell (typically accompanied by the emission of an 'Auger electron' or X-ray fluorescence, Figure 18).

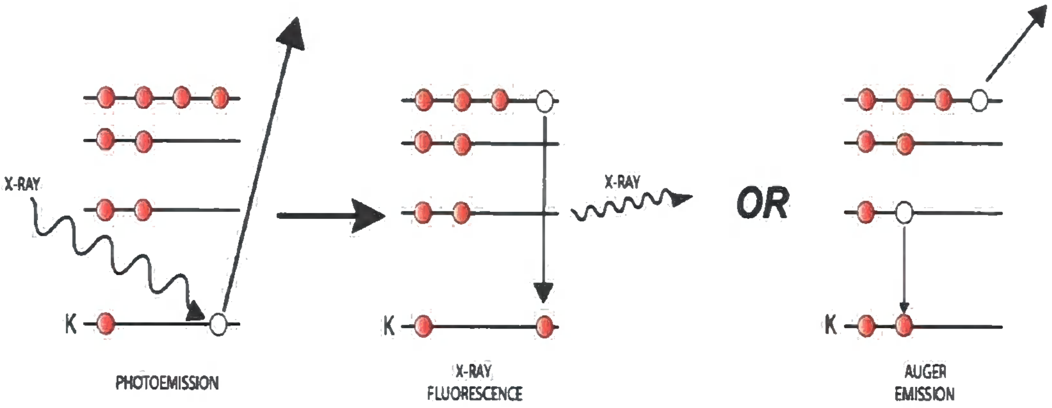

Figure 18. Schematic diagram describing photoemission of a core shell electron from an atoms electronic structure stimulated by irradiation of the sample with high energy X-rays, and the accompanying X-ray fluorescence and Auger emission processes which take place as the core shell 'vacancy' is filled by an electron 'dropping down' from a higher electronic energy level.

XPS uses these principles to extract chemical information about a sample by stimulating photoemission from the sample under analysis, using photons of known energy, and recording the kinetic energy of the ejected core electrons. From this data the binding energies of the emitted electrons can be determined, Equation 15. The binding energies of core electrons are highly characteristic of the element which they originate from, enabling the calculated binding energies to be referenced to the constituent elements of the sample material. Small 'chemical shifts' in binding energies can also yield information about the surrounding chemical environment of an atom, as well as changes in its oxidation state, allowing deductions to be made about the chemical structure of the sample.

$$BE = h\nu - E_{kin} \tag{15}$$

As well as the dependency upon the probability of exciting a specific electronic energy level within an atom, quantitative XPS analysis is also dependent upon the "mean free path" (λ) of the emitted electron. This is defined as (a distribution average of) the distance covered by an electron between two inelastic collisions,[200] or in relation to XPS analysis, the depth from which a photoemitted electron can travel from the sample without undergoing an inelastic collision. Such collisions taking place (through interaction with the surrounding sample matter) result in a loss of energy associated with the electron. Electrons which undergo such interactions contribute to the background noise build-up observed in the XPS spectrum. Electrons which leave the sample without undergoing any such collisions, conserving their energy, result in intense photoelectron peaks in the spectrum. Due to the short mean free path of electrons in solids, only electrons from the first few atomic layers of the sample are detected, leading to the surface specific nature of the technique.

Experimentally, XPS is carried out under ultra high vacuum (UHV) conditions (*ca.* 1 x 10^{-8} mbar) to prevent the inelastic collisions of the ejected photoelectrons with any gaseous particles in the system. The spectrometer itself typically comprises of UHV pumping equipment, an X-ray source, collision and preparatory chambers, an electron energy analyser, and counting and recording equipment, Figure 19.

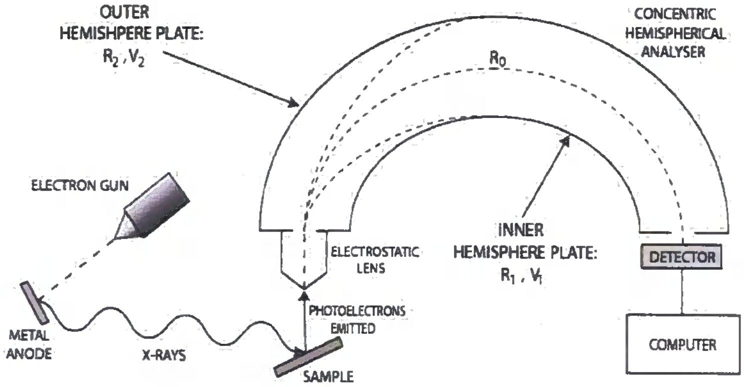

Figure 19. Schematic of typical set-up of an XPS spectrometer.

2.6 *Contact angle analysis*

In surface science, measurement of contact angles, at which a liquid/vapour interface meets a solid surface (the "three phase point"), is commonly used to determine the chemical affinity a liquid has to a solid. Contact angle measurements are commonly carried out using the sessile drop technique in which a single droplet of a liquid (typically high purity water) is placed upon a flat substrate surface. The contact angle (θ) is measured at the tangent of the solid/liquid/vapour interface, Figure 20.

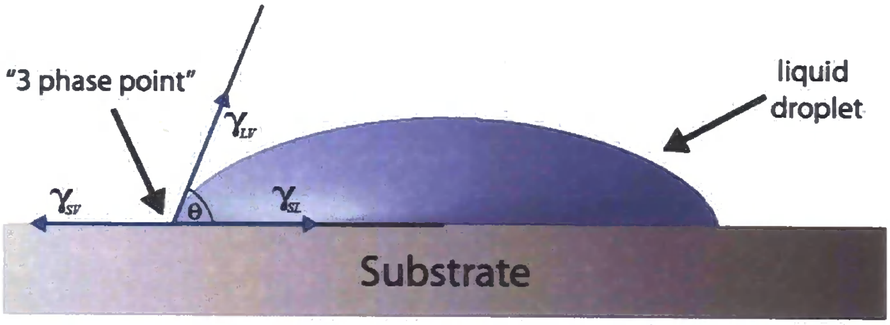

Figure 20. Diagram representing how the contact angle (θ) of a liquid probe upon a substrate surfaces is calculated. γ_{SV}, γ_{SL}, and γ_{LV} represent the surface energies at the surface-vapour, surface-liquid, and liquid-vapour interfaces, respectively.

The magnitude of the observed θ value (which is governed by the interactions across the liquid/vapour/solid interfaces) provides an indication of the affinity between the sample surface and probe liquid. Using high purity water as the probe can elucidate information about the hydrophilic/hydrophobic character of the surface, for example. Low contact angles ($\theta < 90^{o}$) where the water droplet lies largely flat, "wetting" the surface, indicates a high affinity between the probe liquid and the substrate (*i.e.* the surface is hydrophilic). As contact angles approach $\theta = 0\ ^{o}$, complete "wetting" of the surface is observed. In contrast, a hydrophobic surface results in "beading" of the water droplet with larger contact angles exhibited ($\theta > 90^{o}$) indicating the liquid-substrate affinity of the system.

Chapter 3

3. *Preparation ultra-thin transition metal oxide films*

3.1 *Introduction*

The production of thin metal oxide films of zirconium (ZrO_2) and hafnium (HfO_2) has received much attention due to their potential as surface coatings to prevent corrosion and promote thermal stability.[201,202] But perhaps their most promising application is in the electronics industry as a replacement dielectric for silicon oxide (SiO_2) or oxynitrides in complementary metal oxide semiconductor (CMOS) technology.[94,95] The constant scaling down of transistors has necessarily led to a demand for reduced thickness gate dielectrics in order to maintain high capacitance of the gate material (which is dependent upon the gate material thickness (d) being proportional to the gate length, see Figure 21). The reduction of the standard gate dielectric SiO_2 (dielectric constant $\kappa = 3.9$)[203] to a thickness approaching 1.5 nm results in problems such as current leakage, due to quantum mechanical tunneling of electrons across the gate, which may have an adverse effect on device performance.[204]

One solution to this problem is to replace the gate SiO_2 with alternative higher dielectric materials which will allow the use of thicker gate films, while retaining the high capacitance required for successful transistor operation. However, there are significant challenges associated with such a task, including finding a material which is suitably compatible with silicon and able to withstand the conditions of semiconductor processing. Metal oxides such as ZrO_2 and HfO_2 (both with an estimated κ = *ca.* 25)[203] may satisfy such criteria, exhibiting a high dielectric constant as well as stability to silicidation and silicate formation to temperatures up to 900 °C.[205]

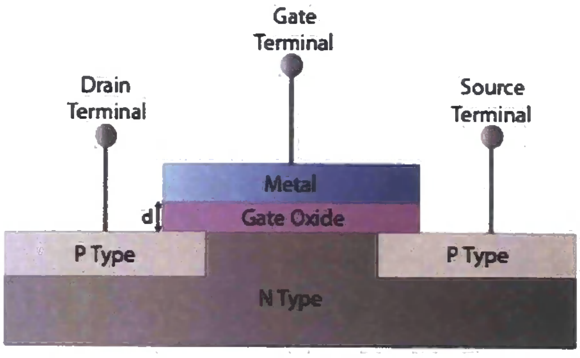

$$C = \frac{\kappa\ \varepsilon_o\ A}{d}$$

Figure 21. A typical complementary metal oxide semiconductor field effect transistor (CMOS-FET), with the equation showing the relationship between the capacitance (C) of the gate oxide to the dimensions of the dimensions of the oxide material, where "κ" represents the dielectric constant, "ε_o" the dielectric permittivity, "A" the gate oxide area, and d the thickness of the gate oxide.

Several different methods for the production of such thin metal oxide films have been reported in recent years, including chemical vapour deposition (CVD),[105] atomic layer chemical vapour deposition (ALCVD),[206] sol-gel synthesis,[109] electron beam deposition,[108] filtered cathodic vacuum arc (FCVA) deposition,[107] and sputtering.[110] Typically these processes have been used in the production of oxide films ranging from several to hundreds of nanometre thick, with a typical route mean square (rms) roughness of <1 nm.

3.2 Octadecylsiloxane / metal-octadecylphosphonate hybrid films

A new approach to the production of homogeneous, nanometre-thick metal oxide films, MO_2 (M = Zr, Hf), is described here by deposition of Langmuir-Blodgett (LB) films of octadecylphosphonic acid (ODP-H_2) upon an octadecyltrichlorosilane (OTS)-modified Si/SiO_2 substrate, and subsequently stabilised through binding of ionic metal species to the deposited monolayer headgroups, as previously described by Talham *et al.*[90] The resulting OTS/metal-octadecylphosphonate (metal-ODP) hybrid film acts as a "template" to the final metal oxide structure, produced using a thermal treatment to decompose the organic film material and calcine the inorganic components in a single step, Scheme 3.

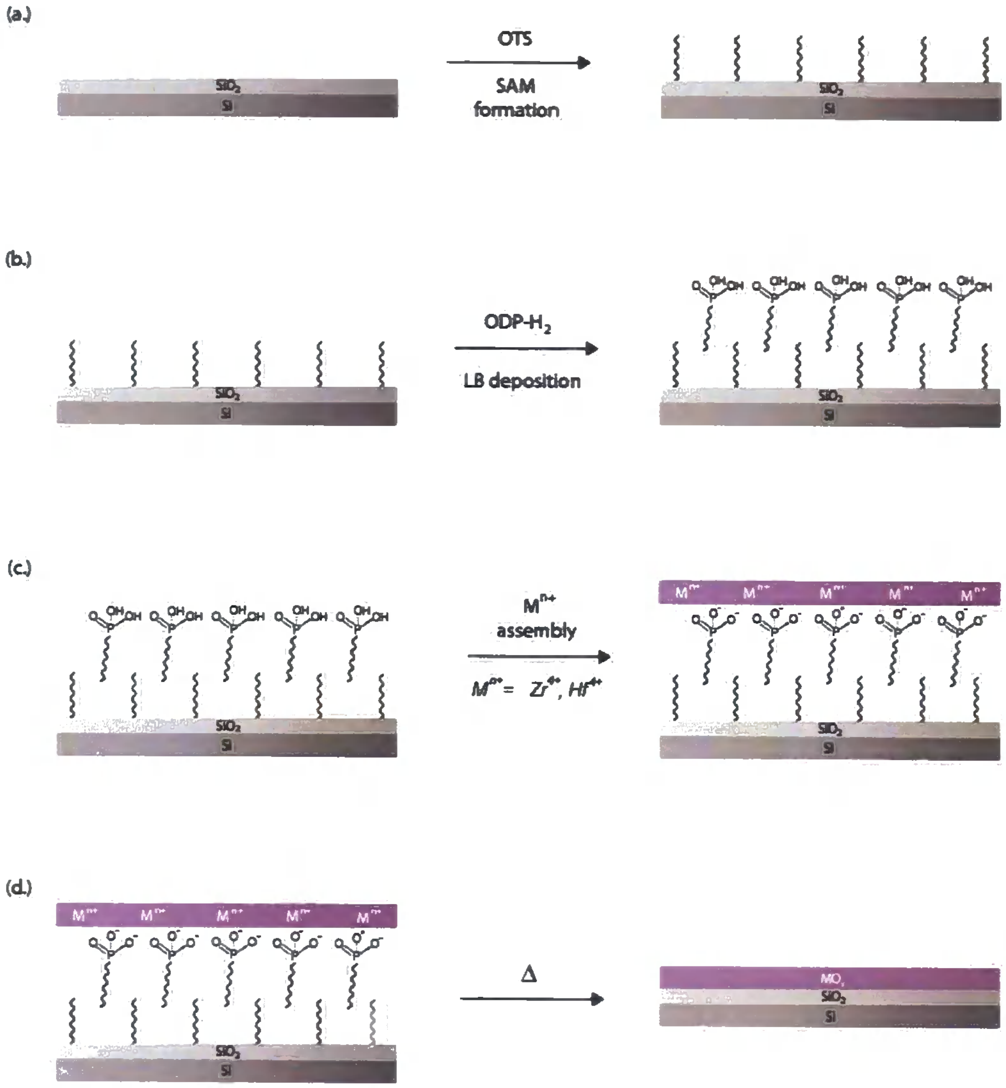

Scheme 3. Four-step method employed to produce OTS/ODP-metal hybrid films, upon a Si/SiO$_2$ support: (a) Formation of SAMs of OTS upon Si/SiO$_2$ substrates prepared using OTS solutions (1mM) in anhydrous toluene. (b) "Tail-down" LB deposition of an ODP-H$_2$ monolayer upon OTS-modified Si/SiO$_2$ substrate. (c) Binding of cationic zirconium species upon the phosphonate-terminated surface through treatment in an aqueous ZrOCl$_2$·8H$_2$O solution (0.5 mM). (d) Thermal treatment of the OTS/ODP-metal hybrid film leads to decomposition of the organic film components and simultaneous calcining of the inorganic metal ion layer.

3.2.1 Octadecyltrichlorosilane self-assembled monolayers

Initial modification of the Si/SiO$_2$ substrate by formation of an OTS self-assembled monolayer (SAM) provides a highly hydrophobic surface, as required for successful "tail-down" LB deposition of an ODP-H$_2$ monolayer upon the substrate surface. SAM formation is carried out under anhydrous conditions to limit hydrolysis and subsequent polymerisation of the OTS molecules in the bulk solvent. Restricting these processes to taking place at the hydrated Si/SiO$_2$ substrate surface aids the formation of homogeneous SAM surfaces.[207,208] The need for OTS films of low roughness arises from the potential impact upon the quality (*e.g.* the number of defects) of the LB films deposited upon the SAM surface.

Following SAM modification, static contact angle values of 106 ± 3° confirmed successful generation of a hydrophobic surface upon the hydrophilic Si/SiO$_2$ substrate (27 ± 4°). Ellipsometry measurements carried out upon the modified substrate calculated an average OTS film thickness of 2.1 ± 0.2 nm, implying the self-assembled film does not exceed one layer. Comparison of this value to the theoretical length of an OTS molecule (*ca.* 2.6 nm[207]) indicates an element of tilt (up to *ca.* 25°) to the surface normal associated with the alkyl chains. This is consistent with the formation of a crosslinked monolayer, which is shown in molecular modelling studies[209] to lead to significant steric hindrance between the alkyl chains. Consequently the alkyl chains are forced to tilt considerably to relieve this steric repulsion. XPS data showed no indication of chlorine present in the OTS film confirming complete hydrolysis of the SiCl$_3$ headgroups. Though this does not conclusively establish the formation of Si–O–Si linkages between the OTS molecules, the facile nature of this nucleophilic reaction suggests the presence of crosslinking to be highly likely.

Evaluation of the OTS surface quality by AFM reveals a homogeneous, low defect surface with a route mean square (rms) roughness of 0.3 ± 0.1 nm over a 5 x 5 μm^2 region, see Figure 22. Particulates (*ca.* 10 nm in height) observed to be sparsely distributed across the film surface (Figure 22, blue arrows) are thought to arise from a small degree of polymerisation of the OTS molecules forming small aggregates which physisorb to the modified substrate. Organic contamination of the surface from the surrounding environment may also contribute the presence of such small surface-bound particulates.

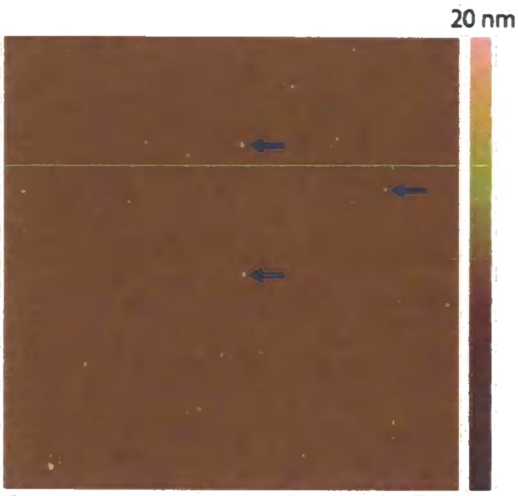

Figure 22. TappingMode™ AFM image of 6 x 6 μm^2 region of an OTS-modified Si/SiO_2 substrate. The blue arrows highlight aggregates of polymerised OTS present upon the SAM surface.

3.2.2 Metal-octadecylphosphonate Langmuir-Blodgett monolayers

Prior to LB film deposition upon the hydrophobic substrates, pressure versus area (π–A) isotherm studies of Langmuir monolayers of ODP-H_2 were carried out upon a high purity H_2O subphase. The resulting isotherms show a single uniform pressure increase, with monolayers stable to surface pressures up to 50 mN/m before film collapse occurred. This single gradient change suggests a sublimation phase change with the film undergoing direct transition from a two-dimensional gaseous to a two-dimensional solid state. No gradient changes are apparent that would indicate gaseous-liquid and liquid-solid phase transitions, Figure 23. Molecular area determination from the isotherm reveals an average area of 24.7 ± 2.5 Å^2 occupied by each ODP-H_2 molecule upon the subphase surface, falling within the expected range of values.[20,90]

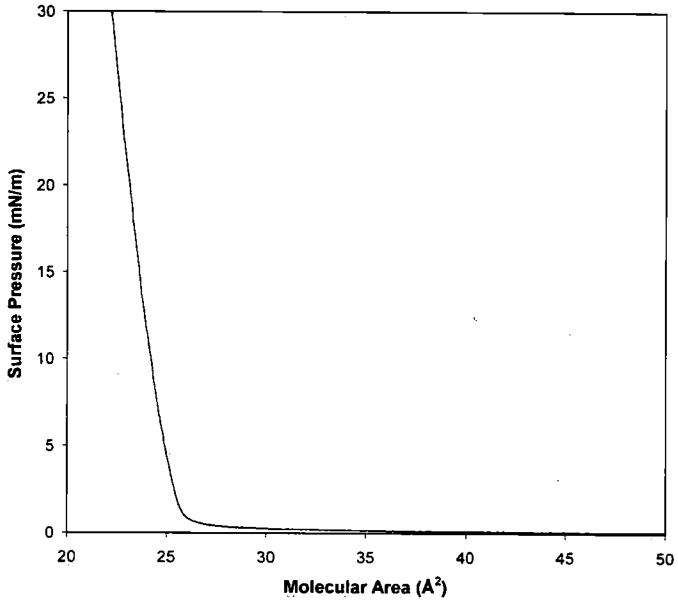

Figure 23. A typical π–A isotherm produced during the formation of a Langmuir monolayer of ODP-H_2 upon a pure H_2O subphase.

The transfer ratio (TR = decrease in Langmuir monolayer surface area / total surface area of substrate, see Section 2.1.2) of the monolayer film, calculated to be 0.93, indicates efficient transfer of an ODP-H_2 monolayer to the hydrophobic substrate surface. This successful film transfer was observed to take place upon the downstroke of the hydrophobic substrate through the subphase-supported monolayer, indicating "tail-down" deposition of the film resulting in a PO_3H_2-terminated LB film surface. The complete coverage of the substrate surface indicates the deposition of a film which is largely free of defects (assuming no peeling of the film from the substrate takes place upon removal from the subphase, after the metal ion layer assembly).

Following LB transfer, exposure of the deposited ODP-H_2 film to aqueous solutions of $ZrOCl_2 \cdot 8H_2O$ and $HfOCl_2 \cdot xH_2O$ (x = 6 - 8) (*ca.* pH 3) respectively, leads to "capping" of the surface through the formation of salts between the cationic metal species and the PO_3H_2 groups at the monolayer surface. Preparation of Zr-ODP LB films previously reported by Talham[90] proposes the phosphonate-terminated surface to be capped by a monolayer of Zr^{4+} ions, with each metal cation bound to three oxygen atoms from three separate phosphonate headgroups. The nature of the zirconium-phosphonate binding is thought to be similar to that found in layered α-zirconium phosphates,[210] and results in a significant degree of crosslinking of the ODP molecules in the Zr-ODP film structure. This crosslinking provides a robust film structure arising from the resulting cooperative nature in which the ODP molecules act, conferring enhanced stability upon the film. Though their preparation has not been previously reported, corresponding Hf-ODP films are rationalised as exhibiting similar structural character and stability due to the highly analogous chemistry of zirconium and hafnium arising from their almost identical atomic (Zr = 1.45Å, Hf = 1.44 Å) and ionic (Zr = 0.86 Å, Hf = 0.85 Å) radii as a result of the "lanthanide contraction".[211]

The stabilisation conferred upon the LB film from the cationic metal layer is evidenced from uncapped ODP-H_2 films which are readily stripped from the substrate surface upon removal from the H_2O subphase. Stripping of the ODP-H_2 monolayer is believed to occur immediately upon removal from the subphase, "peeling" from the substrate back to the aqueous subphase surface due to the preference of the monolayers polar headgroups to remain in intimate contact with a hydrophilic environment. Detachment of the LB film from the substrate upon removal from the subphase is indicated from static contact angle values which remain in excess of 100 °. Such hydrophobic character is expected to arise from the CH_3-terminated surface provided by the underlying OTS SAM rather than the polar PO_3H_2 surface of the deposited ODP-H_2 LB film. Further evidence supporting LB film detachment from the OTS-modified substrate is shown by AFM where the film surfaces appear largely featureless, and more consistent with AFM images of the OTS SAM surfaces. The presence of a LB monolayer upon a substrate surface is typically manifested by the presence of characteristic film features such as "pinhole" defects and "island" domains within the film morphology. Examples of such features expected to be observed are shown in the AFM image presented in Figure 24. This image shows an LB monolayer of ODP-H_2 deposited in a "head-down" fashion upon a Si/SiO_2 substrate, through vertical withdrawal of the substrate from a pure H_2O subphase (at 20 mN/m surface pressure), upon which the LB monolayer was supported.

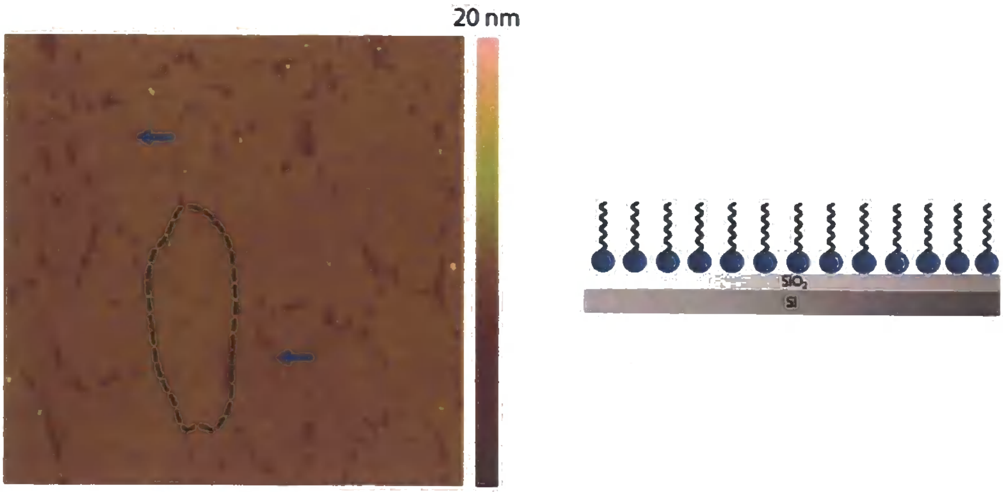

Figure 24. TappingMode^{TM} AFM image (left) of a 10 x 10 μm^2 region of ODP-H_2 LB monolayer deposited upon an Si/SiO_2 substrate at 20 mN/m surface pressure, showing pinholes defects (blue arrow) and monolayer "island" domains (dashed line). Cartoon representation of structure of the LB film, deposited in a "head-down" fashion.

In contrast, treatment of the deposited LB films in aqueous solutions containing Zr^{4+} or Hf^{4+} species resulted in a reduction in the static contact angle observed upon the substrate surfaces (74 ± 3 ° for Zr-ODP and 75 ± 3 ° for Hf-ODP respectively). This increased hydrophilic character associated with the substrate surfaces is attributed to the robust character associated with the LB film arising from the crosslinking of the metal-phosphonate surface. This associated stability prevents film detachment upon removal from the aqueous subphase, leaving a LB-modified substrate surface terminated with cationic metal species.

AFM reveals both the Zr-ODP and Hf-ODP films to be free of pinhole defects and highly uniform with a calculated rms surface roughness of 0.5 ± 0.1 nm over a 5 x 5 μm^2 region. Island features can often be identified within the film morphology (Figures 25 and 26, right hand images), which are thought to result from the initial formation of monolayer islands upon the pure H_2O subphase. Compression of the monolayer islands to the target (20 mN/m) surface pressure (during production of the π–A isotherm) forms a two-dimensional solid phase in which the islands are condensed into the final continuous film structure which is subsequently deposited upon the substrate. The interfaces between the island features in the resulting Zr-ODP and Hf-ODP LB films form only small depressions in the film surface, with no evidence of them resulting in significant defects which deeply penetrate into, or significantly disrupt the film structure. Small particulates observed upon the film surface are thought to arise from organic contamination from the environment in which the substrates are stored. The particulates are unlikely to be OTS aggregates (as observed upon the OTS SAMs) as small film defects may be expected to result around such contaminants due to the disruption they would potentially cause to the LB deposition. In contrast, the LB film appears to have a "healing" effect with the particulates originally observed upon the underlying OTS film surface not evident within the deposited film.

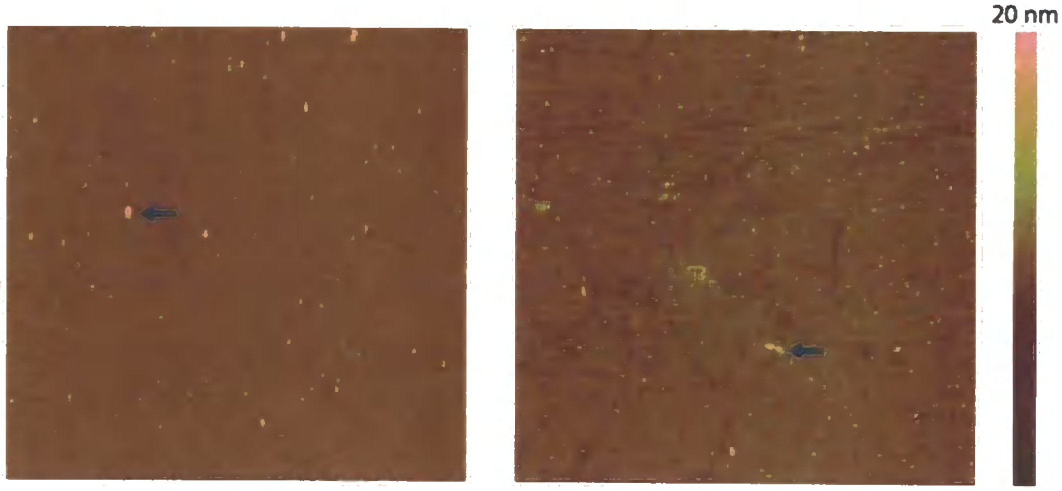

Figure 25. TappingMode™ AFM images of a 6 x 6 µm^2 (left) and 12 x 12 µm^2 (right) regions of a Zr-ODP LB film. The blue arrows highlight particulates on surface proposed to arise from organic contaminants.

Preparation of the Hf-ODP films was found to require aging of the $HfOCl_2\cdot xH_2O$ (x = 6 - 8) solution prior to metal ion assembly upon the LB surface. AFM showed the use of Hf^{4+} solutions aged over shorter time periods (1 - 4 hours) led to LB films containing significant defects which frequently exhibited a dendritic-like morphology as shown in Figure 26 (left hand image). From the AFM image, islands are also visible upon the hafnium-terminated surface areas (blue arrows), believed to be monolayer domains of ODP originating from the defective film regions, and now bound to the metal surface *via* their phosphonate headgroups.

In contrast to this, aging of the Hf^{4+} solutions for extended periods (> 36 hours) prior to metal ion assembly, yielded defect free films of comparable quality to the Zr-ODP LB films, Figure 26 (right hand image). The quality of the Zr-ODP films did not show a similar dependency upon aging of the $ZrOCl_2 \cdot 8H_2O$ solutions employed. The reason for these differences between the zirconium and hafnium solutions is not fully clear, but is thought to relate to aqueous chemistry undergone by the ionic metal species, and the differences between their kinetics of hydrolysis (and further reactions) which take place in solution. The nature of this chemistry is discussed in further detail later in this section.

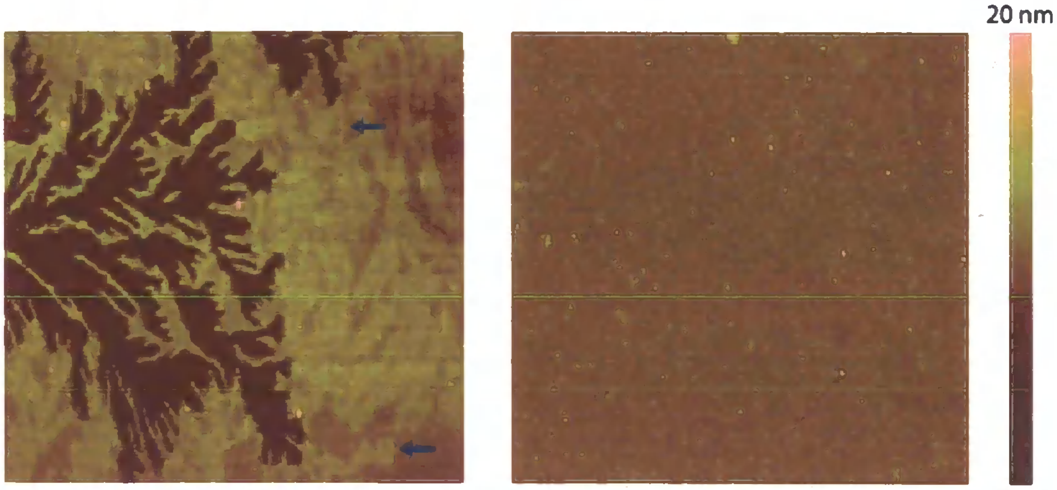

Figure 26. TappingMode™ AFM images of 6 x 6 μm^2 regions of Hf-ODP LB films, prepared using 0.5 mM aqueous solutions of $HfOCl_2 \cdot xH_2O$ (x = 6 - 8) aged for 1 hour (left) and 48 hours (right).

Film thicknesses of 4.5 ± 0.5 nm and 4.8 ± 0.4 nm were determined from ellipsometry data for the Zr-ODP and Hf-ODP LB films, respectively. These values, when considered in context of the theoretical length of an ODP-H_2 molecule (*ca.* 2.5 nm[20]), indicate that a significant contribution to the observed film thickness (*ca.* 2.0 nm) arises from the layer of metal ions bound to the LB surface. This suggests that the nature of the metal-terminated surface produced from the procedures employed here, differs to the monolayer of Zr^{4+} ions bound at the LB monolayer surface reported by Talham and coworkers.[90]

The formation of the two different zirconium film structures may be rationalised when considering the complex nature of aqueous zirconium chemistry. The formation of polymeric Zr-O structures readily occurs, arising from the highly charged nature of the Zr^{4+} ions, which leads to rapid hydrolysis, typically followed by polymerisation. In particular, the hydrolysis of $ZrOCl_2$ to form the hydroxyl bridged tetrameric cation $[Zr_4(OH)_8(H_2O)_{16}]^{8+}$ is known, Figure 27.[212] The occurrence and extent of polymerisation however is reported to be dependent upon several parameters including metal concentration, solution pH, temperature, and aging of solutions.[213,214] It is thus thought that zirconium solutions prepared in these studies (0.5 mM solutions, prepared in 18 MΩ cm H_2O) show a preference for the formation polymeric zirconium species. Though studies into the aqueous chemistry of hafnium prove rare, it is generally believed to be governed by the formation of oligomer structures, such as the $[Hf_4(OH)_8(H_2O)_{16}]^{8+}$ tetramers,[211] in a similar fashion to aqueous zirconium chemistry.

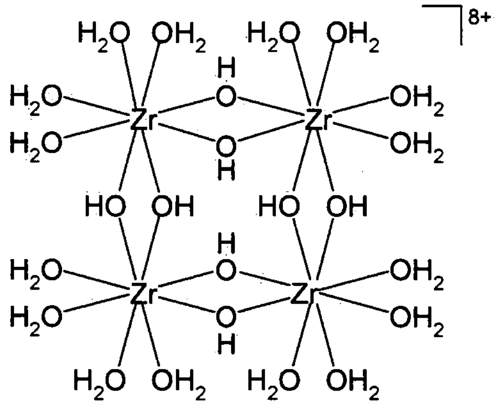

Figure 27. Structure of tetrameric zirconium species reported to form upon hydrolysis of aqueous solutions of $ZrOCl_2{\cdot}8H_2O$.[212]

Further evaluation of the thickness of the metal-ODP films by AFM was carried out through depositing LB films at reduced surface pressures (10 mN/m) to deliberately introduce defects into the film structure. Assuming the defects penetrate through the entire film structure, determination of the depth of these defects can be used to provide an indication of the metal-ODP film thickness.

Figure 28 shows an AFM image of a Zr-ODP film prepared at the reduced surface pressure value. The film morphology can be seen to comprise of a series of island domains inefficiently packed together, resulting in significant defects at the island - island interfaces (blue arrows). A significant number of "pinholes" (red arrows) are also clearly visible throughout the film structure.

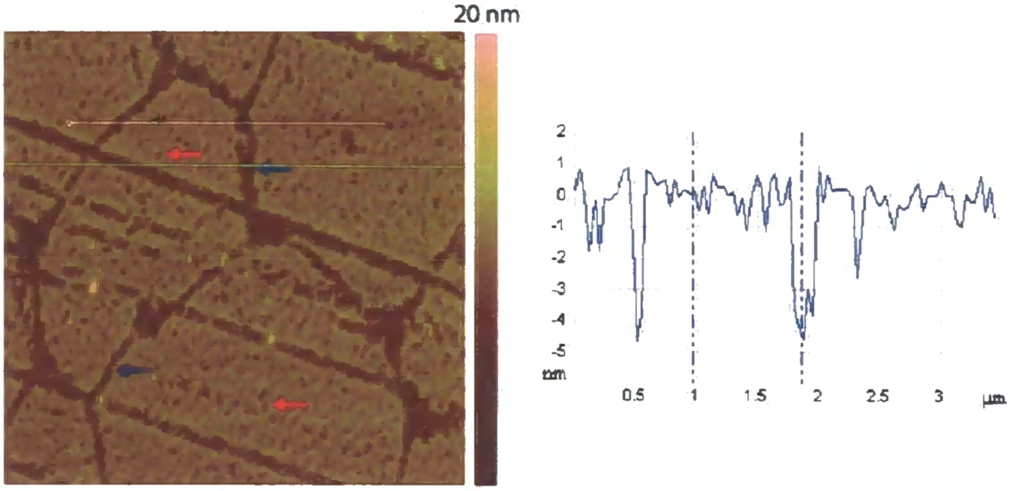

Figure 28. TappingMode^{TM} AFM image (left) of a 5 x 5 µm^2 region of a defective Zr-ODP LB film deposited at a reduced surface pressure (10 mN/m), and a corresponding cross section (right) of the film.

The depths of the defects range from *ca.* 1.7 - 4.7 nm throughout the film, and are attributed to differing levels of disorder (or a complete absence) of ODP-H_2 molecules within these regions, Figure 29. Pinholes in the film showed a tendency to exhibit less prominent defects (1.7 ± 0.2 nm), suggesting ODP-H_2 molecules remain in these regions, but in a disordered fashion and orientated in a manner that inhibits metal binding to the ODP-H_2 headgroups (Figure 29, defects A and C). The depth of these defects is dependent upon the degree of disorder and the orientation of the ODP-H_2 molecules present in the region.

More prominent defects (up to 4.6 ± 0.2 nm) are observed when the ODP-H_2 molecules are highly disordered, either lying highly tilted upon the substrate surface, or being absent altogether (Figure 28, defects C and B). Defects of this nature were commonly observed at the interfaces between the Zr-ODP island domains. Assuming a complete absence of ODP-H_2 molecules at the maximum defect depths observed (4.8 nm) this corresponds to the presence of a 2.2 nm zirconium layer bound at the LB monolayer surface.

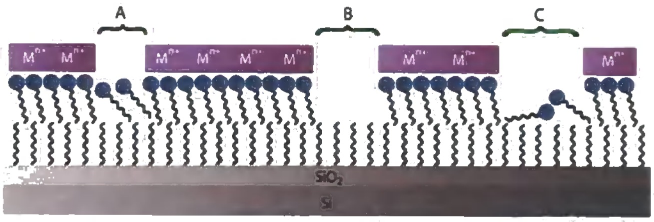

Figure 29. Schematic representation of defective metal-ODP LB film deposited upon a Si/SiO_2-supported OTS monolayer, highlighting the three types of defects observed in films deposited at reduced surface pressures (10 mN/m).

Similarly, in the case of the ionic hafnium species binding to defective films, pinholes were again observed throughout the film, as well as inefficient packing of the Hf-ODP island domains. The pinholes observed within the island domains (Figure 30, red arrows), appeared less invasive than those observed in the defective Zr-ODP film, typically penetrating < 0.5 nm into the film structure. However, more variation in the nature of the defects between the island domains of the Hf-ODP film was found, with two types of principal defects identified. The more commonly observed defects occurred at the interfaces between the islands (Figure 30, blue arrow), typically penetrating 2.2 ± 0.2 nm into the film structure. The depth of these defects lies in close agreement with the expected thickness of the Hf layer, suggesting that the defects do not extend into the underlying ODP monolayer. Higher levels of ordering of the ODP-H_2 molecules present in these defects is indicated by the lower depths in comparison to the corresponding defects observed at the island - island interfaces in the Zr-ODP films (up to 4.6 ± 0.2 nm).

The presence of ordered ODP-H_2 molecules in these regions in the Hf-ODP film may be the result of a limited degree of binding of the ionic hafnium species to the LB film surface. This may provide sufficient stabilisation to prevent loss, or disordering, of the ODP-H_2/ODP-Hf species in these regions of the LB film upon its removal from solution. However, despite this apparent increase in molecular order (and limited metal binding), the headgroups of the ODP-H_2 molecules appear to remain unavailable for efficient growth of a more substantial hafnium-derived film in these regions.

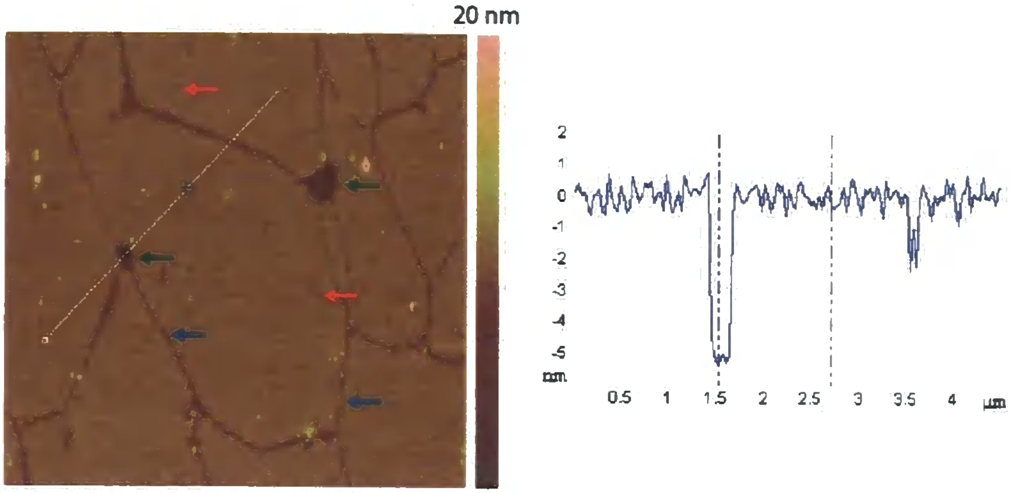

Figure 30. Contact mode AFM image (left) of 6 x 6 µm^2 region of defective Hf-ODP LB film deposited at a reduced surface pressure (10 mN/m) upon an OTS-modified Si/SiO_2 substrate. Blue and green arrows highlight the presence of island-island interface and junction defects, respectively, observed throughout the film. The red arrows highlight pinholes present in the film structure. A cross section (right) of the defective film shows the depths with which the defects extend into the LB film structure.

The second type of defect observed in these inter-island regions are more disruptive to the film structure, and are typically located at "junctions" between where two or more of the island-island interface defects (as just discussed) adjoin one another, as highlighted in Figure 30 (green arrows). These defects typically extend 5.1 ± 0.2 nm into the film structure, and correspond to the expected combined thickness of the hafnium layer and underlying ODP monolayer. This suggests that there to be a complete absence of ODP-H_2 molecules in these junction defects. It is thought that ODP-H_2 molecules may initially be present in these regions following LB deposition, but are again highly disordered preventing hafnium binding. The resulting absence of any film stabilisation (typically provided by the crosslinking hafnium species) leads to film degradation in these regions upon removal from solution. Alternatively, inefficient packing of the ODP-H_2 island domains upon the pure H_2O subphase during the initial Langmuir monolayer formation (due to the reduced surface pressure employed) may result in failure of the ODP-H_2 molecules being transferred to the substrate in these junctions during LB deposition. Suggestions that the junction defects span the full film thickness are supported by the ellipsometry data previously discussed, from which a film thickness of 4.8 ± 0.4 nm was determined. The contribution to the Hf-ODP film thickness from the hafnium layer (*ca.* 2.3 nm, based upon the junction defect depths) also proves highly consistent with the hafnium layer thickness indicated from the island-island interface defects (2.2 ± 0.2 nm).

The consistency between the zirconium and hafnium layers formed is apparent from these AFM studies of the defective films, with both the $ZrOCl_2{\cdot}8H_2O$ and $HfOCl_2{\cdot}xH_2O$ (x = 6 - 8) solution treatments of the ODP-H_2 LB films resulting in the growth of a *ca.* 2.2 nm metal ion layer upon the LB film surface.

Further evidence for the presence of more complex zirconium and hafnium species upon the LB the film surface (in contrast to the formation of simple monolayer of tetravalent Zr^{4+}/Hf^{4+} metal ions) was provided by XPS analysis. XPS data of the Zr-ODP films confirms the presence of carbon (C 1s, 285.0 eV), oxygen (O 1s, 532.1 eV), phosphorus (P $2p_{3/2}$, 133.8 eV), and zirconium (Zr $3d_{3/2}$, 183.7 eV, $3d_{5/2}$, 185.7 eV) in the Zr-ODP with binding energies referenced to the hydrocarbon C1s peak at 285.0eV. An excess of zirconium in the sample, as shown from the Zr : P ratio (*ca.* 2 : 1), further supports the existence of the surface-bound zirconium in a more complex form than the previously observed by Talham. Similarly, XPS confirmed the presence of carbon (C 1s, 285.0 eV), oxygen (O 1s, 532.5 eV), phosphorus (P $2p_{3/2}$, 133.6 eV), and hafnium (Hf $4f_{5/2}$, 17.5 eV, Hf $4fd_{7/2}$, 18.9 eV) in the corresponding Hf-ODP films. The hafnium peaks positions are in close agreement to those of HfO_2 (Hf $4f_{7/2}$ 17.3 eV, Hf $4f_{5/2}$, 18.9 eV)[215] with the hafnium metal in the +4 oxidation state. Hafnium is not shown to be in excess relative to the ODP molecules (Hf/P ratio = *ca.* 1:1) as observed in Zr-ODP systems. This value is does not correspond well with previous ellipsometry data and AFM data (discussed later in this section) which suggest the hafnium to be present in a more complex multilayered structure, in a similar vein to the zirconium surfaces discussed here. It should be noted however that estimation of phosphorus concentration can be difficult as its peaks position overlaps with the silicon loss peak. This can lead to overestimation of the P concentration and hence reduce the calculated Hf to P ratio.

Further probing of the structure of the assembled metal ion layer was carried out by quartz crystal microbalance (QCM) measurements of Zr-ODP LB films, deposited upon an OTS-modified quartz crystal. A LB film mass of 0.707 μg cm^{-2} was calculated, of which 2.247×10^{-7} g cm^{-2} could be assigned to the ODP monolayer if assuming a molecular area of 24.7 $Å^2$ for each ODP molecule (as determined from Langmuir isotherm studies). The remaining film mass (4.823×10^{-7} g cm^{-2}) attributed to the capping layer, corresponds to an ODP to $[Zr(OH)_2(H_2O)_4]_4^{8+}$ tetramer ratio of 1 : 0.9 (*i.e. ca.* 4 zirconium atoms for each ODP molecule present). In comparison, if we carry out the modeling of the metal capping layer as monolayer of Zr^{4+} ions as put forward by Talham,[90] an ODP to Zr ratio of 1 : 7.9 is calculated, which is very different to the 1 : 1 ratio expected if the Talham monolayer model is correct.

3.2.2.1 Multilayer metal-octadecylphosphonate Langmuir-Blodgett films

To provide a comprehensive study into the structure of these metal-ODP films, multilayer Zr-ODP and Hf-ODP films, each consisting of seven repeat bilayers, were prepared through sequential "Y-type" LB deposition of ODP monolayers, Figure 31.

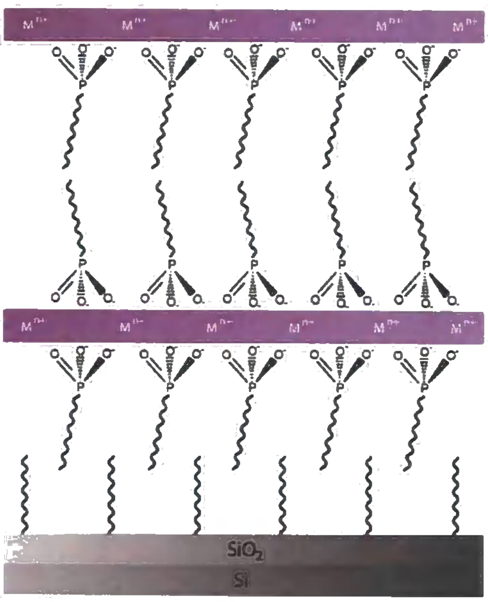

Figure 31. Idealised structure of a Y-type multilayer metal-ODP LB film, supported upon an OTS-modified Si/SiO_2 substrate, showing first three LB layers deposited.

Successful formation of the multilayer film was confirmed from ellipsometry data showing a linear increase in the total film thickness, following each bilayer deposition, Figure 32. Modelling of the multilayer film as a simple repeat bilayer structure, in which tilt associated with the alkyl chains of the ODP molecules is discounted, an average bilayer spacing of 6.5 nm and 6.6 nm was determined for the Zr-ODP and Hf-ODP films, respectively from linear fits of the ellipsometry data. These values indicate a significant contribution (*ca.* 1.5/1.6 nm) to the bilayer thickness arises from the inorganic metal ion film components.

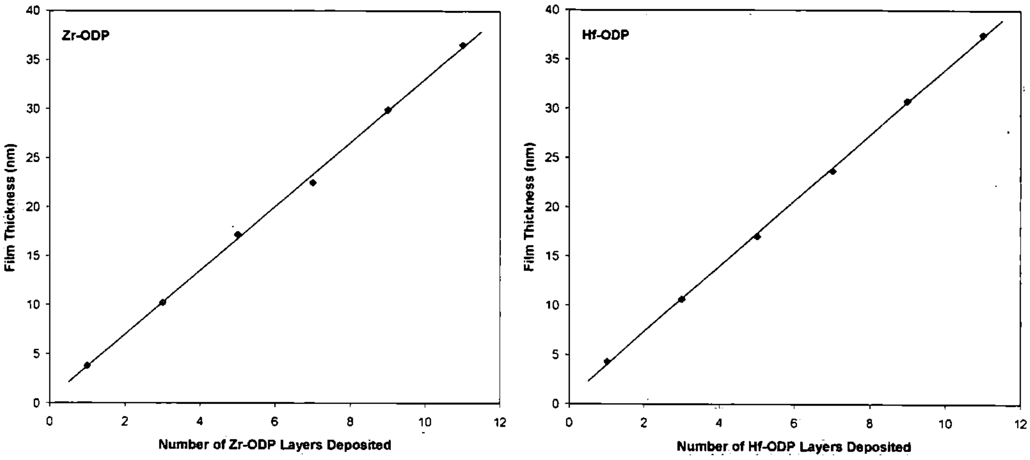

Figure 32. Film thicknesses determined from ellipsometry data recorded following each Y-type deposition of Zr-ODP (left) and Hf-ODP (right) LB bilayers, during the production of multilayer metal-ODP films.

Further probing of the film structure and determination of the film periodicity was carried out using X-ray reflectometry (XRR). Three Bragg peaks are observed in the XRR spectrum of the multilayer Zr-ODP film, representing orders of the (00*l*) reflection at $q = 0.102$ Å^{-1} (001), $q = 0.209$ Å^{-1} (002), and $q = 0.313$ Å^{-1} (003), Figure 33. The difference in q-space ($d = 2\pi/\Delta q$) between each Bragg peak corresponds to a d-spacing of 6.0 nm, a value which is in reasonable agreement with ellipsometry data of the multilayer film, and suggesting a contribution to the bilayer thickness of *ca.* 1.0 nm from the zirconium film component. Although these ellipsometry and XRR values appear low in comparison to ellipsometry data from a singly deposited Zr-ODP monolayer, it should be noted that these modelling calculations do not take into consideration the orientation and potential tilt of the alkyl chains relative to the surface normal. The likely occurrence of molecular tilt within the bilayer structures is expected to result in a true thickness value for the Zr^{4+} layer closer to that obtained from the ellipsometry data of the singly deposited LB film.

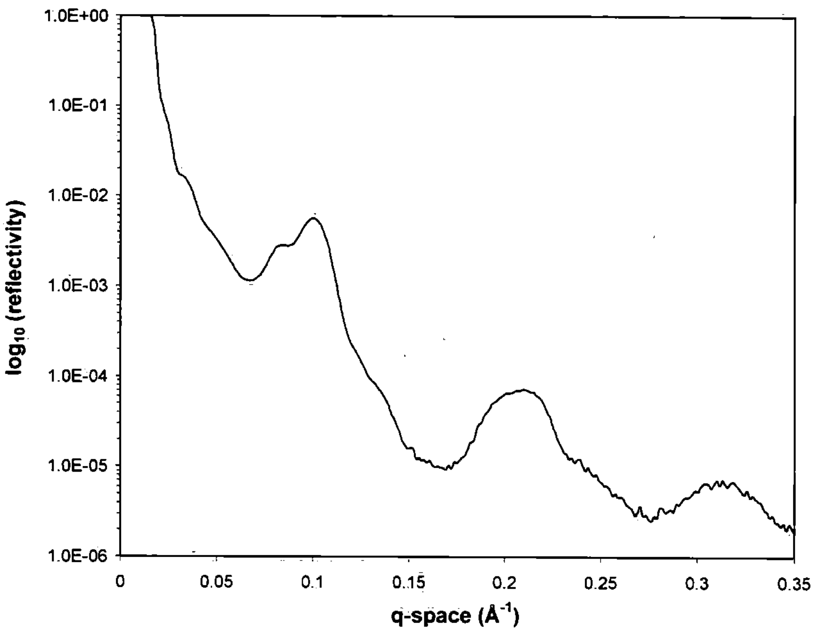

Figure 33. XRR data obtained from a Y-type multilayer Zr-ODP LB film, consisting of seven repeat bilayers, showing three Bragg peaks at q-space values of 0.102 Å^{-1}, 0.209 Å $^{-1}$, and 0.313 Å $^{-1}$ respectively.

Similarly, the two Bragg peaks shown in the XRR spectrum of the Hf-ODP multilayer film (q-space = 0.121 Å^{-1} (001), and q = 0.228 Å^{-1} (002) reflection), show a q-space separation consistent with a d-spacing of 5.9 nm, Figure 34. Fitting of these data to the multilayer film model previously discussed, suggests a Hf layer of *ca.* 0.9 nm in the ODP-Hf film stucture. As observed in the production of Zr-ODP multilayer films, the calculated thickness of the hafnium ion layer is lower than that determined from the corresponding singly deposited Hf-ODP monolayers. This smaller calculated thickness value is again accounted for by any tilt that is associated with the alkyl chains in the Hf-ODP layers having not been considered in the multilayer film model.

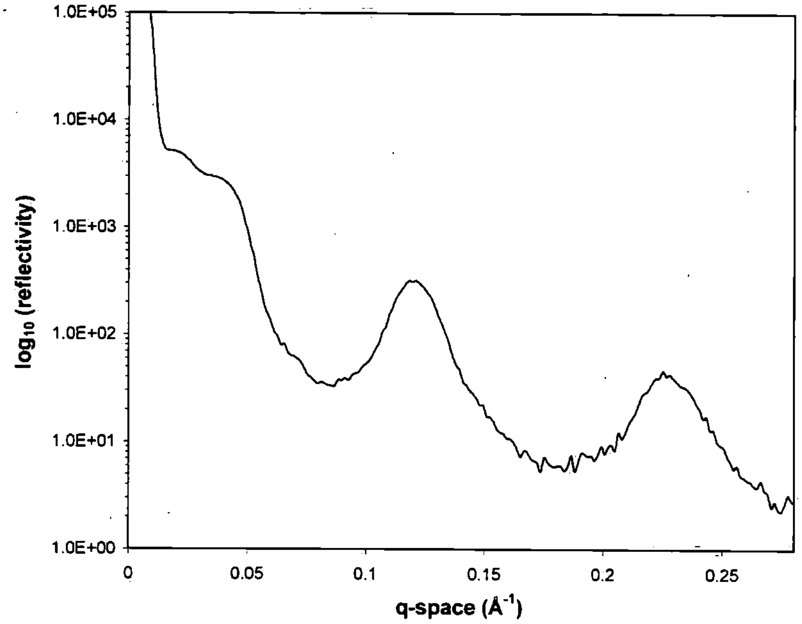

Figure 34. XRR data obtained from a Y-type multilayer LB film, consisting of seven repeat Hf-ODP bilayers, showing two Bragg peaks at q-space values of 0.121 $Å^{-1}$, and 0.228 $Å^{-1}$.

Specular reflectance FTIR spectra provided chemical evidence of the presence of the ODP in the multilayer film structures, with the Zr-ODP (Figure 35) and Hf-ODP (see Appendix 1) multilayer films both showing bands arising from asymmetric CH_3, asymmetric CH_2, and symmetric CH_2 stretches in the alkyl chains of the ODP molecules, Table 1.

Table 1. Bands resolved in specular reflectance FTIR spectra of multilayer (seven repeat bilayers) Zr-ODP and Hf-ODP LB films deposited upon an OTS-modified Si/SiO$_2$ substrate, and "full width half maximum" of the asymmetric CH$_2$ stretches shown.

	Zr-ODP	**Hf-ODP**
ν_s (CH$_2$)	2850 cm^{-1}	2850 cm^{-1}
ν_a (CH$_2$)	2918 cm^{-1}	2918 cm^{-1}
ν_a (CH$_3$)	2954 cm^{-1}	2954 cm^{-1}
fwhm, ν_a (CH$_2$)	18 cm^{-1}	17 cm^{-1}

The position of the ν_a (CH$_2$) band and its "full width at half-maximum" (fwhm) value can also be used to interpret the conformational order of the alkyl chains of the ODP molecules. Typical ν_a (CH$_2$) band frequencies range from 2918 cm^{-1}, indicating a solid crystalline phase, to 2924 cm^{-1} which suggest the alkyl chains to be of a liquid-like phase.[216] Comparison of the position of the ν_a (CH$_2$) bands, in both the Zr-ODP and Hf-ODP spectra (both at 2918 cm^{-1}), to this frequency range indicates a crystalline solid phase. The fwhm of the ν_a (CH$_2$) bands are determined to be 18 cm^{-1} and 17 cm^{-1} for the Zr-ODP and Hf-ODP films respectively, indicating close packing of the alkyl chains in both multilayer films.[123]

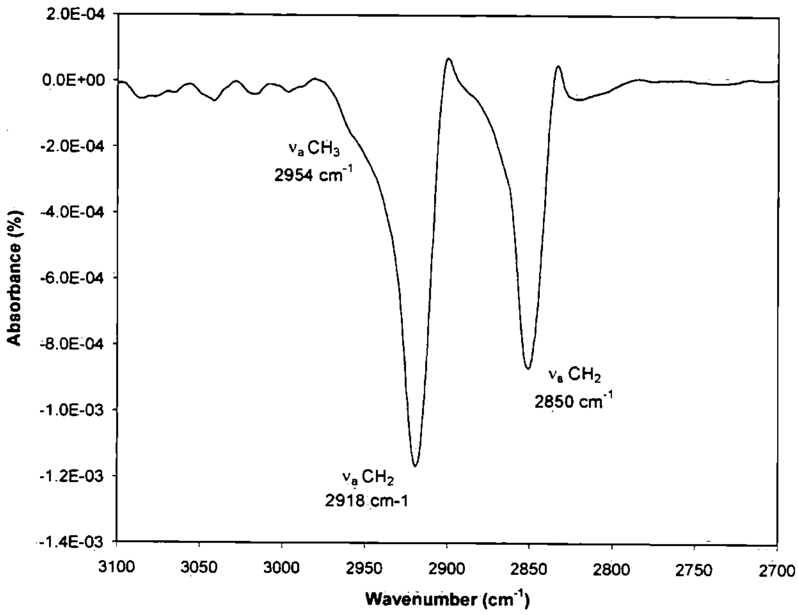

Figure 35. Specular reflectance FTIR spectrum of a Y-type multilayer LB film of seven repeat Zr-ODP bilayers, showing bands resolved at 2954cm^{-1} (asymmetric CH_3 stretch) and 2850 cm^{-1} (symmetric CH_2 stretch) and 2918 cm^{-1} (asymmetric CH_2 stretch).

3.2.3 Ultra-thin metal oxide films

The observed formation of inorganic polymeric films of zirconium and hafnium through metal ion assembly upon phosphonate-terminated LB film surfaces potentially provides a route to the generation of metal oxide films of nanometre thickness, Scheme 4. High temperature treatment (500 °C) was found to successfully lead to decomposition of the organic components of the film leaving behind a thin metal oxide (ZrO_2, HfO_2) film upon the substrate surface, formed by calcination of the polymeric zirconium/hafnium structures.

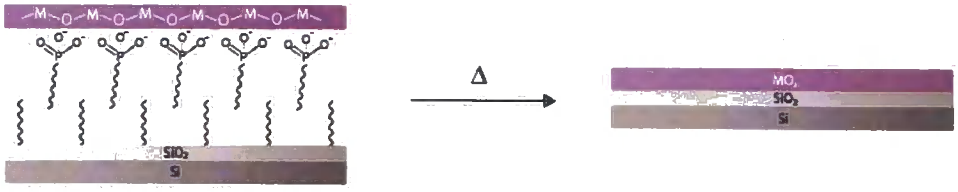

Scheme 4. Schematic representation of the formation of thin metal oxide films by thermal treatment of metal-ODP LB films, used to simultaneous decompose organic film components, and calcine the inorganic layer generating the metal oxide.

AFM shows the thermally treated films to be of low surface roughness (rms roughness of 0.4 ± 0.1 nm over a 5 x 5 μm^2 region for both the ZrO_2 and HfO_2 surfaces), exhibiting good structural retention, with the condensed island features observed in the initial organic-inorganic persisting in the resulting oxide film, Figure 36. No additional defects are observed to arise in the film structures as a consequence of the thermal treatment. Variation in the duration of the thermal step, from 2 - 16 hours, was found to have no noticeable effect upon the film quality. Static contact angle values reveal the thermally treated surfaces to be highly hydrophilic (ZrO_2: 32 ± 3°, HfO_2: 28 ± 3°), as expected for such metal oxide surfaces (which would be expected to bear hydroxyl groups at the film periphery).

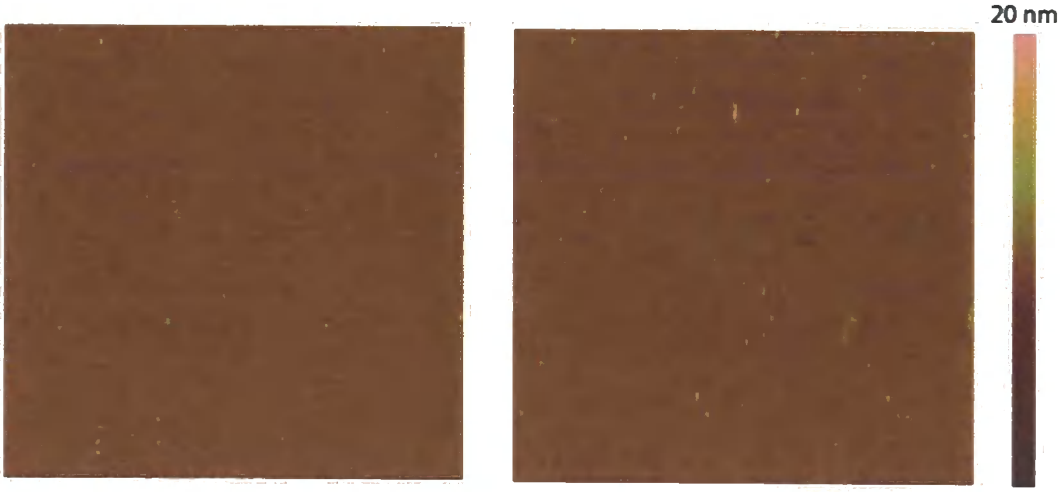

Figure 36. TappingMode™ AFM images of a 5 x 5 μm^2 region of a ZrO_2 film (left) supported upon a Si/SiO_2 substrate, and a 6 x 6 μm^2 region of a HfO_2 film (right) supported upon a Si/SiO_2 substrate, both formed following thermal treatment (500 °C) of the corresponding metal-ODP LB monolayer.

The thicknesses of the metal oxide films were determined from AFM analysis of defective Zr-ODP and Hf-ODP (deposited at 10 mN/m surface pressure) films previously described, following thermal treatment (500 °C). High levels of structural retention are observed in the resulting metal oxide films, with the island morphology and pinhole defects in the initial LB films remaining following thermal treatment, Figures 37 and 38.

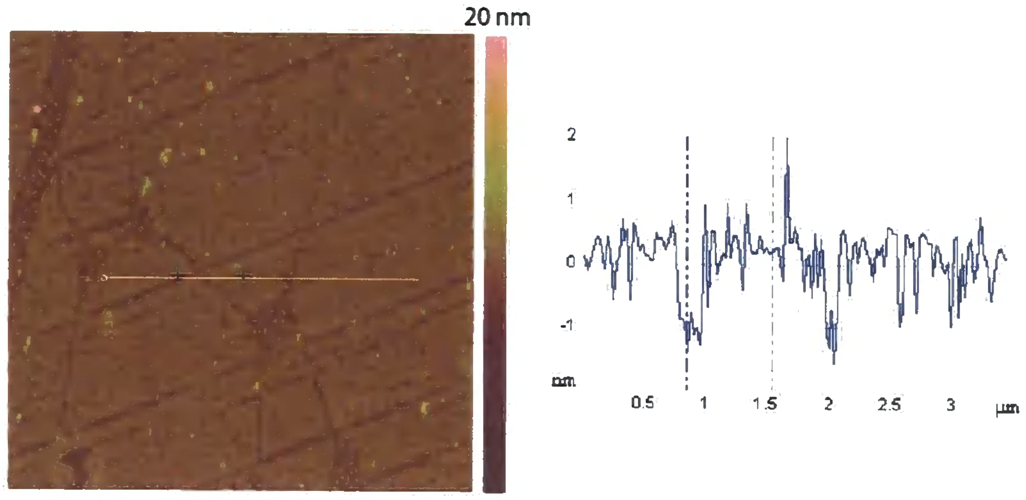

Figure 37. TappingMode™ AFM image (left) of a 5 x 5 µm^2 region of a defective ZrO_2 film upon a Si/SiO_2 substrate, formed following thermal treatment (500 °C) of a defective Zr-ODP LB monolayer deposited at a reduced surface pressure (10 mN/m), and the corresponding cross section (right) of the ZrO_2 surface.

The depth of the defects in the thermally treated ZrO_2 and HfO_2 surfaces, indicate the loss of the organic film components, leaving a calcined metal oxide film of 1.7 ± 0.2 nm (ZrO_2) and 1.5 ± 0.2 nm (HfO_2, Figure 38) thickness. Previous studies (XPS, AFM, thermogravimetric analysis) into the thermal stability of alkylsilane monolayers have shown the decomposition of the organic monolayers to take place through pyrolysis of the hydrocarbon moieties, *via* cleavage of the C–C and Si–C bonds above 220 °C.[217] The loss of the siloxane headgroups of the alkylsilane molecules, from the substrate surface, was also shown to occur at temperatures above *ca.* 480 °C. The thermal decomposition of alkylphosphonic acid monolayers, bound to metal oxide substrates (through the formation of surface phosphonates) has similarly been reported to occur through C–C and P–C bond cleavage, with the the inorganic headgroups remaining present upon the substrate surface at temperatures above *ca.* 450 °C (presumed to be as phosphates).[218] However, when considering this in context of the current studies, it should be noted that the alkylphosphonic acid monolayers (with the headgroup bound to the substrate surface) described by McElwee *et al.*[218] are distinct from the metal-ODP LB monolayers prepared here, where there are no bonding interactions between the substrate surface and ODP headgroup.

The reduction in the film thicknesses following thermal treatment (assuming the ODP molecules provided a 2.5 nm contribution[20] to the Zr-ODP and Hf-ODP film structures) suggests to a small degree of contraction (*ca.* 0.5 nm) is also associated with the calcined inorganic film structure.

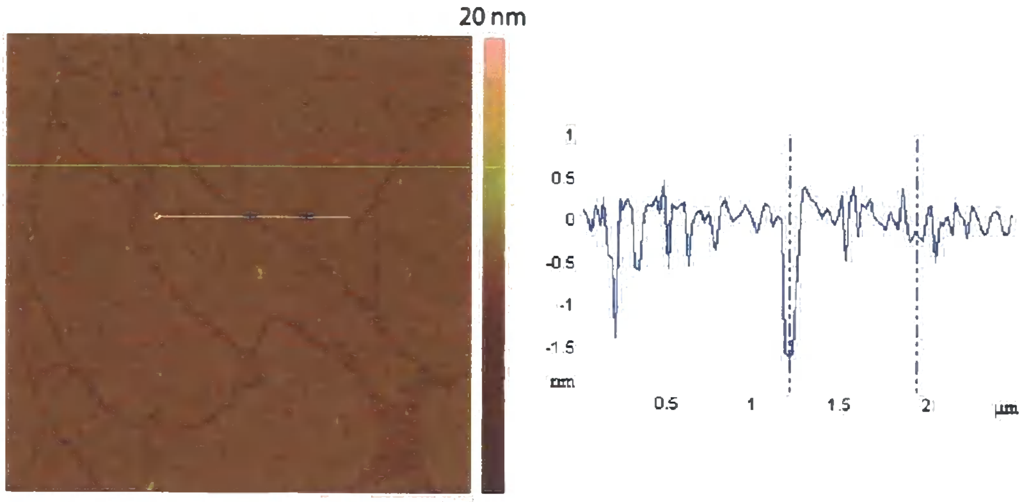

Figure 38. Tapping mode AFM image (left) of a 6 x 6 µm^2 region of a defective HfO_2 film upon a Si/SiO_2 substrate, formed following thermal treatment (500 °C) of a defective Hf-ODP LB monolayer, deposited at a reduced surface pressure, upon an OTS-modified Si/SiO_2 substrate, and a cross section (right) of the HfO_2 surface.

To provide chemical identification of the calcined films, XPS was carried out upon the thermally treated surfaces. XPS confirms zirconium (Zr $3d_{3/2}$, 185.4 eV, $3d_{5/2}$, 183.1 eV) remains present at the substrate surface following thermal treatment of the Zr-ODP LB films, and proves in excellent agreement with the binding energies of the Zr

3d signals arising from a ZrO_2 sample (Zr $3d_{3/2}$, 185.3 eV, Zr $3d_{5/2}$, 182.9 eV).[219] Likewise, XPS analysis of HfO_2 films confirms the presence of hafnium (Hf $4f_{5/2}$, 17.9 eV, Hf $f_{7/2}$, 19.4 eV), with the binding energies again proving in good agreement with the metal oxide, HfO_2 (Hf $4f_{5/2}$ 19.8 eV, $4f_{7/2}$ 17.9 eV).[220] The XPS spectrum also shows a weak P 2s signal (and possibly P 2p) indicating the presence of residual phosphorus in the sample believed to originate from the phosphonate headgroups present in the ODP monolayer.

From the XPS data, the close matches between the binding energies of the Zr and Hf signals in the respective thermally treated Zr-ODP and Hf-ODP films, to those reported in bulk ZrO_2 and HfO_2, provides a strong indication of the successful metal oxide formation. Attempts to obtain further evidence to support metal oxide formation, and elucidate information regarding the phase of the ZrO_2 and HfO_2 by grazing angle X-ray diffraction (XRD) proved unsuccessful, probably as a result of the small amount of material present on the substrate surface, and the lack of suitably sensitive equipment.

Indirect evidence of metal oxide formation was obtained however, using variable temperature XRD studies of the metal precursor materials, $ZrOCl_2{\cdot}8H_2O$ and $HfOCl_2{\cdot}xH_2O$ (x = 6 - 8) (following their exposure to water and subsequently redried). The XRD data of the $ZrOCl_2{\cdot}8H_2O$ sample shows the onset of crystallisation of tetragonal (high temperature form) ZrO_2 at *ca.* 290 °C with peak sharpening (tetragonal (111) reflection at 30.2 °) on warming to 900 °C,[221] Figure 39. Upon cooling back to room temperature both the monoclinic (as evidenced by monoclinic (200) and (-201) peaks at $2\theta = 34.4\ ^{\circ}$ and $2\theta = 35.1\ ^{\circ}$ respectively) and tetragonal forms of ZrO_2 are present.[222]

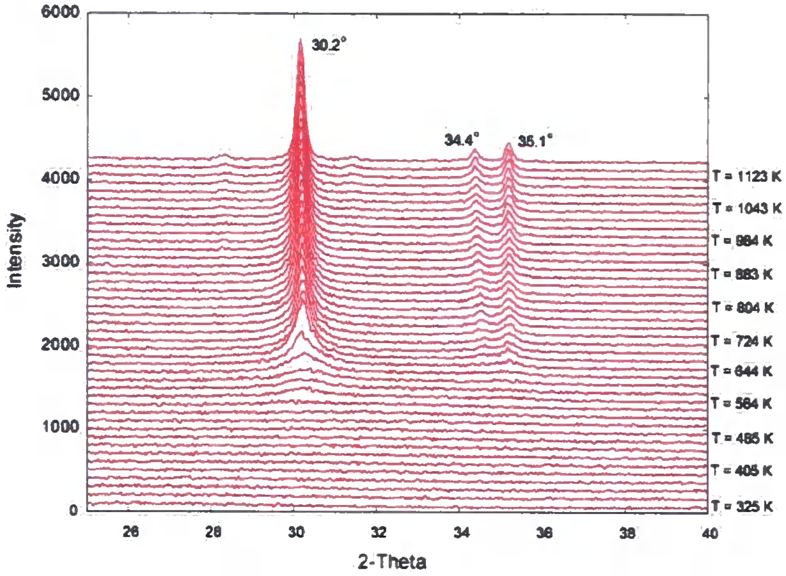

Figure 39. XRD pattern of $ZrOCl_2.8H_2O$ at variable temperature ranging from T = 325 - 1163 K. The presence of tetragonal and monoclinic ZrO_2 phases are confirmed by the presence of the tetragonal (111), monoclinic (200), and monoclinic (-201) reflections at 30.2°, 34.4°, and 35.1°, respectively.[221,222]

The XRD studies of the $HfOCl_2{\cdot}xH_2O$ (x = 6 - 8) sample show the onset of crystallisation of a monoclinic phase HfO_2 to occur at *ca.* 390 °C, with the growth of peaks at $2\theta = 24.2\,^{\circ}$ (011), 28.4 ° (-111), 31.5 ° (111), 34.1 ° (200), 34.7 ° (020), and 35.5 ° (002) respectively.[223,224]

The phases observed in the crystallised ZrO_2 and HfO_2 (from the $ZrOCl_2.8H_2O$ and $HfOCl_2.xH_2O$ precursor compounds) may provide an indication to the phase of the ZrO_2 and HfO_2 films produced following thermal treatment of the Zr-ODP and Hf-ODP LB films.

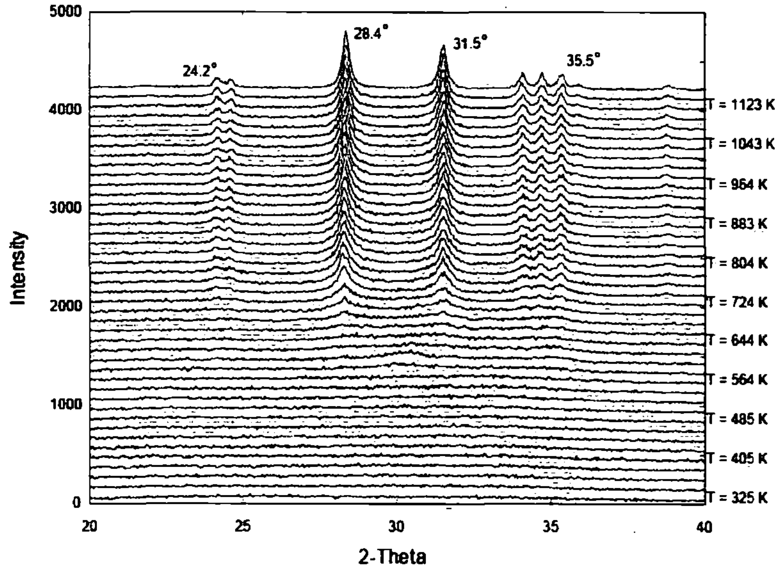

Figure 40. XRD pattern of $HfOCl_2.xH_2O$ (x = 6 - 8) at variable temperature ranging from T = 325 - 1163 K. Sharpening of the reflections including the monoclinic (011), (-111), (111), (200), (020) and (002) reflections at 24.2 °, 28.4 °, and 31.5 °, 34.1 °, and 34.7°, and 35.5 ° respectively confirms the onset of crystallisation of a monoclinic HfO_2 phase at *ca.* 390 °C.

3.4 Conclusions

A facile method to produce nanometre thick metal oxide films of zirconium and hafnium has been described here, exploiting aqueous chemistry of hafnium and zirconium and their tendency to form polymeric structures in solution, in conjunction with LB film deposition procedures. LB monolayers of ODP-H_2, deposited upon OTS-modified Si/SiO_2 substrates, were employed to provide a PO_3H_2-functionalised surface suitable for subsequent metal ion binding. The tendency of Zr^{4+} and Hf^{4+} ions to readily hydrolyse and form polymeric structures in solution results in the growth of nanometre thick (determined by AFM data as a 2.2 ± 0.4 nm Zr layer, and 2.5 ± 0.4 nm Hf layer) layers of the metal ions upon the LB film surface.

AFM reveals high temperature treatment leads to a reduction in the film thickness (Zr-ODP: 1.7 ± 0.2 nm, Hf-ODP: 1.5 ± 0.2 nm), attributed to decomposition of the organic film components. Simultaneously calcining of the inorganic metal ion layer during the thermal treatment leads to the formation of highly smooth, low defect metal oxide films. Confirmation of the presence of zirconium and hafnium species at the substrate surface following thermal treatment was shown in XPS studies, with the binding energies of both the Hf and Zr proving in close agreement for those expected for the bulk ZrO_2 and HfO_2 samples, indicating successful formation of the metal oxide. Although direct XRD analysis of the thermally treated films (to probe the phase of the metal oxide films) was not successful, variable temperature XRD studies upon the metal precursor materials used during LB preparation, provided indirect evidence to suggest the formation of monoclinic and tetragonal phase ZrO_2, and HfO_2 forming in a monoclinic phase.

The methods described here for metal oxide film formation prove procedurally simple, and without the need for expensive equipment (*e.g.* high vacuum equipment used in chemical vapour deposition process of similar metal oxide films), whilst also offering the potential to be carried out in a parallel fashion for large scale production. All these benefits add to this technique being a potentially economically sound route to the production of thin films of ZrO_2 and HfO_2. The production of such metal oxide films of zirconium and hafnium respectively, with the high dielectric properties these materials typically offer, makes such films a potentially viable option for use as gate oxide materials in future generations of nanoscale transistor devices.

Chapter 4

4. *Preparation of ultra-thin magnesium oxide films*

4.1 *Introduction*

The tendency of zirconium and hafnium compounds to form polymeric structures in aqueous solution has proved advantageous for the growth of nanometre-thick metal ion films upon Langmuir-Blodgett (LB) monolayers, and subsequent metal oxide formation by calcining the metal layer, see Chapter 3. The scope for production of further metal oxide films using this methodology is proposed to be dependent upon a metal species ability to polymerise in solution. Organo-metal compounds, such as those commonly employed in sol-gel processes, may satisfy this criteria.

Here, the production of magnesium-octadecylphosphonate (Mg-ODP) LB films is investigated as a precursor to the generation of thin MgO films upon Si/SiO_2 supports. Comparative studies are made into the production of films using two alternative magnesium compounds, which exhibit different aqueous chemistry. Initial attempts to stabilise LB films of octadecylphosphonic acid ($ODP\text{-}H_2$) were carried out using $Mg(NO_3)_2 \cdot 6H_2O$ as a source of Mg^{2+} ions, known to exist as the $[Mg(H_2O)_6]^{2+}$ species in aqueous solutions.[225] Subsequent investigations focussed upon the use of $Mg(OEt)_2$, and its ability to readily undergo hydrolysis and polymerisation in aqueous solutions, to "grow" sol-gel films of magnesium hydroxide (magnesia), upon the LB films.

4.2 Mg^{2+}-derived magnesium oxide films

4.2.1 Magnesium-octadecylphosphonate Langmuir-Blodgett monolayers

In contrast to Zr-ODP and Hf-ODP production (see Chapter 3) Mg-ODP LB films were prepared with Mg^{2+} ions incorporated directly into the aqueous subphase, Scheme 5. In contrast to ODP-H_2 monolayers prepared upon Zr^{4+} subphases (which result in highly inefficient LB deposition due to the rigid nature of the resulting Zr-ODP Langmuir monolayer[226]), efficient LB deposition of ODP-H_2 monolayers prepared upon aqueous subphases of divalent metal ions (Mn^{2+}, Mg^{2+}, Ca^{2+}, Cd^{2+}) can be achieved by using appropriate subphase pH conditions (typically in the pH range 5.2 - 8.1).[86]

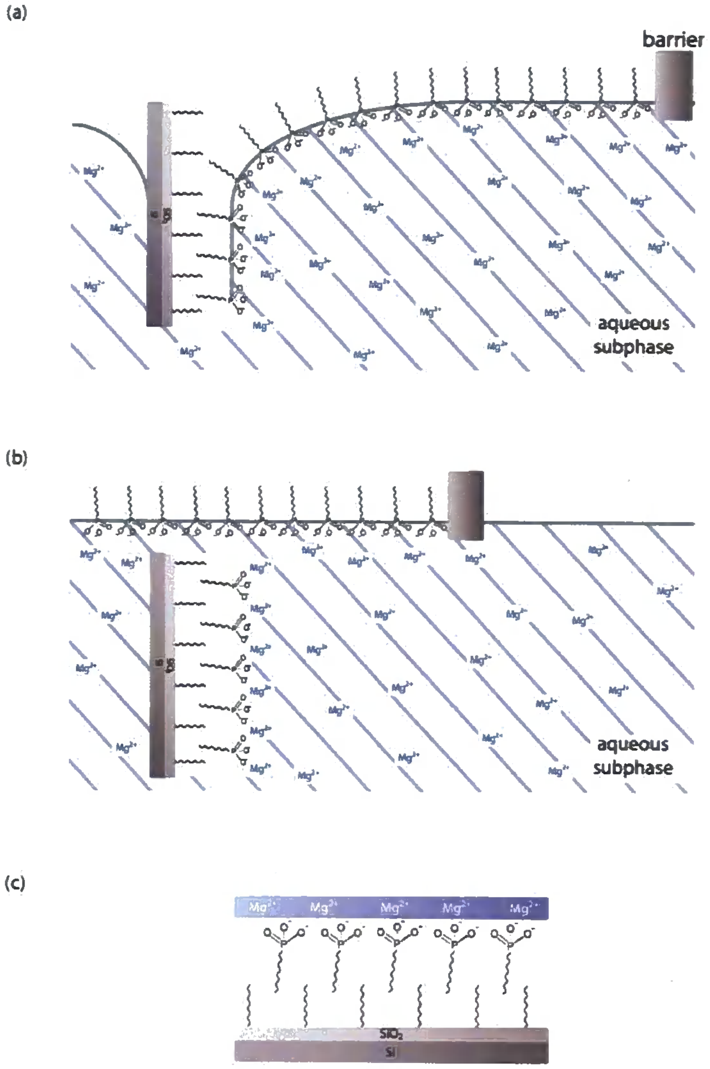

Scheme 5. Cartoon representation of the preparation of Mg-ODP LB films upon OTS-modified Si/SiO$_2$ substrates: (a) An OTS-modified Si/SiO$_2$ substrate is passed vertically downwards through a Langmuir monolayer of ODP (surface pressure = 20 mN/m) into the 0.5mM Mg^{2+} aqueous subphase. (b) The resultant LB film produced following "tail-down" transfer of the Langmuir monolayer substrate, with Mg^{2+} ions bound to the phosphonate headgroups, is shown. (c) The final idealised structure of the Mg-ODP LB monolayer supported upon the OTS-modified Si/SiO$_2$ substrate.

π–A isotherms of ODP-H$_2$ Langmuir films upon a 0.5 mM Mg^{2+} subphase (*ca.* pH 6) were similar in appearance to isotherms produced on a high purity H$_2$O subphase, with a sublimation (gaseous-solid phase) transition observed, Figure 41. The calculated molecular area per ODP molecule upon the Mg^{2+} subphase (27.1 ± 2.5 $Å^2$) shows a small increase in comparison to corresponding Langmuir monolayers prepared upon pure H_2O subphases (24.7 ± 2.5 $Å^2$). This film expansion is attributed to the association of the Mg–O bridges between the Mg^{2+} ions and the oxygen atoms of the phosphonate groups in the resulting metal phosphonate structures. The incorporation of divalent metal ions into LB films of alkylphosphonate is well-established[86,227] with previously reported XPS and FTIR characterisation of multilayered magnesium-phosphonate films showing their structures to be consistent with analogous $M^{II}(O_3PR)\cdot H_2O$ layered solids.[228] The efficiency of film transfer to the substrate surface, evaluated by transfer ratio (TR) calculations, indicates complete monolayer coverage of the substrate (TR = 1.05).

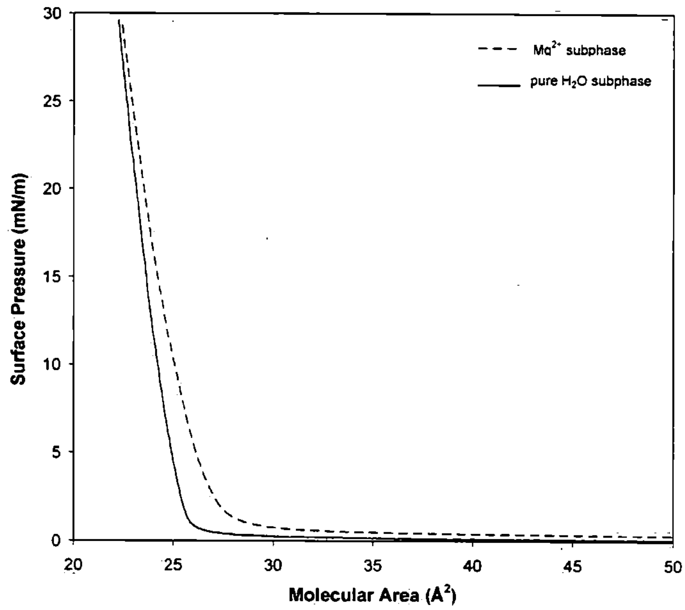

Figure 41. Comparison of π–A isotherms produced during the formation of Langmuir films of ODP-H_2 upon a pure water (solid line) and a 0.5 mM Mg^{2+} (dashed line) aqueous subphase.

AFM analysis shows evidence of characteristic island domains within the LB film structures. Significant defects are observed throughout the film however, with island-island interface defects up to *ca.* 100 nm in diameter present, and "pinholes" prevalent across the film surface, Figure 42. The highly defective nature of the film surface leads to rms roughness values of the surface calculated to be as high as 1.6 ± 0.2 nm over a 5 x 5 μm^2 region.

These defects are believed to introduced into the film structure upon its' removal from the aqueous subphase, with the Mg^{2+} ions providing a lower degree of stabilisation of the ODP surface in comparison to zirconium and hafnium ionic species, as described in Chapter 3. The defects are believed to be the result of peeling of the ODP molecules from the substrate back to the subphase surface upon substrate removal from the subphase, due to unfavourable interactions between the film surface (hydrophilic), and surrounding air environment (considered hydrophobic). Alternatively conformational changes may take place within the film as it is removed from the subphase, with ODP molecules reorientating to "cap" other polar regions of the Mg-ODP surface. Static contact angle values support these suggestions, showing the deposited Mg-ODP LB film surface to be hydrophobic in character (97 ± 3 ^{o}).

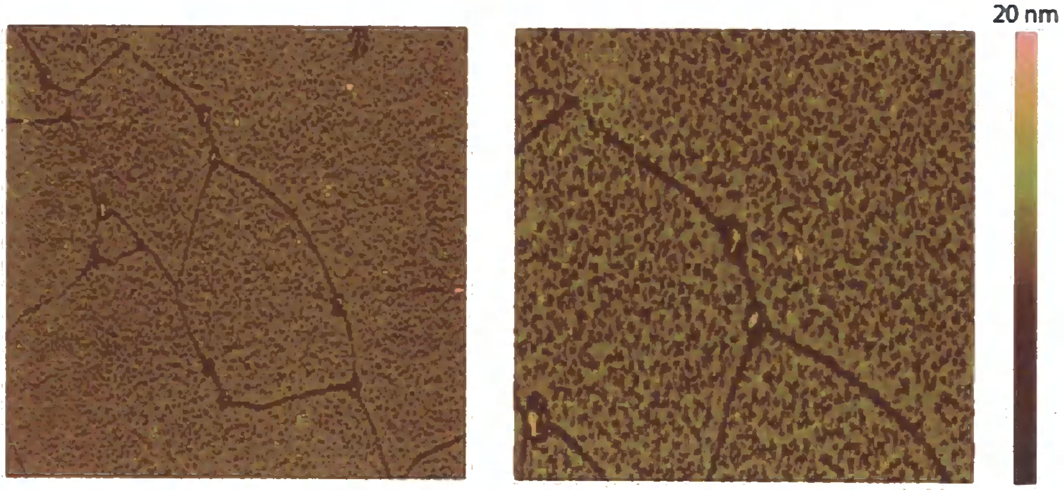

Figure 42. TappingMode™ AFM images showing a 10 x 10 μm^2 (left) and 5 x 5 μm^2 (right) region of a Mg-ODP LB monolayer.

4.2.2 Magnesium-octadecylphosphonate Langmuir-Blodgett bilayers

Efforts to reduce the occurrence of defects in the Mg-ODP films focused upon capping of the polar surface with a second ODP LB monolayer to give a Y-type bilayer structure, Figure 43. Deposition of the capping layer provides a CH_3-terminated film surface which is hydrophobic in character and stable to an air environment.

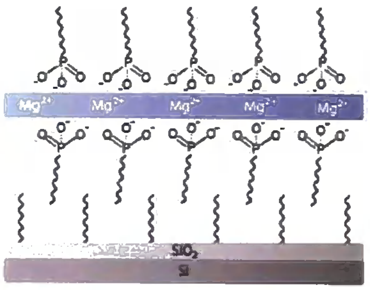

Figure 43. Cartoon representation of the idealised Y-type structure of a Mg-ODP LB bilayer upon an OTS-modified Si/SiO_2 substrate. The magnesium film component is comprised of a simple monolayer of Mg^{2+} ions sandwiched between the headgroups of the ODP monolayers.

Efficient "head-down" deposition of the capping ODP monolayer is shown to take place from transfer ratio calculations (TR = 0.97), indicating almost complete coverage of the substrate surface by the deposited film. Successful formation of the bilayer structure is further evidenced by ellipsometry measurements from which a film thickness of 5.2 ± 0.3 nm was calculated. A calculated theoretical bilayer thickness of *ca.* 5.0 nm (based upon the length of ODP-H_2 molecule[20]) suggests no significant contribution to the film thickness arises from the layer of Mg^{2+} ions sandwiched between the ODP layers. This thickness value is in good agreement with the proposed model of the film structure in which the metal layer consists of a simple monolayer of Mg^{2+} ions, Figure 43.

Chemical characterisation of the bilayers using XPS confirms the presence of magnesium (Mg $2p_{1/2}$, 50.9 eV, $2s_{1/2}$, 89.8 eV), carbon (C 1s, 285.0 eV), oxygen (O 1s, 532.2 eV), phosphorus (P $2s_{3/2}$, 194.6 eV) in the film structure. Calculation of the Mg to P ratio yields a lower value (*ca.* 1 : 2) than that predicted by analogous solid-state $Mg(O_3PR){\cdot}H_2O$ compounds (where the Mg to P ratio = 1 : 1).[229] This may be attributed to incomplete formation of metal phosphonate salts at the monolayer headgroups whilst upon the subphase surface, resulting in decreased levels Mg^{2+} ions being incorporated into the LB film structure.

4.2.2.1 Magnesium-octadecylphosphonate Langmuir-Blodgett multilayers

To provide comprehensive characterisation of the Mg-ODP film structure, analysis of multilayer (seven repeat bilayers) Mg-ODP films prepared by repeated LB depositions was carried out. Ellipsometry data obtained during construction of the multilayer Mg-ODP film (consisting of seven repeat bilayers) confirmed successful multilayer deposition with a linear increase in the calculated film thickness observed. The average bilayer thickness (5.0 nm) determined from a linear fit of the calculated film thickness values (Figure 44) also proved consistent with the Mg-ODP bilayer film thickness values (5.2 ± 0.3 nm) as previously discussed, see Section 4.2.2.

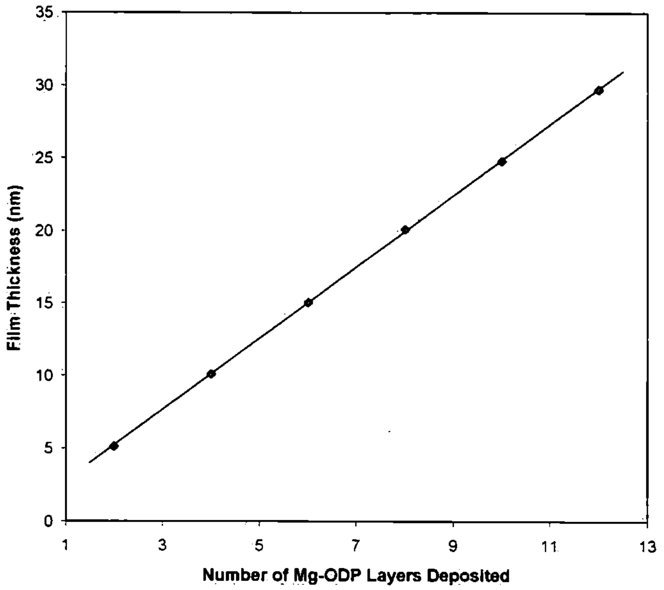

Figure 44. Film thicknesses determined from ellipsometry data, recorded following each Y-type deposition of a Mg-ODP LB bilayer, during the production of multilayer Mg-ODP film.

Further probing of the multilayer films by XRR provided a distinctive diffraction pattern with five clearly distinguishable Bragg peaks assigned to as the 001 ($q = 0.125$ Å^{-1}), 002 ($q = 0.256$ Å^{-1}), 003 ($q = 0.380$ Å^{-1}), 004 ($q = 0.511$ Å^{-1}), and 005 ($q = 0.636$ Å^{-1}) reflections respectively, Figure 45. The q-spacing between the Bragg peaks reveals a mean d-spacing within the bilayers of 4.92 ± 0.1 nm. These data are again in close agreement with ellipsometry data of both the bilayer (5.2 ± 0.3 nm) and multilayer (5.0 nm) Mg-ODP films. Intensity oscillations in the reflected X-ray beam, as observed between the Bragg peaks, arise from interference between the beams reflected from the air-film, and film-substrate interfaces respectively. The number of these interference, or "Kiessig" fringes between each Bragg peak provides a direct indication that the film structure is comprised of seven repeat bilayers (the number of constituent film bilayers corresponds to "N – 2" fringes between two Bragg peaks, where N = number of bilayers).[230]

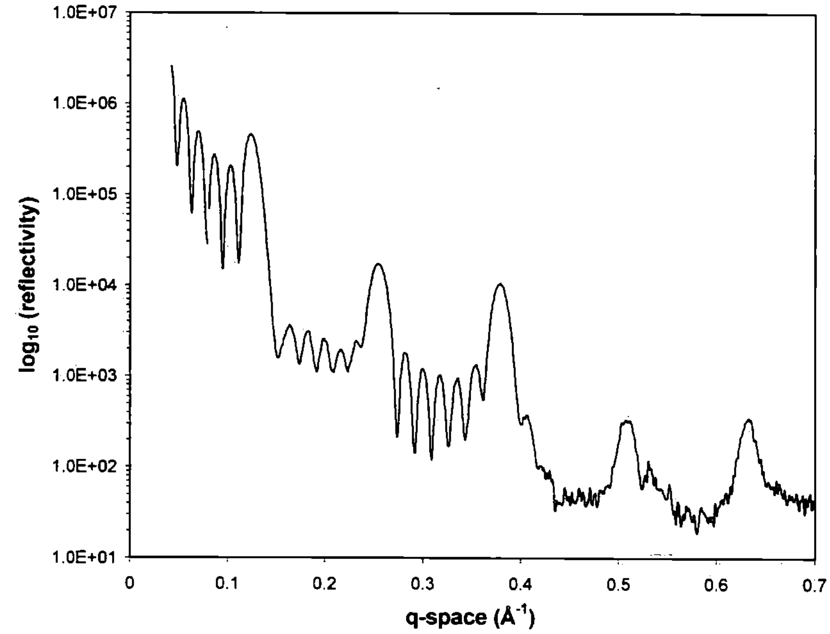

Figure 45. XRR data obtained from a Y-type multilayer LB film, consisting of seven repeat Mg-ODP bilayers, showing five Bragg peaks at q-space values of 0.125 $Å^{-1}$, 0.256 $Å^{-1}$, 0.380 $Å^{-1}$, 0.511 $Å^{-1}$ and 0.636 $Å^{-1}$. Up to five Kiessig fringes are shown between each of the first three Bragg peaks.

Specular reflectance FTIR provided detail of the ordering within the ODP LB monolayers, confirming the alkyl chains to be in a close packed, crystalline state, as confirmed by the position (2918 cm^{-1}) and fwhm (16 cm^{-1}) of the asymmetric CH_2 stretch,[123,216] see Appendix 2.

4.2.2 *Magnesium-octadecylphosphonate Langmuir-Blodgett bilayers*

Having evaluated both the bilayer and multilayer film thicknesses to help elucidate the Mg-ODP bilayer structure, AFM studies of the singly deposited Mg-ODP bilayers were carried out to assess the quality of the films. A significant enhancement in the bilayer film quality over the corresponding LB monolayers (see Section 4.2.1) was revealed by AFM images, showing a highly uniform surface (rms roughness of 0.3 ± 0.1 nm over 5 x 5 μm^2 regions) containing few pinhole defects, Figure 46 (red arrows). Evidence for the bilayer structure being comprised of island domains of ODP-Mg-ODP condensed together is apparent from AFM images, with defects arising between the island-island interfaces (Figure 46, blue arrows) proving less frequent and of smaller line widths (< 50 nm) than those observed in the related Mg-ODP monolayer films (where line widths of defects between island structures were *ca.* 60 - 110 nm, see Section 4.2.1). The defects that are observed between the island structures in the bilayer films show a tendency to extend into the upper bilayer leaflet only (*i.e.* the "capping" ODP monolayer), with a typical depth of 1.9 ± 0.2 nm, Figure 47. Such defects are thought to be a result of the Mg^{2+} binding to the phosphonate headgroups of the monolayer leading to a moderate increase in the film rigidity upon the Mg^{2+} subphase. This is expected to make efficient packing of the island domains of Mg-ODP within the Langmuir monolayer, into a continuous film more difficult. The cross section profile of the defects, as shown in Figure 47, indicates no degradation of the lower bilayer leaflet (*i.e.* the first ODP monolayer depositied upon the substrate) occurs upon withdrawal of the substrate from the subphase. This suggests that, whereas over large surface areas the Mg-ODP monolayers prove unstable to an air environment (see Section 4.2.1), in the smaller, localised regions, such as where the underlying Mg-ODP monolayer is exposed at the island-island interfaces, the film can maintain its structural integrity without degrading upon exposure to air.

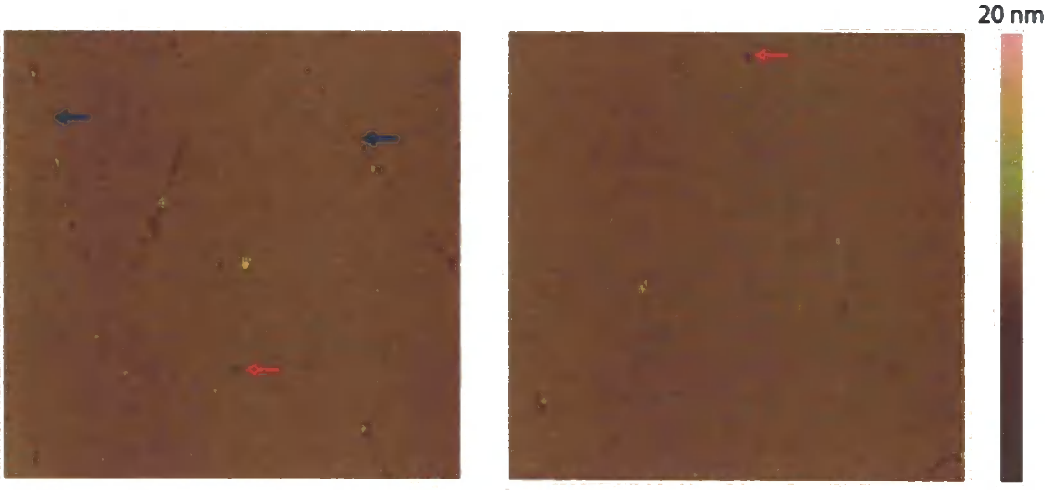

Figure 46. TappingMode™ AFM images both of 6 x 6 μm^2 regions of a Y-type Mg-ODP bilayer. The blue and red arrows highlight the island-island interface defects and pinholes present in the film structure, respectively.

More pronounced defects which span across the entire bilayer thickness are commonly observed at junctions (Figure 47, green arrows) where two or more island-island interface defects adjoin one another (4.9 ± 0.2 nm). Whereas the underlying ODP-Mg leaflet was observed to remain unaffected within the defects between the island interfaces as just discussed, the larger surface areas of the lower bilayer leaflet exposed in these junction regions is thought to result in their degradation upon withdrawal from the subphase.

Static contact angle values (104 ± 2 °) from the bilayer film surface provided confirmation of the hydrophobic character of the film, resulting from its' CH_3-terminated surface.

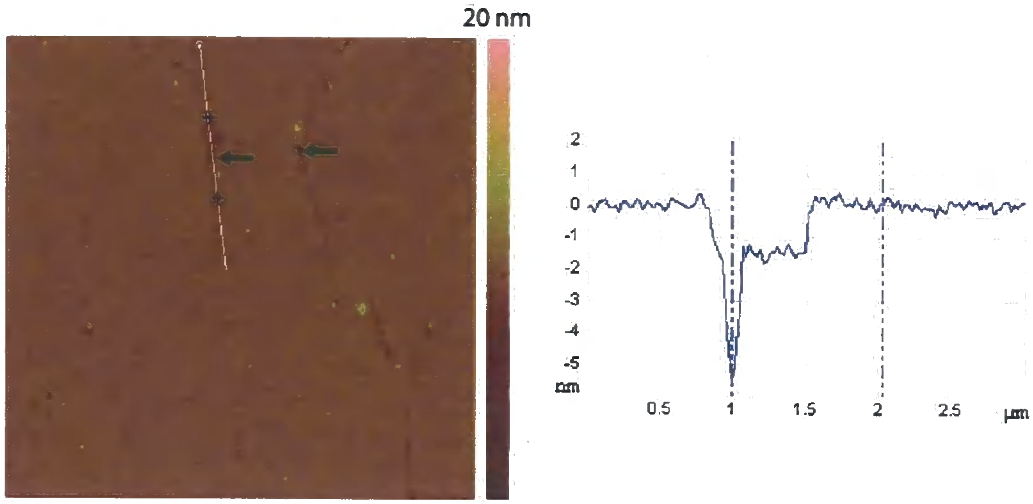

Figure 47. TappingMode™ AFM image of 6 x 6 µm^2 region (left) of a Y-type Mg-ODP bilayer, and a cross section (right) illustrating of the depth of defects present. The green arrows highlight the junction defects in the film structure.

4.2.2.1 Magnesium oxide film formation

In principle, the Mg-ODP bilayer films provide a potential route to the formation of MgO, through high temperature calcination. However, the presence of the magnesium film component as a simple monolayer of Mg^{2+} ions is expected to lead to formation of a significantly thinner film than the corresponding metal oxide films derived from polymeric zirconium and hafnium species (see Chapter 3).

XPS characterisation of the thermally treated (500 °C) bilayer confirmed the presence of magnesium (Mg $2p_{1/2}$, 50.9 eV, Mg $2s_{1/2}$, 89.8 eV), coupled with loss of the phosphorus signal (P $2s_{1/2}$, 191.6 eV), indicating successful decomposition of the ODP film components. Conclusive formation of the metal oxide cannot be confirmed however, with the Mg signals showing some variation in the binding energies typically reported for bulk MgO (Mg 2p, 51.8 eV, Mg 2s, 88.1 eV).[231,232]

XRD data was obtained from $Mg(NO_3)_2{\cdot}6H_2O$ at variable temperatures to attempt to provide evidence that thermal treatment of the bilayer films results in MgO formation upon the sample surface, Figure 48. The diffraction patterns show the phase of the $Mg(NO_3)_2{\cdot}6H_2O$ in the first scan (above 50 °C) to be monoclinic, with dehydration and formation of a cubic $Mg(NO_3)_2$ phase upon reaching temperatures up to 130 °C, with an additional unidentified phase also present. The single peak observed in the final high temperature phase (42.5 °) above *ca.* 290 °C, is consistent with the strongest predicted peak (the (002) reflection) in a fine powder pattern of MgO which occurs at *ca.* 42.8 °.[233] However, the lack of further peaks in the diffraction pattern prevents conclusive identification of the MgO formation. It is possible that a lack of other peaks from this final phase is due to a preferred orientation being adopted with all the crystals aligning in a single direction.

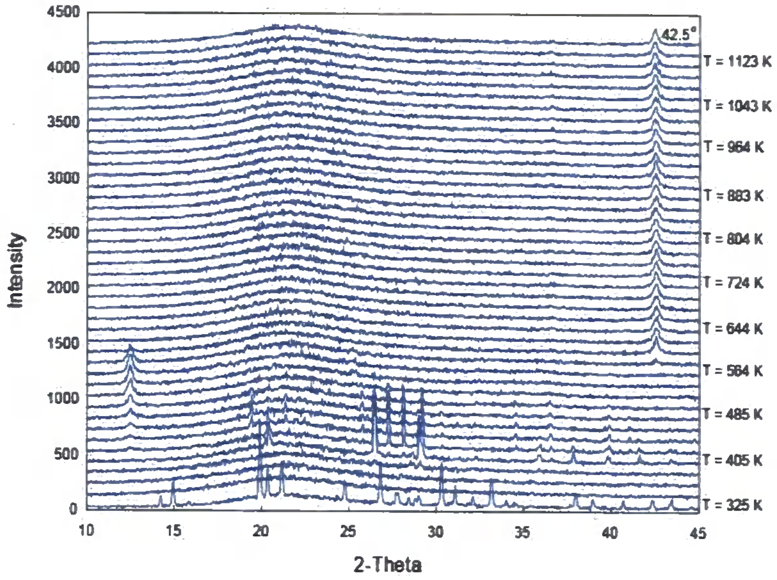

Figure 48. XRD pattern of $Mg(NO_3)_2{\cdot}6H_2O$ at variable temperature ranging from T = 325 - 1163 K, with the final phase above *ca.* 290 °C showing a single peak at 42.5 °.

AFM analysis of the thermally treated sample reveals the characteristic island morphology observed in the initial Mg-ODP bilayer to be no longer evident. Instead, the surface is shown to consist of sparsely dispersed island structures (red arrow, Figure 49) ranging from a few to several hundred square nanometres in size, and protruding 1.0 ± 0.2 nm from the substrate surface. Alongside these discrete island features, larger particulates (blue arrow, Figure 49), up to *ca.* 40 nm in height are observed throughout. The identity of these particulates is unclear, although they are thought to arise from organic contamination of the surface or be a result of the thermal treatment, perhaps being large aggregates of MgO.

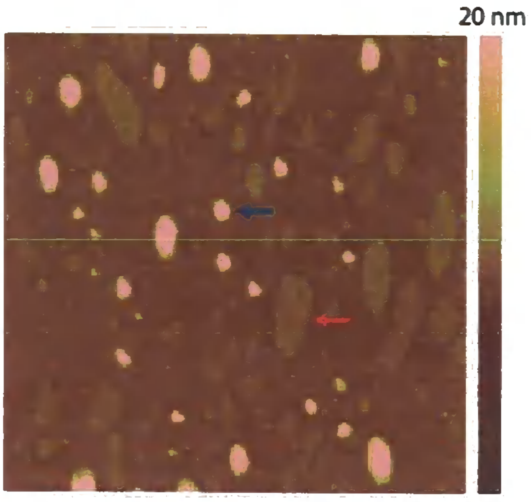

Figure 49. TappingMode™ AFM image (left) of 6 x 6 μm^2 region of a MgO surface, produced following thermal treatment (500 °C) of Y-type Mg-ODP bilayer, supported upon an OTS-modified Si/SiO$_2$ substrate. The red and blue arrows highlight islands of MgO and particulates (possibly of organic contamination or MgO) upon the Si/SiO$_2$ substrate surface.

These changes in the observed surface morphology upon thermal treatment are hypothesised to arise from the inorganic monolayer of Mg^{2+} ions breaking up, with the films coalescing into islands or droplets. This behaviour of the Mg-ODP films is consistent with that observed upon thermal treatment of metal carboxylate LB films of Pb^{2+}, Ba^{2+}, Zn^{2+} and Cd^{2+}.[234,235] Static contact angle values show the surface to be hydrophilic (25 ± 3 °), due to the thermal treatment resulting in exposure of the underlying Si/SiO_2 substrate surface (the islands of MgO are also expected to be hydrophilic in character, bearing hydroxyl groups at their surface).

4.3 *Sol-gel derived magnesium oxide films*

4.3.1 *Sol-gel chemistry*

Sol-gels can be described as rigid, inorganic networks of interconnected colloidal particles formed by hydrolysis and polycondensation of an organometallic precursor.[236,237] The most extensive studies involving of sol-gel formation have used alkoxysilanes such as tetramethoxysilane (TMOS)[238] and tetraethoxysilane[239] (TEOS) due to their labile nature in aqueous solution. A variety of metal alkoxide such as aluminates,[240] and titanates[241] have also been successfully employed as sol-gel precursors.

Control over the physical structure of the final product can be achieved from the manner in the sol-gel is processed, (*e.g.* dip[242] and spin-coating[243] for thin film formation), mold casting[244] (*e.g.* monolithic ceramics of desired shapes), and the synthesis of powders[245] (*e.g.* micro and nanoparticles). The reaction mechanism of sol-gel formation is initiated by hydrolysis of the metal alkoxide, Equation 16.

$$M(OR)n + H_2O \rightarrow M(OH)(OR)_{n-1} + ROH \qquad (16)$$

The hydrated metal products subsequently interact, undergoing condensation reactions to form M–O–M bonds, Equation 17.

$$M(OH)(OR)_{n\text{-}1} + M(OH)(OR)_{n\text{-}1} \rightarrow (RO)_{n\text{-}1}M\text{–}O\text{–}M(OR)_{n\text{-}1} + H_2O \quad (17)$$

Further condensation reactions between the remaining M–OH linkages and further $M(OH)_4$ structures leads to the formation of a polymeric MO_2 framework, Equation 18. The alcohols and H_2O expelled during the reaction remain in the pores of the MO_2 network.

$$(RO)M\text{–}O\text{–}M(OR)_{n\text{-}1} + 2(n\text{-}1)\,M(OH)n \rightarrow$$

$$[(OH)_{n\text{-}1}MO]_{n\text{-}1}M\text{–}O\text{–}M\text{–}M[OM(OH)_{n\text{-}1}]_{n\text{-}1} + 2n(n\text{-}1)\,H_2O \quad (18)$$

As more M–O–M linkages form by hydrolysis and condensation, the polymeric structures begin to act cooperatively as colloidal particles within the solution, forming a "sol". Over time, gelation of the sol occurs as the colloidal particles and oxo-metal species link together, forming the three-dimensional framework of the sol-gel. The nature of subsequent processing of the sol-gel (*e.g.* aging, drying, dehydration and densification) can all be used to control the physical properties of the final structure, and are comprehensively discussed by Hench and West.[246]

Sol-gel synthesis of magnesia (MgO), commonly used as a catalyst for decomposition of propanol, has been reported as an alternative to traditional methods (thermal decomposition of mineral salts), yielding homogeneous, high purity materials.[247] This method uses magnesium ethoxide as the sol-gel precursor due to its reactive nature with H_2O, readily hydrolysing, Equation 19, and undergoing almost simultaneous polymerisation, Equations 20 and 21.

$$Mg(OEt)_2 + H_2O \rightarrow Mg(OH)(OEt) + EtOH \quad (19)$$

$$\equiv Mg-OH \quad + \quad -Mg-OH \quad \rightarrow \quad -Mg-O-Mg- \quad + \quad H_2O \qquad (20)$$

$$Mg(OEt) \quad + \quad -Mg-OH \quad \rightarrow \quad -Mg-O-Mg- \quad + \quad EtOH \qquad (21)$$

Sol-gel formation is sensitive to the presence of acid and base, with changes in pH influencing the chemical structure of the final product.[247] Preparation under basic conditions for example, promotes condensation reactions leading to increased gelation rates. At lower pH values however, the sol-gel process is dominated by hydrolysis reactions, leading to slower gelation, and a highly hydroxylated product. Subsequent heating of the sol-gels leads to the onset of dehydroxylation, giving the final MgO product.

4.3.2 Magnesia-octadecylphosphonate Langmuir-Blodgett monolayer formation upon an aqueous $Mg(OEt)_2$ subphase

Here, magnesium oxide formation using a similar strategy to the fabrication of nanometre-thick zirconium and hafnium oxide films (see Chapter 3), focussed upon exploiting the sol-gel chemistry associated with magnesium alkoxides. The growth of magnesia films directly upon Langmuir monolayers of ODP-H_2 was investigated, using an aqueous $Mg(OEt)_2$ subphase. The saturated solutions of $Mg(OEt)_2$ were of significantly lower concentration than the 0.5 mM Mg^{2+} solutions previously employed in Mg-ODP film preparation (see Section 4.2) due to the sparingly soluble nature of $Mg(OEt)_2$ in H_2O). The resultant π–A isotherm shows two significant variations from those isotherms of monolayers prepared upon pure H_2O and 0.5 mM subphases, Figure 50. (see Sections 4.2.1 and 3.2.2). Firstly, the onset of the surface pressure increase is observed to occur immediately upon compression of monolayer films when prepared upon $Mg(OEt)_2$ aqueous subphases. The second notable characteristic of the isotherm is the significant reduction in the gradient of the surface pressure relative to monolayer films prepared upon pure H_2O and 0.5 mM Mg^{2+} subphases. The isotherm also shows no distinct gradient changes to define phase transitions within the film structure. The significant changes observed in the isotherm shape (in comparison to monolayers prepared upon pure H_2O and 0.5 mM Mg^{2+} subphases) suggest the sol-gel species in solution to be interacting with the monolayer headgroups.

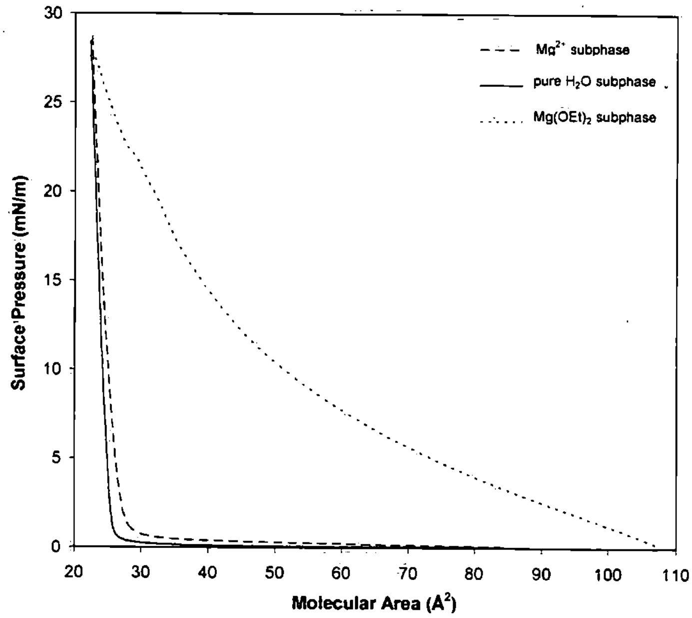

Figure 50. Comparison of π–A isotherms produced during the formation of Langmuir films of ODP upon pure H_2O (solid line), 0.5 mM Mg^{2+} (dashed line), and saturated $Mg(OEt)_2$ (dotted line) subphases.

The morphology of resulting LB film deposited upon an octadecyltrichlorosilane (OTS)-modified Si/SiO_2 substrate at 22 mN/m surface pressure, is revealed by AFM to consist of discrete "island" monolayer domains, Figure 51. The individual island structures exhibit low surface roughness (rms roughness of *ca.* 0.4 nm/island), and are absent of pinhole defects. However, the long range film order is of significantly lower quality with substantial regions in the film structure where magnesia-ODP/ODP-H_2 molecules are absent (between the island domains). This defective film character is believed to arise from binding of magnesia sol-gel structures to the island domains, inhibiting movement of the constituent ODP molecules within the islands. This rigid character associated with the resulting magnesia-crosslinked islands is thought to restrict their packing efficiency. Increases in the surface pressure at which LB films were deposited were found to have minimal effect upon the efficiency with which the island structures pack together, Figure 51.

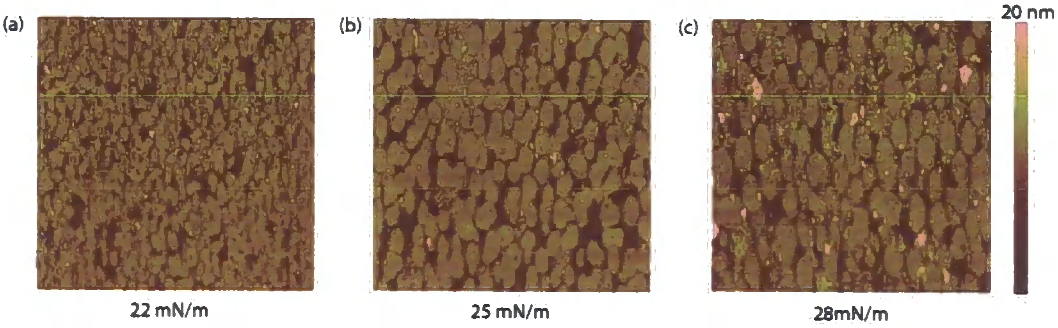

Figure 51. TappingMode^{TM} AFM images of 6 x 6 μm^2 regions of LB monolayer of magnesia-ODP transferred from a $Mg(OEt)_2$ subphase to an OTS-modified Si/SiO_2 substrate at (a) 22 mN/m, (b) 25 mN/m and (c) 28 mN/m surface pressures.

The distinctive island structures associated with the deposited films suggests the ODP monolayer acts as a template which controls morphology of the magnesia structures which associate with the headgroups of the monolayer, Figure 52. The formation of the magnesia layer at the monolayer surface is proposed to take place *via* a "nucleation and growth" process whereby magnesium species which initially bind to the monolayer surface, act as nucleation sites for polycondensation and growth of larger magnesia structures.

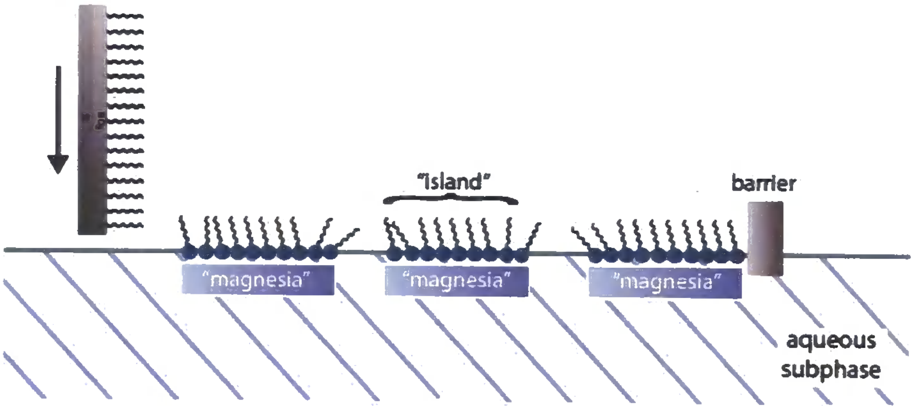

Figure 52. Cartoon representation of formation of magnesia films upon ODP monolayer islands present at the aqueous $Mg(OEt)_2$ subphase surface.

Island heights of 4.5 ± 0.3 nm (determined by AFM) indicate successful formation and binding of polymeric magnesia sol-gel structures to the monolayer domains, contributing up to *ca.* 2.0 nm to the film thickness. The homogeneous and low defect character of the individual island structures suggests that the polymeric magnesia layer provides effective stabilisation of the underlying LB film upon exposure to air.

4.3.2.1 Generation of magnesium oxide films

Further evidence supporting claims of successful magnesia sol-gel growth upon the LB surface is shown from AFM images of the film surfaces following thermal treatment (500 °C) in air, Figure 53. The resulting surface shows a thin film (0.9 ± 0.2 nm) exhibiting the same island morphology of the films prior to the thermal treatment step. The chemical identity of the film is thought to be magnesium oxide, resulting from calcination of the LB-supported magnesia sol-gel. Decomposition of the organic film components during the thermal treatment is again indicated by the observed reduction in the film thickness.

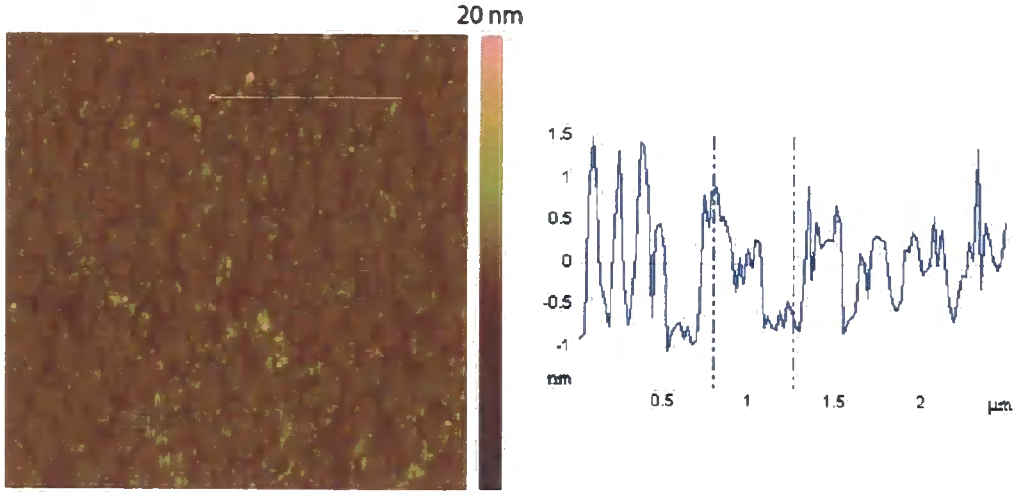

Figure 53. TappingMode™ AFM image (left) of 6 x 6 µm^2 of the proposed MgO film upon a Si/SiO$_2$ substrate produced following thermal treatment (500 °C) of a LB monolayer of magnesia-ODP, and a corresponding cross section (right) of the thermally treated surface.

4.3.3 Magnesia-octadecylphosphonate Langmuir-Blodgett monolayer formation upon a pure H_2O subphase.

As previously discussed, the rigid nature of the magnesia-ODP island domains formed upon an aqueous Mg(OEt)$_2$ subphase is thought to restrict their packing efficiency upon film compression (see Section 4.3.2). This rigid character ultimately results in the formation of discontinuous and highly defective magnesia-ODP LB films. In contrast, Langmuir films prepared upon a pure H_2O subphase have been demonstrated to readily give continuous monolayer films of close packed ODP molecules upon film compression (see Section 3.2.2). This is attributed to the free mobility of the ODP molecules, providing a more malleable character to the island domains formed upon the subphase surface, allowing for their efficient packing through (two-dimensional) reorganisation of their constituent ODP-H_2 molecules during film compression. Following these principles, magnesia-ODP LB films were prepared by a two stage process, involving an initial ODP-H_2 LB deposition from a pure H_2O subphase, proceeded by magnesia film growth upon the LB film surface as a second discrete step. Formation of the magnesia sol-gel films upon the deposited ODP-H_2 film was carried out using buffered (pH10) $Mg(OEt)_2$ aqueous solutions. Basic solution conditions were employed to promote condensation reactions of the magnesium species, and enhance the rate of film growth.[247] AFM analysis revealed a more continuous film structure in comparison to LB monolayers prepared directly upon $Mg(OEt)_2$ subphases, though interface defects between the island domains remained present, along with the interiors of the island structures being populated with pinhole defects, Figure 54.

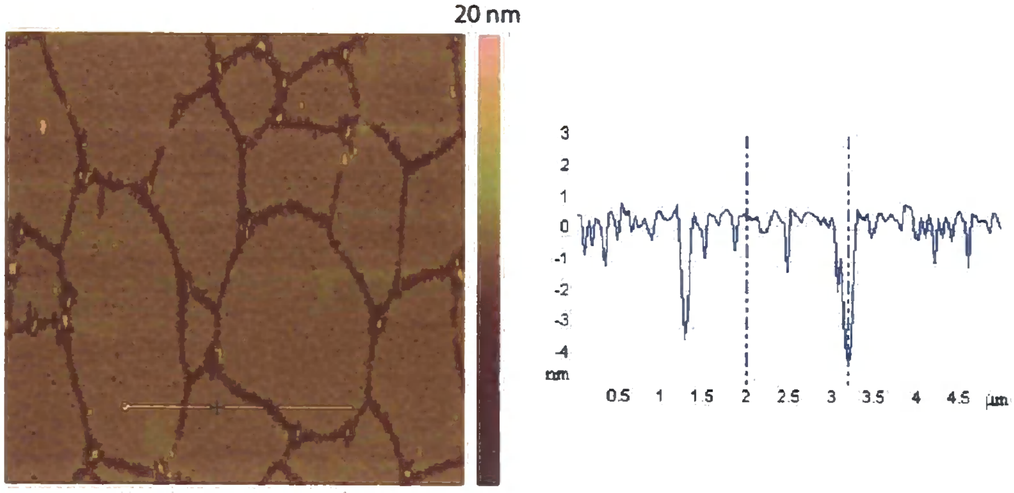

Figure 54. TappingMode™ AFM image of 10 x 10 µm^2 region of a magnesia-ODP film, prepared by LB transfer of an ODP-H_2 monolayer from a pure H_2O subphase to an OTS-modified Si/SiO_2 substrate. Magnesia film growth is achieved is carried out by exposure of the deposited LB film to an aqueous solution of $Mg(OEt)_2$.

The island domains in the LB film structure are significantly larger than those observed in corresponding films deposited from a $Mg(OEt)_2$ subphase, estimated to range from *ca.* one to several square microns in size. The structure of the island-island interface defects are also more consistent throughout the film, forming regular "trenches" (170 ± 50 nm diameter) which encompass the island domains. The presence of such defects is thought to arise from the formation of the initial Langmuir monolayer upon the subphase, as illustrated in Figure 55. It has been previously discussed (see Chapter 3) that the ODP-H_2 monolayers are believed to form upon the subphase surface *via* aggregation of the ODP-H_2 molecules into discrete islands which condense upon compression of the monolayer to form a continuous film structure. In such film structures, it is probable that the surrounding (two-dimensional) environment of the ODP-H_2 molecules at the perimeter of the islands (uneven distribution of neighbouring ODP-H_2 molecules) differs to that of the molecules at the island interior (each molecule fully surrounded by neighbouring ODP-H_2 molecules). The less efficient packing of the perimeter molecules can result in more molecular disorder in these film regions, restricting the availability of the phosphonate headgroups for binding and growth of sol-gel structures. The absence of magnesia species at the island-island interfaces is expected to result in film degradation with loss of ODP-H_2 molecules in these regions upon exposure to air, due to the unfavourable interactions between the exposed monolayer headgroups and surrounding air environment. Though such defects were not observed in Zr-ODP and Hf-ODP monolayer films prepared using a similar methodology, this may be attributed to strong oxophilicity of the tetravalent metal species enabling metal ion binding to the phosphonate headgroups of ODP-H_2 molecules in the island-island interface regions. In comparison, the lower stability of magnesium-phosphonate (suggested by differences in the preparation of Zr-

ODP and Mg-ODP LB films, *i.e.* Zr-ODP films more rigid and unable to be deposited directly from an aqueous Zr^{4+} subphase[86,247]) may result in the magnesia sol-gel binding proving less tolerant to small changes in the orientation of the monolayer molecules, and subsequent availability of the headgroups. Steric considerations relating to ability of the metal species to approach the headgroups of the disordered ODP-H_2 molecules at the island perimeters may also contribute to these differences in binding.

Assuming a complete absence of ODP-H_2 molecules from these regions, defect depths of 4.3 ± 0.3 nm, as revealed by AFM, suggest the presence of a magnesia sol-gel layer bound to the LB film, up to *ca.* 1.8 nm thick. Further evaluation of the AFM data shows the presence of pinhole defects, *ca.* < 80 nm in diameter, within the island domains. These pinholes are less invasive than the interface defects however, penetrating no more than *ca.* 2.4 nm into the film structure, suggesting they only partially extend into the underlying ODP monolayer. Film thickness values (4.0 ± 0.1 nm) of the magnesia-ODP monolayers, determined from ellipsometry data, prove in reasonable agreement with AFM data, indicating a magnesia layer *ca.* 1.4 nm thick.

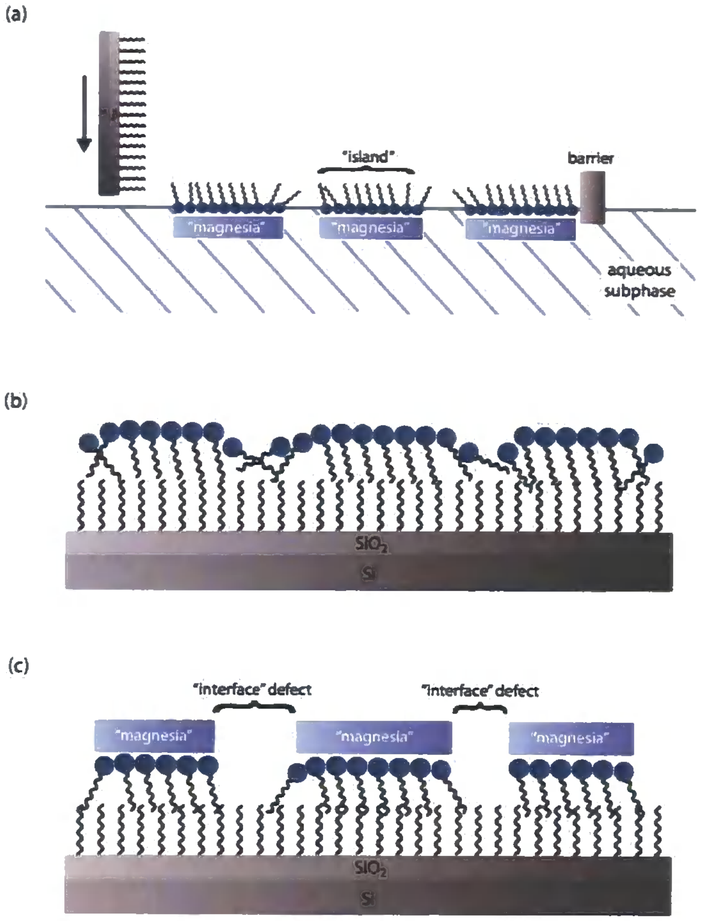

Figure 55. Cartoon representation of origins of island-island interface defects which arise in magnesia-ODP LB films deposited upon OTS-modified Si/SiO$_2$ substrates: (a) Formation of monolayer island domains of ODP-H$_2$ molecules upon subphase surface. (b) Resulting structure of ODP-H$_2$ LB monolayer upon the OTS-modified Si/SiO$_2$ substrate, showing increased molecular disorder island perimeters. (c) Final magnesia-ODP film structure following treatment of LB surface in a saturated Mg(OEt)$_2$ solution.

4.3.3.1 Multilayer magnesia-octadecylphosphonate Langmuir-Blodgett film formation upon a pure H$_2$O subphase.

Further characterisation of the magnesia-ODP film structure was once again carried out upon the corresponding multilayer LB film. Film thickness values were determined from ellipsometry data following each bilayer deposition. Fitting of the ellipsometry data to a linear model yields an average bilayer thickness (5.8 nm) which corresponds to a minimum contribution of *ca.* 0.8 nm from the magnesia layer to the magnesia-ODP film thickness, Figure 56. This magnesia thickness value is expected to be larger in reality, as the multilayer film model to which the film thickness data is fitted to, does not take into account any tilt associated with the alkyl chains of the ODP molecules.

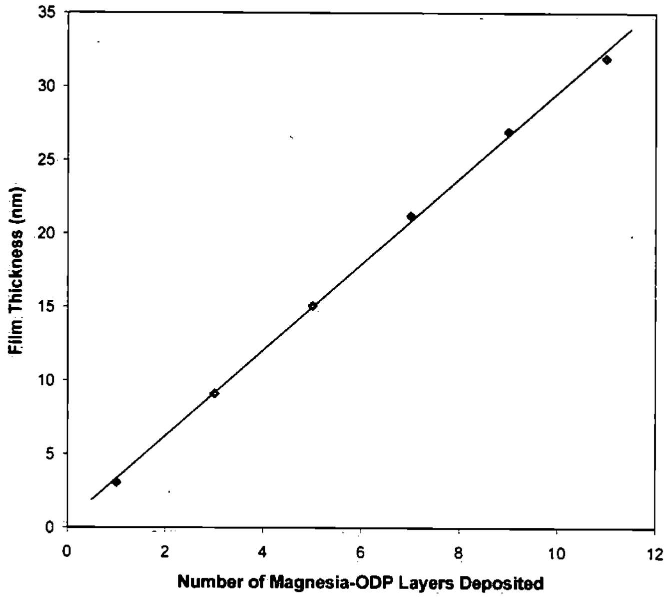

Figure 56. Film thickness determined from ellipsometry data, recorded following each Y-type deposition of a magnesia-ODP LB bilayers, during production of a multilayer film.

Specular reflectance FTIR once again confirms a high degree of conformational order of the alkyl chains within the LB layers as indicated from the asymmetric CH_2 band resolved at 2918 cm^{-1}, with a fwhm value of 12 cm^{-1},[123,216] see Appendix 3.

4.3.3.2 Generation of magnesium oxide films

Thermal treatment (500 °C) of magnesia-ODP LB monolayers was again observed to lead to a reduction in the film thickness (Figure 57), due to loss of organic material from the film structure. High levels of retention of the initial LB film morphology are also observed throughout the resulting MgO film. The metal oxide shows an increased film thickness (1.5 ± 0.2 nm) in comparison to the MgO films produced from LB films prepared upon an aqueous $Mg(OEt)_2$ subphases (0.9 ± 0.2 nm), see Section 4.3.2.1. This may be attributed to the longer periods which the ODP LB films prepared upon a pure H_2O subphase are exposed to the $Mg(OEt)_2$ solution (1 hour) in comparison to LB films prepared directly upon a $Mg(OEt)_2$ subphase (ODP-H_2 molecules remain on aqueous $Mg(OEt)_2$ subphase surface for *ca.* 25 - 30 mins during LB preparation), enabling more substantial growth of the sol-gel film upon the LB surface.

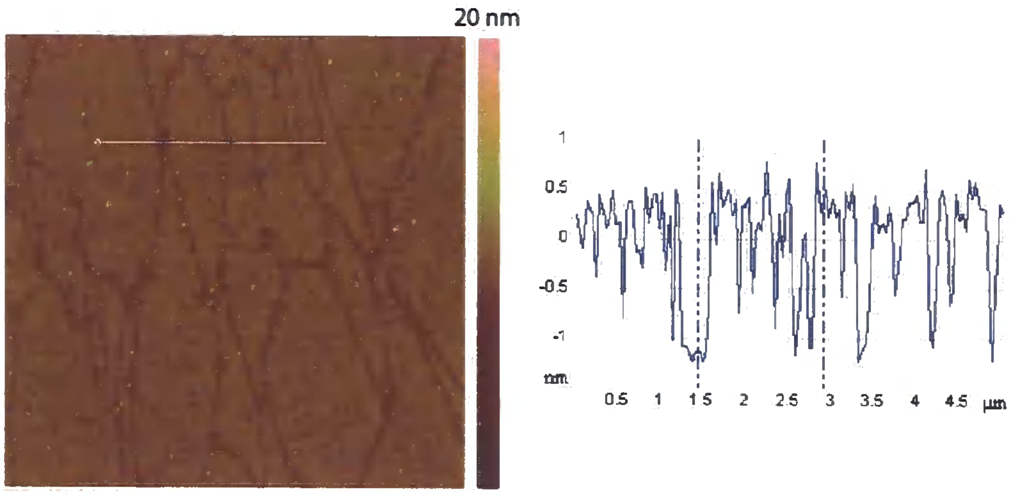

Figure 57. TappingMode™ AFM image (left) of 10 x 10 µm^2 region of proposed MgO film upon a Si/SiO_2 substrate, produced following thermal treatment (500 °C) of a magnesia-ODP LB film deposited upon an OTS-modified Si/SiO_2 substrate from a pure H_2O subphase, followed by magnesia solution assembly, and a corresponding cross section (right) of the film surface.

Attempts to identify the formation and phase of the MgO film proposed to be produced during the thermal treatment step were carried out by variable temperature XRD studies upon the $Mg(OEt)_2$ used in the sol-gel preparation. The resulting XRD pattern showed little evidence of the formation of any crystalline phases, with the sample remaining largely amorphous throughout the temperature range employed. However, there was perhaps weak evidence for the formation of small particles of MgO at high temperature, with a broad peak possiblt present at *ca.* 42 °. This correlates to the strongest predicted peak in a fine powder pattern of MgO, representing the (002) reflection at around $2\theta = 42.8\ ^{\circ}$),[233] Figure 58.

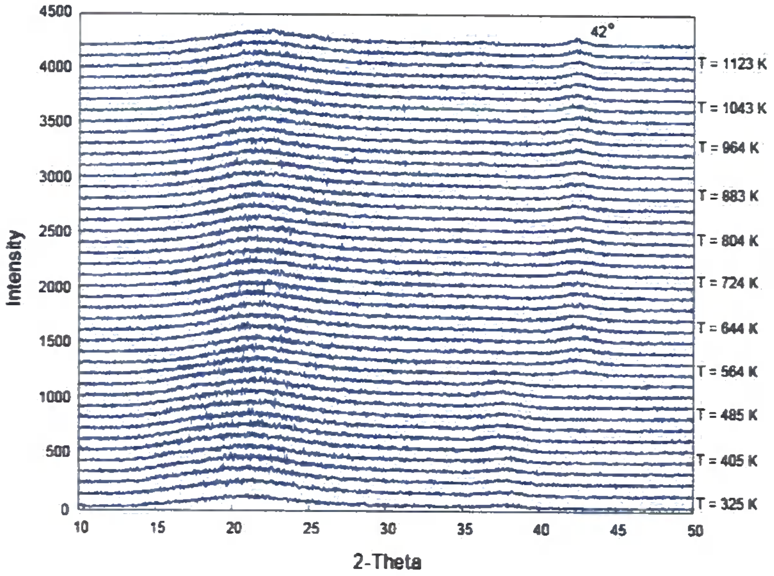

Figure 58. XRD pattern of $Mg(OEt)_2$ at variable temperature ranging from T = 325 - 1163 K, shows the sample to be largely amorphous throughout the temperature range. Some evidence of a broad peak at around 42 ° (possible (002) reflection) may suggest the formation small particles of MgO at high temperatures.

4.3.4 Magnesia-octadecylphosphonate Langmuir-Blodgett monolayer formation upon a Mg^{2+} subphase.

Both the advantages and drawbacks of the use of Mg^{2+} ions and magnesia sol-gels respectively in the generation of MgO films have been highlighted here (see Sections 4.1 and 4.2). Film preparation upon Mg^{2+}-modified subphases has been demonstrated to yield low defect LB bilayers of Mg-ODP for example, but prove unsuitable for the generation of homogeneous metal oxide surfaces due to coalescence of the films upon thermal treatment (500 °C). In contrast, the sol-gel processes undergone by metal alkoxides provide a convenient route to the growth of nanometre-thick magnesia films upon ODP-H_2 LB monolayers, suitable for subsequent formation of metal oxide films. However, such films were prone to numerous and significant defects throughout.

Here, attempts to fabricate magnesium oxide films which exhibit the favourable characteristics of both Mg^{2+} and magnesia-derived metal-ODP LB films have been investigated through incorporation of both Mg^{2+} ions and magnesia sol-gel structures into an ODP-H_2 LB film. Preparation of the initial ODP-H_2 monolayer was carried out upon a 0.5 mM Mg^{2+} subphase to enhance film stabilisation through association of Mg^{2+} ions to the headgroups of the ODP-H_2 molecules. Following transfer of the monolayer to the OTS-modified Si/SiO_2 substrate support, magnesia sol-gel formation was carried out upon the LB surface.

AFM analysis of the resulting magnesia/Mg-ODP monolayers shows significant variations in film quality across the surface. Highly uniform film regions, free of pinholes and showing efficient packing of the island domains can be observed across a typical magnesia/Mg-ODP film for example, Figure 59a. Despite the efficient packing of the monolayer islands observed in high quality regions of the film, defects remain present at the junctions (*ca.* 50 nm in diameter) where two or more of the island-island interfaces adjoin (Figure 59a, green arrows). Cross sectional analysis indicates a depth at these junctions of 4.8 ± 0.3 nm, suggesting the defects extend through both the magnesia film, and underlying ODP LB monolayer. Large particulates, up to *ca.* 20 nm in height, frequently observed to occupy the junction defects are thought to be colloidal particles of non/partially-hydrolyses $Mg(OEt)_2$ species formed in solution. The unhydrolysed ethoxy groups are thought to provide hydrophobic regions to the colloid surface, leading to their preferential adsorption at the junction defect sites where the underlying (hydrophobic) OTS monolayer is exposed. Adsorption of particulates to the magnesia-ODP surface is less favourable due to its more hydrophilic character as confirmed by static contact angle measurements (84 ± 4 °). The efficient packing of the magnesia-ODP island domains leads to only a small amount of disruption to the film structure at the island-island interfaces. Defects observed at these points in the film typically only penetrate a distance of up to 1.6 nm into the film structure, indicating that they do not extend beyond the upper magnesia layer, into the underlying ODP monolayer.

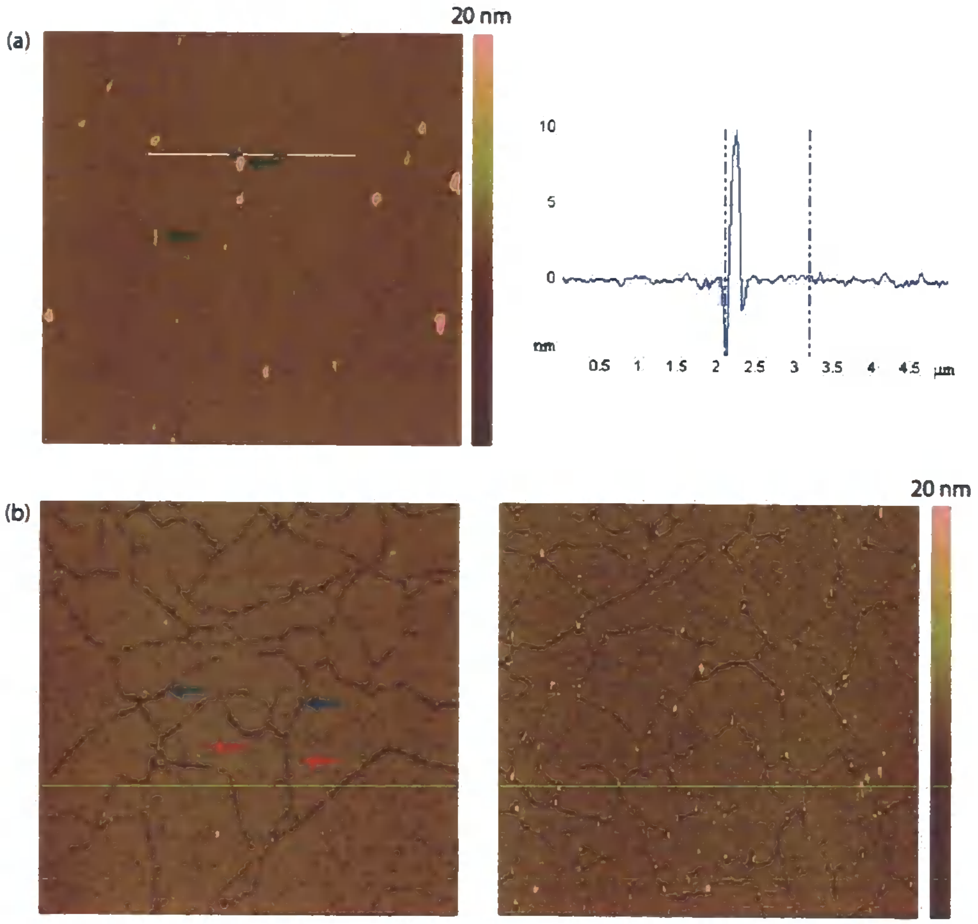

Figure 59. (a) TappingMode™ image (left) of 10 x 10 µm^2 region of magnesia-ODP LB film supported upon an OTS-modified Si/SiO$_2$ substrate, prepared from a 0.5 mM Mg^{2+} subphase, and a cross section (right) of the film highlighting the depth of the junction defects present. Magnesia sol-gel film formation was carried out by subsequent Mg(OEt)$_2$ solution treatment of the deposited LB film. (b) TappingMode™ AFM images of 10 x 10 µm^2 regions of magnesia-ODP LB films, prepared as described in (a), which highlight the variation in film quality from (a) that was often observed across the magnesia-ODP films.

However, as well as these low defect film regions, other areas of lower film quality were also observed across the magnesia-ODP film structure, which were more susceptible to pinhole defects (Figure 59b, red arrows) and exhibited less efficient packing of the island domains (Figure 59b, blue arrows). These lower quality film regions showed more extensive defects present at the island-island interfaces, both in terms of their diameter (up to *ca.* 70 nm) and depth (5.1 ± 0.2 nm). Pinholes in these regions, typically ranging from 60 - 150 nm in diameter, varied in their density across the surface (Figure 59b), and typically extended 4.0 ± 0.3 nm into the film structure. Ellipsometry data recorded upon singly deposited magnesia-ODP monolayers showed good agreement with the AFM data, indicating a film thickness of 4.9 ± 0.3 nm. Measurements recorded across a multilayer magnesia-ODP LB film proved less consistent however, with an average bilayer of 5.2 nm suggesting minimal contribution to film thickness arising from the magnesia bilayer components, (assuming a standard ODP-H_2 bilayer thickness of *ca.* 5.0 nm based upon the theoretical length of an ODP-H_2 molecule[20]), Figure 60.

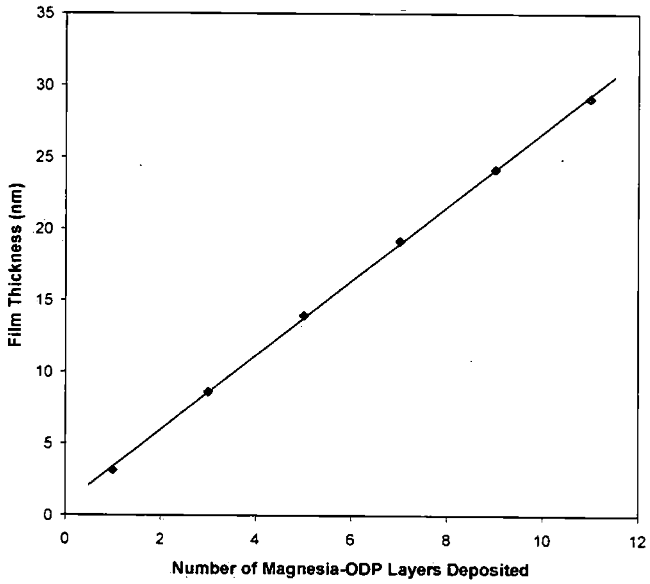

Figure 60. Ellipsometry data recorded of the total film thickness following each Y-type deposition of magnesia/Mg-ODP LB bilayers, deposited from a 0.5 mM Mg^{2+} subphase, in the step-wise production of a multilayer film. The linear fit of the film thickness increase following sequential bilayer depositions reveals an average bilayer thickness of 5.2 nm.

The XRR data of the multilayer film shows two Bragg peaks at q = 0.117 $Å^{-1}$ and q = 0.239 $Å^{-1}$, representing the (001) and (002) reflections, respectively, Figure 61. The difference in the q-space values ($d = 2\pi/\Delta q$) between the Bragg peaks corresponds to a d-spacing of 5.2 nm, a value in good agreement with the ellipsometry data. As commented upon previously following evaluation of the ellipsometry data, this value for the bilayer thickness appears low for the production of film structures where a nanometre thick magnesia layer is expected to be present. Though it should once again be noted that the multilayer film model to which the ellipsometry and XRR data is fitted, does not take into account any tilt associated with the alkyl chains of the ODP molecules, it is unlikely that this tilt would occur to the extent that would result in a 5.2 nm bilayer structure (as this would require the chains to lie virtually flat relative to the surface normal). As a result, the reasons for these contrasting findings in comparison to the AFM and ellipsometry data of the single layer magnesia-ODP films is yet to be established.

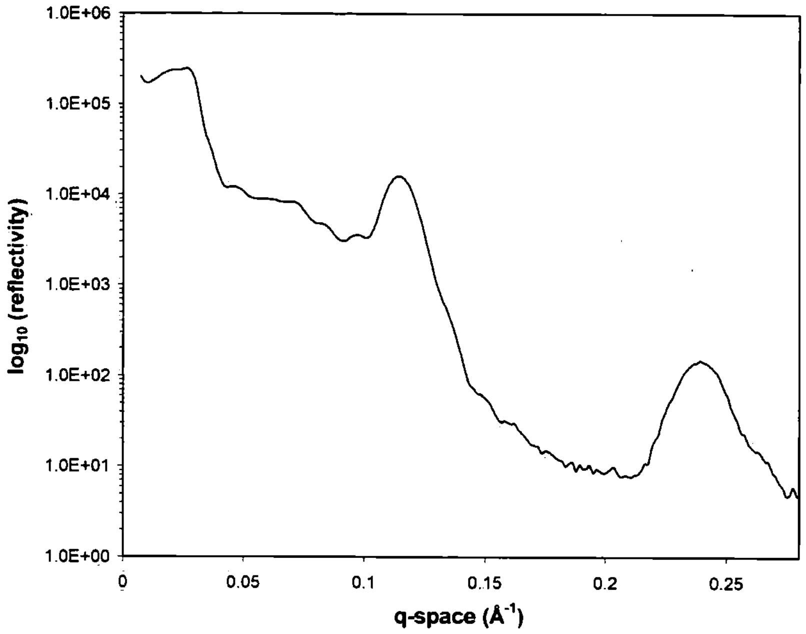

Figure 61. XRR data obtained from a Y-type multilayer magnesia-ODP LB film, consisting of seven repeat bilayers, showing two Bragg peaks at q-space values of 0.117 $Å^{-1}$, and 0.239 $Å^{-1}$.

FTIR data proved consistent previous multilayer films prepared, indicating a close packed, crystalline phase (asymmetric CH_2, 2918 cm^{-1}; fwhm value, 16 cm^{-1}) associated with the aliphatic chains of the ODP molecules, see Appendix 4.

4.3.4.1 Magnesium oxide film formation

Thermal treatment (500 °C) of singly deposited magnesia-ODP LB monolayers yielded results consistent with magnesia films prepared upon a pure H_2O subphase, generating a thin metal oxide film (1.5 ± 0.2 nm), as shown from AFM cross section profiles, Figure 62. Again, the island morphology observed in the initial magnesia/Mg-ODP LB monolayer is preserved in the thermally treated film structure. The hydrophilic character of the thermally treated surface was confirmed by static contact angle measurements, (17 ± 3 °).

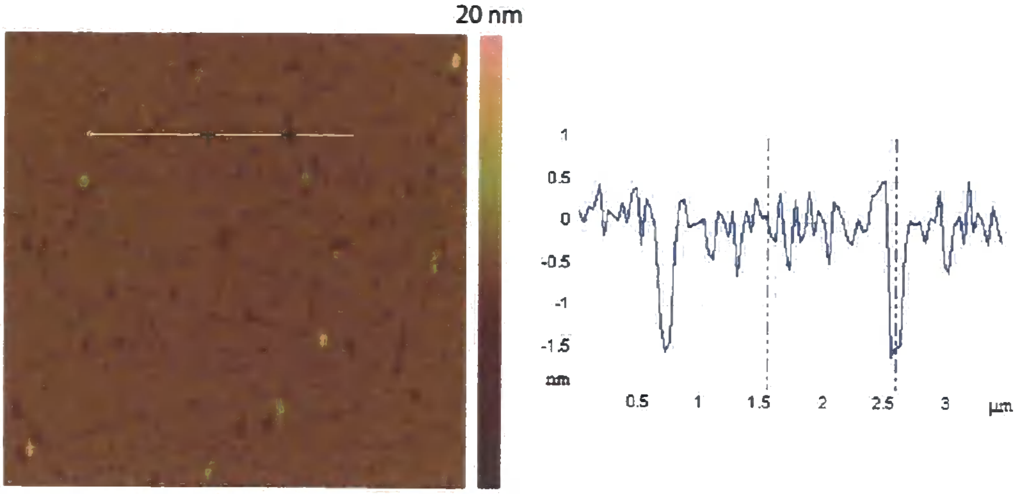

Figure 62. Tapping mode AFM image (left) of 6 x 6 µm^2 region of proposed MgO film upon a Si/SiO$_2$ substrate, produced following thermal treatment (500 °C) of a magnesia-ODP LB monolayer, deposited upon an OTS-modified Si/SiO$_2$ substrate from a 0.5 mM Mg^{2+} subphase, and a corresponding cross section (right) of the film. Magnesia sol-gel film formation was carried out by treatment of the deposited LB film in an aqueous Mg(OEt)$_2$ solution.

4.4 Conclusions

The formation of magnesium oxide films of nanometre-scale thickness has been demonstrated through the growth of a metal oxide precursor film upon an ODP-H$_2$ LB monolayer. The requirement for metal species capable of forming polymeric structures in solution, to grow "precursor" films suitable for subsequent metal oxide fabrication, is highlighted by comparative studies into MgO film formation, employing different magnesium compounds which exhibit contrasting aqueous chemistry. Growth of magnesium precursor films derived from Mg(NO$_3$)$_2$ failed to generate highly quality MgO films, attributed to the magnesium species existing as Mg^{2+} ions in solution, and binding upon the LB film surface as simple monolayer of Mg^{2+} ions. In contrast, successful formation of nanometre-thick films of MgO was achieved by LB-supported growth of precursor films derived from $Mg(OEt)_2$. The success of this strategy was attributed to the tendency of the metal alkoxide to form sol-gels in solution *via* a series of hydrolysis and condensation reactions.

Improvements in the quality of the magnesia-ODP (and hence MgO) films were also achieved by preparation of LB monolayers upon a Mg^{2+} subphase, followed by sol-gel film growth. The resultant films show a considerable reduction in the number of defects present, attributed to association of Mg^{2+} ions to the headgroups of the ODP-H_2 molecules, enhancing the stability of the initial LB monolayer deposited.

Chapter 5

5. *Preparation of nanopatterned "soft" and "hard" ultra-thin films*

5.1 *Introduction*

In recent years the generation of nanopatterned surfaces has attracted considerable attention.[248,249] The ability to engineer chemical structures on such a small scale is of great potential importance to the development of nanoelectronic and optical devices,[1,250] as well as biosensing[251] technologies. Lithographic processes such as electron-beam (e-beam)[252,253] and photolithography[120,254,255] are perhaps two of the most commonly employed techniques used in the fabrication of such technologies.[256] However, other more cost effective lithographic methods such as microcontact printing,[131,257] and nanoimprint lithography[258] continue to be developed, and find commercial use.

Recently, efforts have focussed upon the development of lithographic methods based upon scanning probe technology (AFM, STM and SNOM),[139] which take advantage of the nanometre sized dimensions of the SPM probes and localised probe-surface interactions. Such technologies have been exploited in a variety of different scanning probe lithography (SPL) applications such as dip-pen nanolithography (DPN),[172] catalytic probe AFM-induced surface reactions,[190,259] STM and conductive probe AFM-induced localised surface oxidation,[260,261] and scanning probe photolithography.[192,262] Other examples of interest include nanoshaving and nanografting which rely upon the physical displacement of molecules through the application of high vertical forces upon the substrate surface by an AFM probe.[263]

Chapter 5

Previously reported nanoshaving experiments have focussed upon modification of alkylthiolate monolayers prepared upon Au[168] and long chain alkenes bound to SiH[167] substrates. Using a method similar to that of Liu,[168] the production of patterned metal-octadecylphosphonate (metal-ODP) Langmuir-Blodgett (LB) monolayers (see Chapters 3 and 4) is described. The "soft" nature of the organic film allows for selective shaving, or "nanodisplacement" of the LB monolayer within well-defined surface regions by careful control of the vertical forces exerted by the AFM probe, Scheme 6a.

The patterned LB films are also demonstrated to provide an indirect route to the fabrication of patterned metal oxide films in which a single thermal step is used to decompose the organic film components, whilst also calcining the inorganic metal layer to generate the final metal oxide surface. During this stage the patterned LB film acts as a template with the patterns shaved into the metal-ODP layer maintaining their integrity in the resulting metal oxide film structure, Scheme 6b.

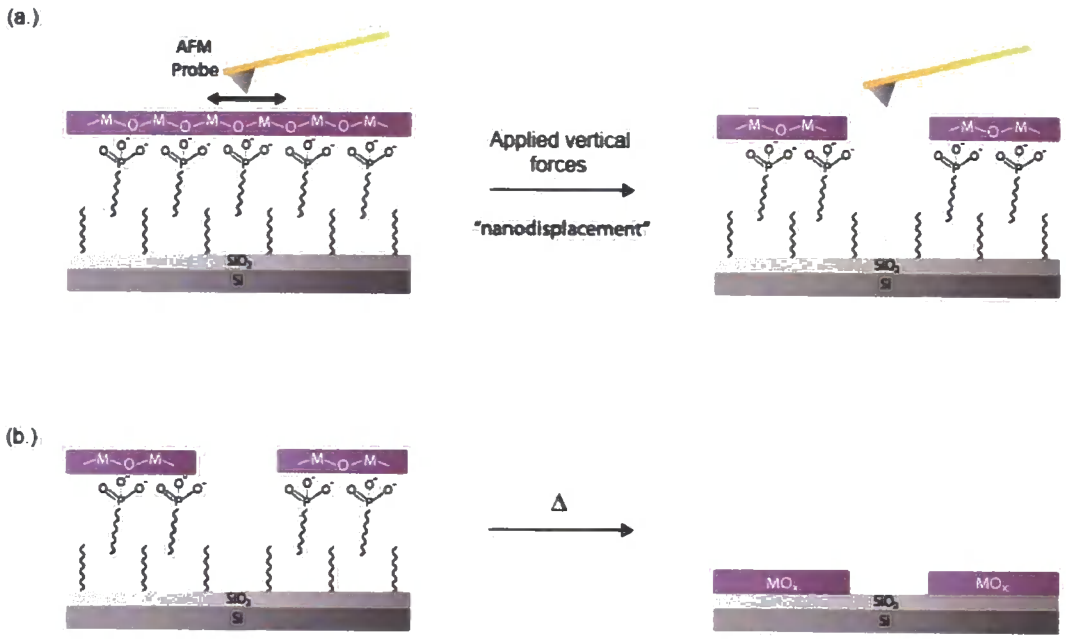

Scheme 6. Cartoon representation of the production of nanopatterned LB and metal oxide films: (a) AFM probe used for spatially controlled application of high vertical forces (> *ca.* 40 nN) upon a metal-ODP LB monolayer (metal = $Zr^{4+}/Hf^{4+}/Mg^{2+}$), supported upon an OTS-modified Si/SiO_2 substrate. The high vertical forces lead to displacement of material from the LB layer. (b) Decomposition of the organic film components and simultaneous calcination of the inorganic metal layer are achieved using a single thermal step (typically 500 °C). The shaved patterns in the LB film transfer into the resulting metal oxide film.

5.2 *Nanopatterning of metal-octadecylphosphonate Langmuir-Blodgett films*

AFM nanodisplacement patterning of the metal-ODP monolayers, supported upon an OTS-modified Si/SiO_2 substrate, was carried out by contact mode AFM operation. AFM probes were used during the nanodisplacement process with a cantilever spring constant (k) of 0.32 N/m or 0.58 N/m and a Si_3N_4 tip. The robust nature of the Si_3N_4 helps reduce degrading and blunting of the tip which can take place as a result of the high vertical forces generated as the tip contacts the film surface during the nanodisplacement process. Blunting of the AFM probe tip will lead to reductions in the patterning and imaging resolutions offered by the probe, as well as influence the pressures generated upon the film surface (due to the increased surface area of the tip point).

Regulation of the vertical forces applied by the AFM probe upon the film surface is of great importance in order to control when nanodisplacement of the film material takes place, and prevent subsequent film damage during imaging of the patterned surface. Calculation of the vertical forces exerted upon the LB film were determined from force curves generated through measurement of the tip cantilever deflection, as a function of the z-position of the AFM probe as the tip is brought into contact and then detached from the film surface (see Section 2.2.1.1). Calculation of the vertical forces was subsequently carried out in accordance with Hookes Law ($F = - k \cdot x$), using the cantilever displacement (*i.e.* deflection) determined from the force curve, and the cantilever spring constant (as supplied by the probe manufacturer).

5.2.1 Zirconium-octadecylphosphonate

Nanodisplacement of zirconium-octadecylphosphonate (Zr-ODP) LB monolayers (see Section 3.2 for film preparation and characterisation) was used to pattern shaved features into the LB film, which reveal the underlying octadecyltrichlorosilane (OTS)-modified Si/SiO_2 substrate. From force-curve measurements, a minimum vertical force threshold of *ca.* 40 nN was determined to be required for consistent and complete displacement of the LB layer molecules. Scan rates of 10 - 12 Hz were typically employed during the nanodisplacement process with complete shaving of the desired region achieved rapidly (typically < 1 minute). Repeated scanning of the film surface in contact mode, with forces optimised for imaging (*i.e.* vertical forces experienced upon surface minimised typically to < 5 nN), showed no immediate damage to the film.

A typical pattern produced is shown in Figure 63, comprising of a series of parallel lines with a 500 nm line width, patterned at 45 ° to the imaging scan angle, Figure 63. A cross section profile of the patterned surface (Figure 63a) shows the shaved features to be 4.6 ± 0.4 nm in depth, consistent with the removal of the ODP layer (*ca.* 2.5 nm[20]) and a polymeric Zr^{4+} film of *ca.* 2.1 nm. Increasing the nanodisplacement process to longer time periods, and varying the applied forces (above the threshold value) were found to have no effect upon the depth of the shaved features. The close agreement between the pattern depths and the defects (4.6 ± 0.2 nm) observed in Zr-ODP LB films deposited at reduced surface pressures (10 mN/m, see Section 3.2.2) indicates the underlying OTS SAM remains intact following the nanodisplacement process. Further supporting evidence for the resistance of the OTS to nanodisplacement was shown in separate AFM nanodisplacement studies where attempts to etch Si/SiO_2-supported OTS monolayers (without a metal-ODP monolayer deposited on top) using forces up to *ca.* 240 nN failed to disrupt the SAM surface. Similar findings have previously been reported by Wang *et al.*[23] who demonstrated that applied forces of up to 1 μN were unable to disrupt Si/SiO_2-supported OTS films. The high stability of the OTS monolayer is attributed to the high degree of crosslinking which takes place through the formation of Si–O–Si linkages between the OTS headgroups.[56]

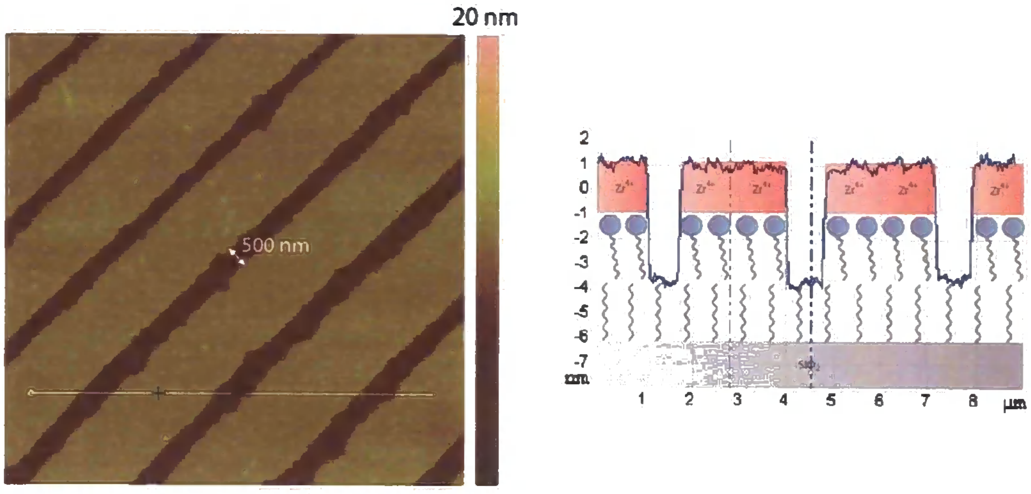

Figure 63. Contact mode AFM image (left) of 10 x 10 μm^2 region of a patterned Zr-ODP LB film, showing trenches (dark brown) of 500 nm line width shaved into LB layer (yellow), and a corresponding cross section profile of the patterned surface (right) shows the depth of the shaved features and a cartoon representation of the proposed film structure.

The clean nature of the surfaces typically observed following patterning, with little evidence of the displaced film material being observed upon the LB film surface, suggests that this material transfers to the AFM probe rather than redepositing upon the film surface. AFM was also used to identify compositional changes across the patterned film by monitoring the frictional characteristics of the surface *via* the interactions between the probe tip and sample surface (see Section 2.2.1.2). Topographical contributions to the friction force data were removed through subtraction of the retrace AFM friction image from the trace image. The friction force image shown in Figure 64, (which corresponds to the AFM image of the patterned Zr-ODP LB film in Figure 63) demonstrates clear contrast between the shaved regions and the surrounding undisrupted Zr-ODP LB monolayer. These changes in frictional character across the surface are attributed to the differences in chemical composition between the shaved film regions (where the underlying CH_3-terminated OTS SAM surface (hydrophobic) is exposed) and the surrounding Zr-terminated LB film surface (hydrophilic).

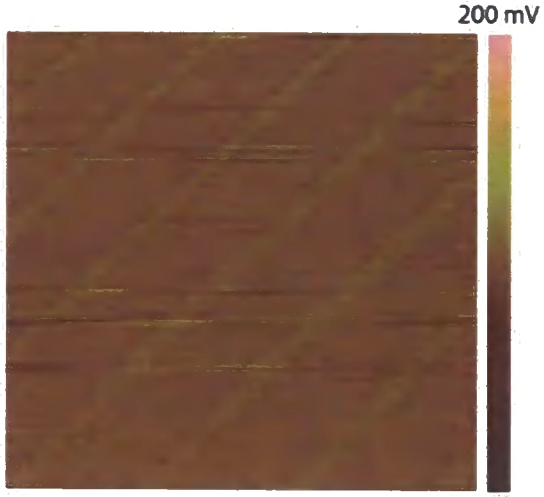

Figure 64. Friction AFM image of a patterned Zr-ODP LB film, highlighting differences in the frictional characteristics of the Zr-ODP LB film surface (light brown), and the OTS SAM surface exposed in the shaved regions of the LB film (yellow).

Patterns of various shapes and resolutions have been produced within the metal-ODP surfaces using AFM nanodisplacement, as illustrated in Figure 65. The first image (left) shows a series of parallel lines with a *ca.* 1 μm^2 separation, and a typical line width of 190 nm. The patterns again indicate efficient nanodisplacement of the LB film by the AFM probe, with complete removal of the LB film material from the patterned regions. Preparation of such high aspect ratio patterns (with efficient nanodisplacement of the film maintained across the whole the patterned structure), were found to be consistently reproducible with the line lengths in excess of 10 μm. The second image (middle), consisting of two "cross" patterns, demonstrates the production of smaller line lengths (the two lines of the crosses each correspond to a length of 3 μm) but with similar resolutions to the first pattern. The production of such patterns was found to require careful regulation of the number of passes of the AFM probe over the pattern region during the nanodisplacement process. The use of excessive nanodisplacement time scales (estimated to be typically > *ca.* 5 seconds for such high aspect ratio features) was found to have a considerable influence upon the line width of the features produced, resulting in increased line widths. This behaviour is believed to be a technical issue arising from drift of the AFM probe position upon the sample surface as it raster scans over the defined area. This is highlighted by the cross patterns shown in Figure 65 where the second cross (right) shows an increase line width (250 - 270 nm) arising from an increase in the nanodisplacement process time period during the patterning procedure. It should be noted that the exact effect of the nanodisplacement time period is also dependent upon other factors such as the size of the patterned area and the scan rate employed (due to their effect upon the time taken for the probe to travel across the desired patterning area). The final image (right) shown in Figure 65 demonstrates the production of larger pattern features, showing three squares with line edges of 600 nm, and a 1 μm separation between each of the squares.

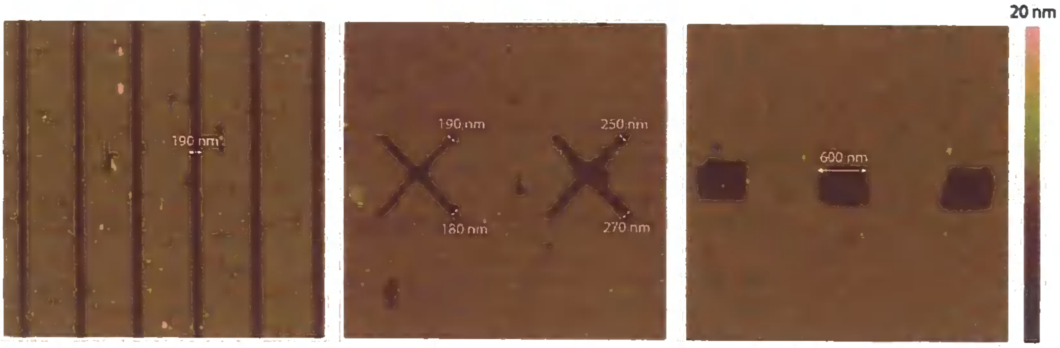

Figure 65. AFM images of 10 x 10 μm^2 (left), 9 x 9 μm^2 (middle) and 4 x 4 μm^2 (right) regions showing a range of different patterns producible upon Zr-ODP LB film by spatially resolved AFM nanodisplacement of the LB film material.

The production of such patterns is typically achieved using four full passes (*i.e.* x 2 traces, and x 2 retraces) of the AFM probe over the pattern area. The pattern resolutions demonstrated here (with line widths down to 180 nm) remain larger than those reported by Liu *et al.*[168] (10 nm line widths) when using a similar AFM nanodisplacement strategy upon Au-supported alkanethiolate SAMs. However, the aim of the patterns shown here is to demonstrate the versatility of the nanodisplacement patterning of such metal-ODP films, as illustrated by the examples in Figure 65, with a range of pattern shapes and sizes shown to be producible. Later examples also highlight the ability of this SPL technique for providing sub-100 nm resolutions, approaching those reported by Liu (see Section 5.2.2).

High levels of stability are associated with the patterns, with complete structural retention of the shaved features observed upon exposure to a variety of aqueous and non-aqueous (EtOH, $CHCl_3$, CH_2Cl_2, CH_3COCH_3, THF) solvents. Exposure of LB films to solvents at temperatures up to 80 °C was also shown to have no effect upon the patterned features (temperatures above this value were not investigated).

5.2.2 *Hafnium-octadecylphosphonate*

Nanopatterning of Hf-ODP LB monolayers has also been successfully carried out, employing the same AFM nanodisplacement strategy as described for Zr-ODP films. The stability of the Hf-ODP films (see Section 3.2 for preparation) are comparable to the corresponding zirconium films, with consistent nanodisplacement of the LB layer taking place with an applied vertical force in excess of *ca.* 40 nN. Cross section profiles of patterns shaved into the Hf-ODP films (Figure 66) show a film depth (5.5 ± 0.5 nm) corresponding to the presence of a *ca.* 3 nm thick hafnium layer (assuming a ODP monolayer of *ca.* 2.5 nm thickness[20]). This again shows that metal ion assembly upon the LB film surface using $HfOCl_2{\cdot}xH_2O$ (x = 6 - 8) solutions, leads to the formation of thicker inorganic metal layers (Hf-ODP: 5.1 ± 0.2 nm) than corresponding $ZrOCl_2{\cdot}8H_2O$ solutions (Zr-ODP: 4.6 ± 0.2 nm), see Section 3.2.2. However, the Hf-ODP pattern depths are greater than those obtained from the previous defective Hf-ODP films investigated. This contrast between the depths may suggest that in the defective Hf-ODP films, ODP-H_2 molecules remained present in the film defects, but in a highly disordered state. This would account for the *ca.* 0.4 nm increase in the Hf-ODP film thickness determined from the patterned films, where the nanodisplacement process is believed to efficiently remove all traces of the LB film material from the shaved regions. The increased values of the pattern depths are not believed to be a result of any disruption to the underlying OTS SAM due to its high stability, as previously discussed (see Section 5.2.1).

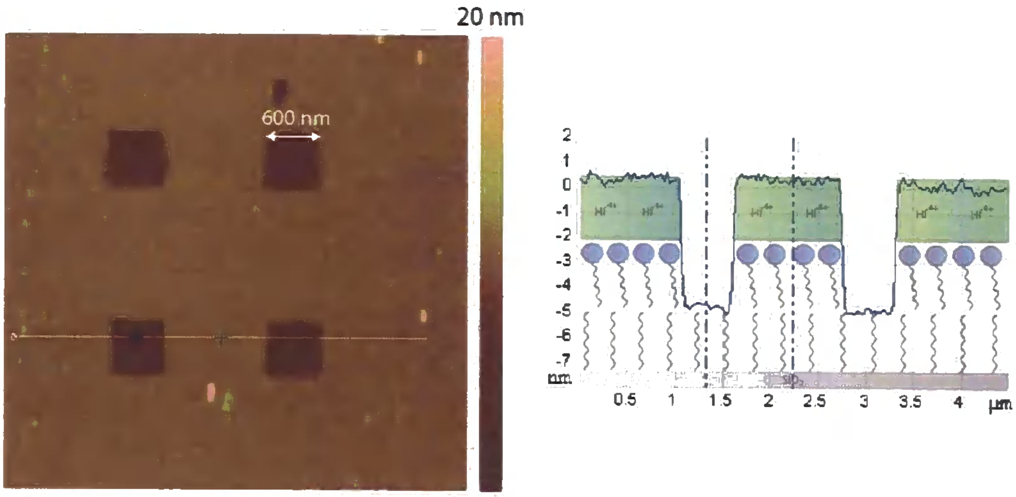

Figure 66. Contact mode AFM image (left) of 5 x 5 μm^2 region of Hf-ODP LB monolayer, showing patterned 600 x 600 nm^2 squares (dark brown) shaved into the LB film (light brown/yellow) and a corresponding cross section profile of the patterned surface (right) shows the depth of the shaved features and a cartoon representation of the proposed film structure.

Patterns with sub-100 nm resolution are shown in Figure 67 with line widths (down to 30 nm) approaching those reported by Liu *et al.*[168] during similar AFM nanodisplacement patterning of alkanethiolate SAMs upon Au. Production of such narrow features required stringent control over the movement of the AFM probe over LB film surface, typically being restricted to no more than two passes (*i.e.* trace and retrace) of the probe over the surface region. Difficulties were also encountered in the consistently achieving efficient nanodisplacement in the LB layer, whilst maintaining such high spatial resolutions. Disruptions to such shaved features were observed on occasions, arising from failure of the AFM probe to displace the LB film material. More consistent and reproducible levels of surface patterning were achievable with an associated line width of 70 - 80 nm (Figure 67), upon increasing the number of passes of the AFM probed over the desired patterned region (typically *ca.* x 5 - 10 passes). The differences in the resolution achieved are again believed to be a result of the precision with which the AFM probe is positioned and scanned across the sample surface.

In a similar fashion to Zr-ODP films previously discussed (see Section 5.2.1), friction force images indicate compositional differences across the patterned Hf-ODP surfaces arising from the different frictional characteristics of the exposed OTS SAM in the patterned film regions, and the surrounding Hf-ODP LB film.

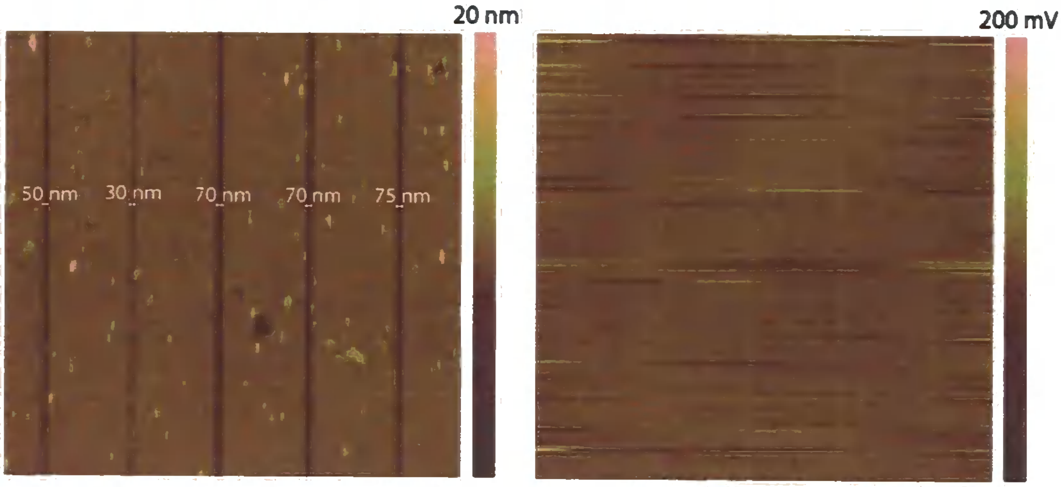

Figure 67. Contact mode AFM image (left) and the corresponding friction force image (right) of a 6 x 6 μm^2 region of a patterned Hf-ODP LB monolayer. Trenches (dark brown) down to 30 nm in line width are shown to be shaved in the LB film (light brown/yellow) in the topographical image, with the values stated indicating the resolution of each shaved feature. The friction image highlights differences in the frictional characteristics of the Hf-ODP film (brown) and the OTS SAM surface exposed in the shaved regions of the LB film (yellow).

Patterns such as those presented in Figures 66 and 67 are produced through controlled scanning of the AFM probe across the desired regions of the LB film surface, with the vertical forces exerted by the probe being above the film displacement threshold. Figure 68 demonstrates a 3 x 3 array of "pinholes" produced through focusing the AFM probe upon a single surface point, and applying vertical forces above the film displacement threshold to "puncture" the film surface. The resulting array shows pinhole features with *ca.* 100 - 200 nm dimensions. Variations observed in the shape and dimensions of the features produced are believed to be a result of the stability of the AFM probe to be maintained at a single point location upon the sample surface, *i.e.* even when directed to a single point at the LB film surface, factors such as "drift" of the tip are thought to lead to the elongated appearance of the shaved features.

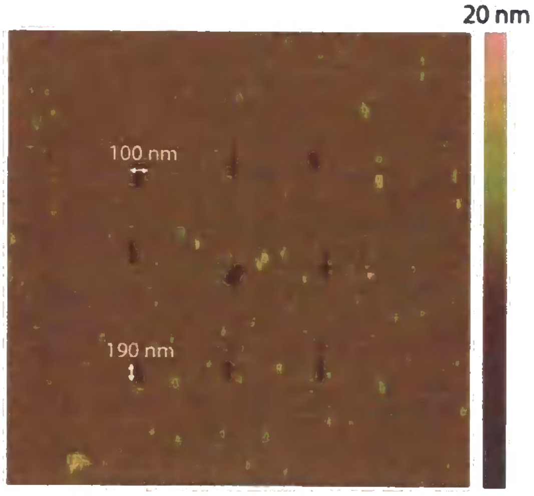

Figure 68. Tapping mode AFM image of a 5 x 5 μm^2 region of a patterned Hf-ODP LB monolayer, showing a 3 x 3 array of pinholes (dark brown) "punctured" into the LB film (light brown/yellow) by the AFM probe. The values on the image indicate the resolution of the patterned features.

High levels of stability were again associated with the patterned surfaces, with complete retention of the structures following treatment in both water and a variety of organic solvents.

5.2.3 Magnesia-octadecylphosphonate

Further AFM nanodisplacement studies were carried out into patterning of magnesia-ODP LB films, prepared through sol-gel growth of the magnesia layer upon an ODP-H_2 LB film deposited from a 0.5 mM Mg^{2+} subphase, as described in Section 4.3.2. The sol-gel films were determined from force curve studies to show a moderate increase in stability in comparison to Zr-ODP and Hf-ODP LB (*ca.* 40 nN film displacement threshold) films with a higher threshold value (*ca.* 50 nN) determined for efficient nanodisplacement in the LB film. However, it should be noted that some degree of error is present in the calculated vertical forces due to the error associated with the spring constant values of the AFM probes (provided by the probe manufacturer). The difference between the reported threshold values of the Zr-ODP/Hf-ODP and magnesia-ODP films may consequently lie within the limits of error in the calculation.

Further evidence relating to the production of more robust films derived from sol-gel structures can be observed in the quality of the resultant patterns, however. Attempts to generate high resolution patterns (line widths > 200 nm) typically resulted in inconsistent shaved structures. Figure 69 shows an AFM image of a typical pattern consisting of a series of parallel lines spaced *ca.* 2 μm apart, where inefficient nanodisplacement of the pattern regions is shown to result in discontinuous line structures, as indicated by the blue arrows.

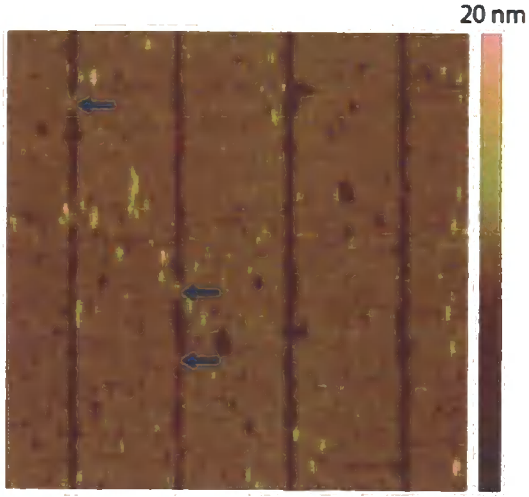

Figure 69. Contact mode AFM image of a 10 x 10 μm^2 region of a patterned magnesia-ODP LB monolayer, showing a series of parallel lines (dark brown) of *ca.* 150 nm line width shaved in the LB layer (light brown/yellow). The blue arrows show areas within the pattern regions where nanodisplacement of the LB film has failed to take place.

Greater success was found in patterning larger surface features such as 1 x 1 μm^2 regions as illustrated in Figure 71, with more consistent shaving of the patterned film regions observed. This is thought to be due to the production of larger features being influenced less by the effects of the drift of the AFM probe, which may occur during extended periods of the film displacement process, *i.e.* drift will result in a larger error in the resolution of a high aspect ratio feature such as the 150 nm wide lines shown in Figure 63, in comparison to the production of larger features of low aspect ratio such as the 1 x 1 μm^2 squares shown in Figure 70. The use of longer film displacement times for larger features, proved beneficial for ensuring that complete displacement of the LB film in the pattern region occurred.

The cross section profile of the patterned magnesia-ODP LB film in Figure 70 shows an associated depth of 5.7 ± 0.4 nm with the shaved structures. This is considerably larger than the film thickness determined from the cross section profile of the defects (4.8 ± 0.3 nm) present in the magnesia-ODP LB film structure as previously described, see Section 4.3.4. This again may be attributed to the presence of highly disordered ODP-H_2 molecules, or small aggregates of the magnesia sol-gel present within the defects in the magnesia-ODP film, resulting in their apparent lower depths. In contrast, nanodisplacement patterning leads to efficient removal all of the magnesia-ODP film material from within the patterned regions, leading to the larger depths of these features that are observed. Another notable feature of the patterned magnesia-ODP surfaces was the build up of the displaced film material commonly observed around the periphery of the shaved features (Figure 71, red arrows).

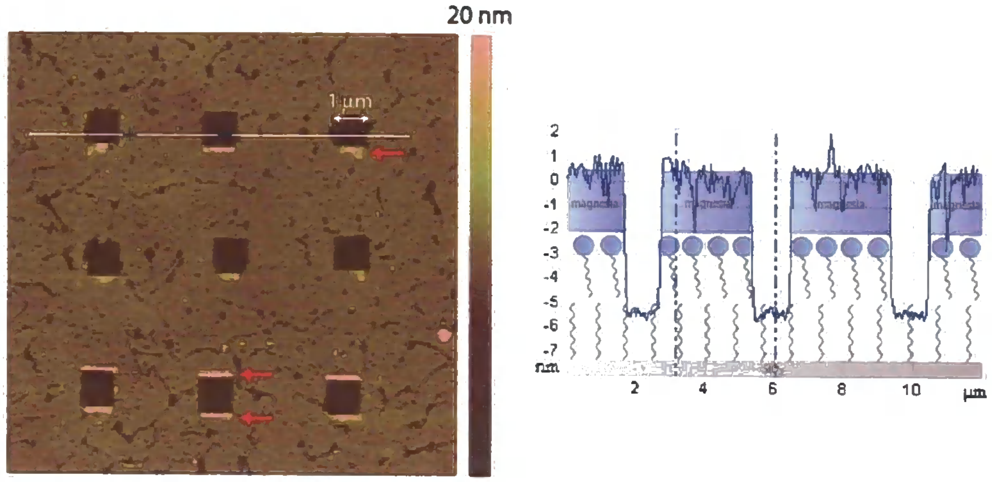

Figure 70. Contact mode AFM image (left) of 10 x 10 µm^2 region of patterned magnesia-ODP LB film showing 1 x 1 µm^2 squares (dark brown) shaved into the LB layer (light brown/yellow). The red arrows indicate regions where the displaced film material has deposited around the periphery of the patterned region. The corresponding cross section profile of the patterned surface (right) is shown, indicating the depth of the etched features and shows a cartoon representation of the proposed film structure.

Friction force imaging of the patterned surfaces provided results consistent with those previously observed for Zr-ODP and Hf-ODP LB films, with contrast observed between the frictional forces experienced by the AFM probe in pattern film regions (OTS surface), and surrounding magnesia surface, Figure 71.

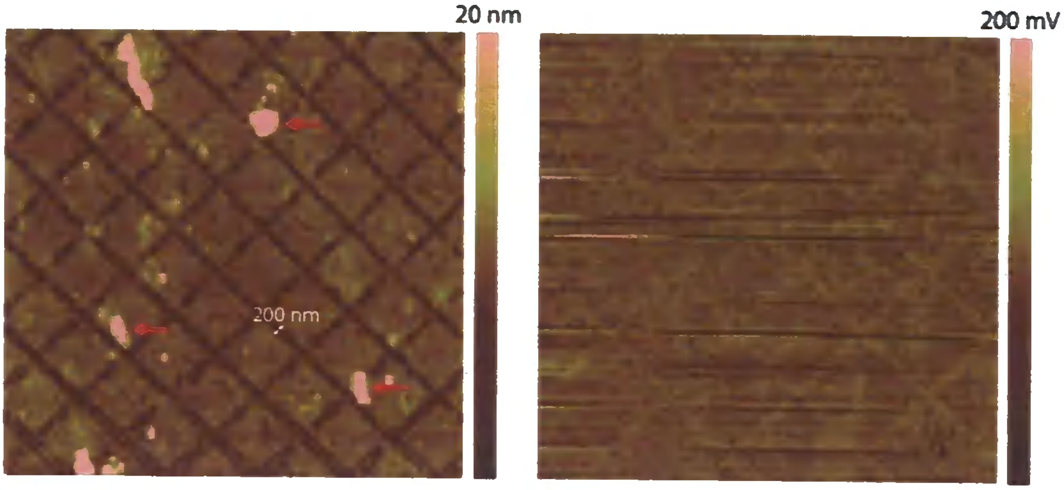

Figure 71. Contact mode AFM image (left) of a 12 x 12 μm^2 region of a patterned magnesia-ODP LB monolayer, showing a grid pattern (dark brown) shaved in the LB film (light brown/yellow). The value on the AFM image indicates the resolution of the shaved features. The red arrows highlight regions where the displaced material from the patterned regions has been deposited upon the sample surface. The friction force AFM image of a 6 x 6 μm^2 region of the magnesia-ODP LB monolayer highlights differences in the frictional characteristics of the magnesia-ODP film (brown) and the underlying OTS-modified Si/SiO$_2$ substrate exposed in the shaved regions of the LB film (yellow).

5.3 *Nanopatterned metal oxide films*

Thermal treatment of Zr-ODP and Hf-ODP LB films has already been demonstrated to provide a route to generating homogenous, nanometer-thick metal oxide films due to the assembly of the inorganic metal layer as a *ca.* 2 nm thick film arising from the tendency of Zr^{4+} and Hf^{4+} ions to form polymeric structures in solution (see Section 3.2.3). Similar success was also found in exploiting the sol-gel chemistry of the metal alkoxide, $Mg(OEt)_2$ for the preparation of magnesia-ODP LB films, in which nanometer-thick sol-gel films of magnesia are found to form upon the LB film surface. The formation of homogenous metal oxide surfaces through thermal treatment of the patterned metal-ODP LB films that have been described here is found to show complete retention of the patterned structures in the metal oxide, as illustrated by the AFM data shown in Figure 72. These images show three sets of patterns produced upon Zr-ODP (top left), Hf-ODP (top middle) and magnesia-ODP (top right) LB monolayers deposited upon OTS-modified Si/SiO$_2$ substrates with the corresponding metal oxide films following thermal treatment (500 °C) shown below them. The images illustrate the high levels of retention observed in the patterns upon thermal treatment, with no evidence of deformation or degrading of the shaved structures. The high precision transfer of the patterns during the metal oxide formation highlights the effectiveness of the metal-ODP LB monolayer to act as a surface template, which can control the morphology of the final metal oxide film generated.

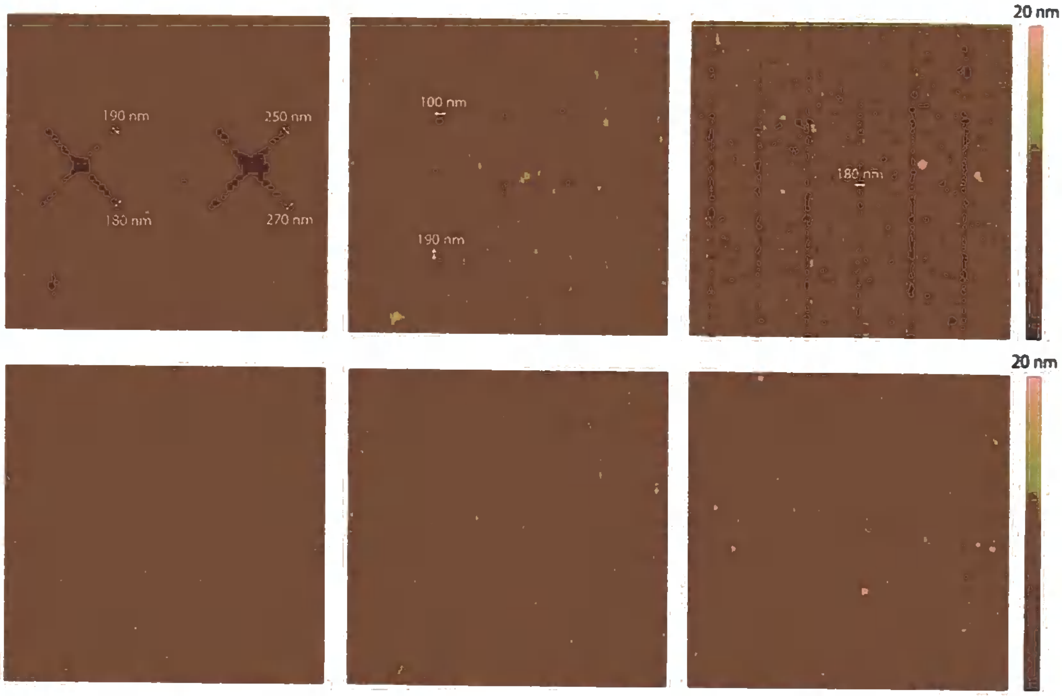

Figure 72. TappingMode^{TM} AFM image of 9 x 9 μm^2 (top left), 5 x 5 μm^2 (top middle), 12 x 12 μm^2 (top right) regions of patterned Zr-ODP, Hf-ODP, and magnesia-ODP LB monolayers respectively, supported upon an OTS-modified Si/SiO$_2$ substrate. The TappingMode^{TM} images below show the corresponding metal oxide films produced following thermal treatment (500 °C).

From initial evaluation of the AFM images of the patterned metal-ODP films both before and after the thermal treatment, a reduction in the pattern depths is apparent (based upon the colour scale of the images, Figure 72). This is attributed to the decomposition of the organic film components under the high temperatures (500 °C) of the thermal treatment step. Figure 73 shows three AFM images with the corresponding cross section profiles underneath of patterned ZrO_2 (left), HfO_2 (middle) and MgO (right) films, highlighting the observed reduction in the film thickness. Evaluation of the pattern depths in the generated zirconium, hafnium and magnesium metal oxide surfaces reveal film thickness values of 1.6 ± 0.3 nm, 1.7 ± 0.3 nm, and 1.3 ± 0.3 nm respectively. These values correspond to a reduction of *ca.* 3.0 nm, *ca.* 3.8 nm and *ca.* 4.4 nm in the film thickness during the formation of the respective metal oxide surfaces. In context of the contribution to the initial metal-ODP film thickness by the ODP molecules (*ca.* 2.5 nm[20]), this suggests the inorganic zirconium, hafnium and magnesia layers undergo varying degrees of contraction (Zr : *ca.* 0.5 nm, Hf : *ca.* 1.3 nm, Mg : *ca.* 1.9 nm) during the calcination process. The thicknesses of these patterned metal oxide films prove in good agreement with the metal oxide thickness values determined from AFM analysis of the defective ZrO_2 (1.7 ± 0.2 nm) and HfO_2 (1.5 ± 0.2 nm) and MgO (1.5 ± 0.2 nm) films, see Sections 3.2.3 and 4.3.4.1.

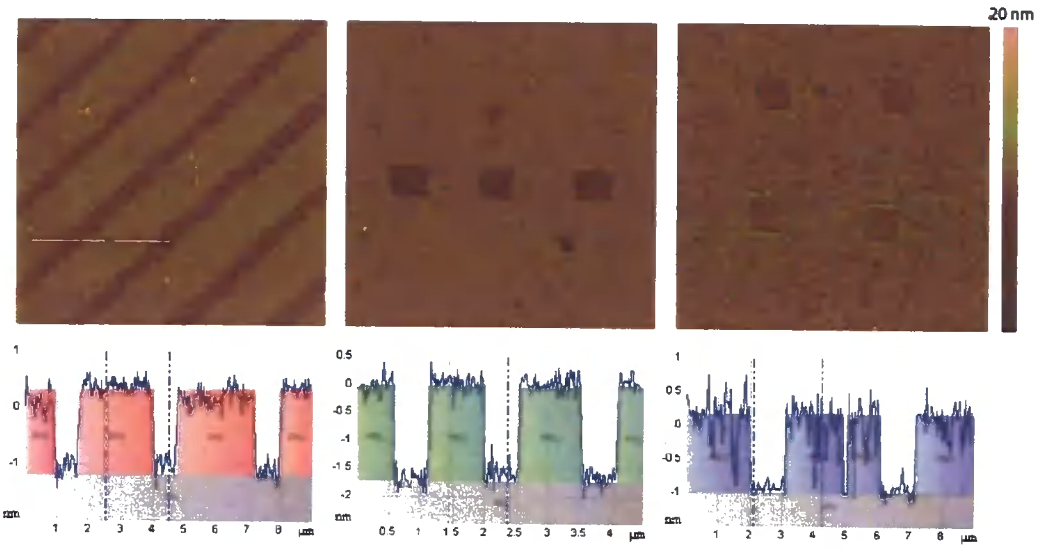

Figure 73. Tapping mode AFM images of a 10 x 10 µm^2 region of a patterned ZrO_2 film (top left) a 5 x 5 µm^2 region of a patterned HfO_2 film (top middle), and a 10 x 10 µm^2 region of a patterned MgO film (top right), and the corresponding cross section profiles (bottom) of the patterned surfaces showing the depth of the shaved features and a cartoon representation of the film structure.

5.4 *Conclusions*

Successful patterning of metal-ODP LB monolayers supported upon OTS-modified Si/SiO_2 substrates has been described. The fabrication of patterns in the LB film structure was carried out through selective shaving, or nanodisplacement of the metal-ODP LB layer by the application of high applied loads (*ca.* 40 - 50 nN) upon the film surface using an AFM probe. The "soft" nature of the LB layer enables the film structure to be readily disrupted by the AFM probe, producing well-defined, spatially resolved patterns within which complete removal of the LB film material takes place. Particular success was found in patterning of Zr-ODP and Hf-ODP films with shaved features offering resolutions (down to 30 nm line width) approaching those first demonstrated by Liu *et al.*[168] upon alkanethiolate SAMs (10 nm line widths). LB films of magnesia-ODP were observed to be more robust, with the production of such high resolution patterns proving less consistent. However, more success was found in patterning larger surface structures (1 x 1 μm^2) upon such films.

Thermal treatment of the patterned organic-inorganic hybrid films, used to simultaneously decompose organic films components and calcine the inorganic metal layer, was found to result in excellent levels of retention of the patterns in the resulting metal oxide films. The preparation of such "soft" organic and "hard" metal nanostructures holds significant potential, having already been exploited in the development of biodiagnostic tools,[251] and showing potential in the development of nanoelectronic and optical devices.[1,250]

Chapter 6

6. *Preparation of nanopatterned amino-functionalised surfaces*

6.1 *Introduction*

Patterning of Langmuir-Blodgett (LB) monolayers using the AFM nanodisplacement technique previously described has been demonstrated upon LB films supported upon octadecyltrichlorosilane (OTS)-modified Si/SiO_2 substrates (see Chapter 5). Spatially resolved nanodisplacement of the LB layer reveals the underlying OTS SAM, creating chemically well-defined surface domains within the LB film structure with the CH_3 terminal groups of the OTS molcules, at the film-air interface. Similar nanodisplacement patterning of LB films prepared upon alternative substrate-supported SAMs offers a potential route to production of nanometer-scale patterns which can exhibit a range of different surface functionalities.

The fabrication of such functional micro and nanoscale structures upon a solid support allows for tailoring of surface properties such as wetting behaviour,[264] adhesion,[265] friction,[266] within spatially defined surface regions. Perhaps one of the most significant roles of such structures however, is their potential to facilitate a range of spatially resolved, chemical reactions upon the surface.[267]

The preparation of SAMs upon a variety of different substrates has been well established with the formation of a range of organosilane monolayers upon Si/SiO_2 substrates being well known.[13,43,46] One of the most extensively studied organosilane systems are amino-functionalised monolayers typically prepared using 3-aminopropyltrimethoxysilane (APTMS),[268,269] and 3-aminopropyltriethoxysilane (APTES).[62,270] Amino-functionalised surfaces are of particular interest due to the role that such aminosilanes can perform as a "primer" molecule, acting as anchor sites for binding of a variety of molecules including enzymes and antibodies,[271] fluorescence molecules,[272] and inorganic nanoparticles.[273]

Much of the current work reported into the fabrication of patterned amino-functionalised surfaces focus upon their use as templates for directing surface binding of Au nanoparticles (AuNPs).[274] The controlled assembly of two-dimensional micro and nanostructures of metal colloid nanoparticles holds significant potential in chemical and biological detection[275,276] as well as in the electronics[277,278] and photonics[279] industries. Several techniques have been used to pattern aminosilane films for subsequent template-directed assembly of AuNPs using top-down lithographic approaches. Electric-field induced microcontact electrochemical conversion (MEC) of aminosilane films has been described for example,[280] in which an electric bias is applied across an electrochemical stamp in contact with the substrate surface. Anodic oxidation of the amine surface, induced by localised electrical fields experienced at the microcontacted areas, results in patterned SiO_2 domains within the SAM surface. A similar concept reported by Li and coworkers[281] describes spatially resolved electrochemical oxidation of OTS SAMs upon Si/SiO_2 substrates. Subsequent amine patterns are created through backfilling of the newly oxidised SiO_2 regions by APTMS assembly. Preece *et al.* [282] reported the use of chemical electron-beam lithography upon NO_2-terminated SAMs, providing a direct write method for the fabrication of patterned amino-functionalised surfaces, through selective reduction of the NO_2 functionality to NH_2 groups.

Here, a novel top-down approach is described towards the fabrication of patterned amino-functionalised micro and nanostructures, using the AFM nanodisplacement strategy for spatially resolved shaving of a LB "mask" to reveal the underlying amino-functionalised surface, Scheme 7.

Amine modification of the Si/SiO$_2$ substrate is carried out using established surface silanisation strategies, with APTMS as the SAM precursor compound. "Masking" of the amine surface is subsequently carried out through "tail-down" assembly of a metal-ODP LB monolayer upon the modified substrate surface, see Scheme 7. Spatially resolved surface domains in which the amine functionality is exposed to the environment directly above the substrate are achieved by AFM nanodisplacement of the LB film, using an AFM probe.

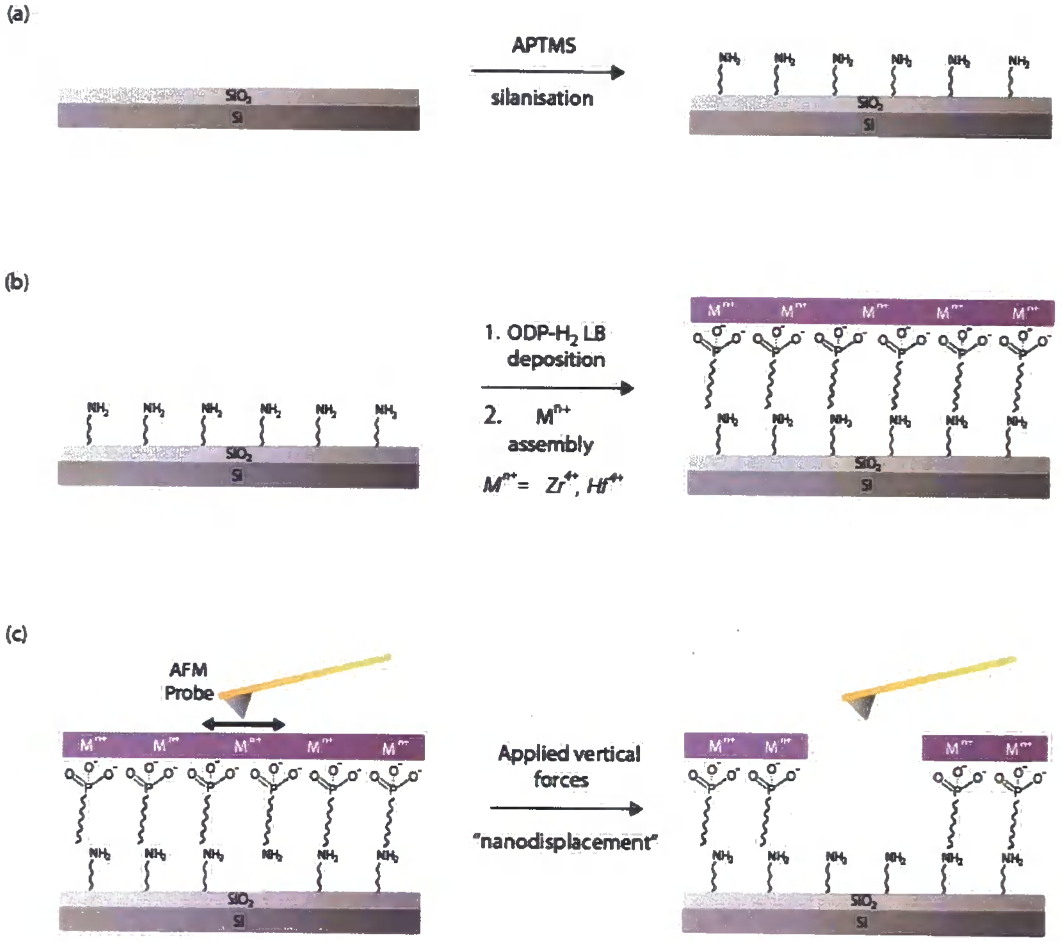

Scheme 7. Schematic representation of the production of patterned amino-functionalised surfaces: (a) Silanisation of Si/SiO_2 substrate using a 1mM APTMS solution in anhydrous toluene to produce an amino-functionalised surface. (b) "Tail-down" LB deposition of an ODP-H_2 monolayer upon the amine surface, and subsequent assembly of a metal layer (M^{n+} = Zr^{4+}, Hf^{4+}) to stabilise the LB film. (c) Spatially resolved AFM nanodisplacement of the metal-ODP LB layer to reveal the underlying amino-functionalised surface.

6.2 Preparation of APTMS / ODP-metal hybrid bilayer films

6.2.1 APTMS film preparation

Amino-functionalised films were produced upon chemically oxidised Si/SiO_2 substrates in 1 mM solutions of APTMS prepared in anhydrous toluene. The water content in the APTMS solution was minimised to restrict hydrolysis of the silane groups in the bulk solvent which would otherwise facilitate excessive polymerisation of the APTMS molecules[53] resulting in the formation of rough aminosilane films unsuitable for LB deposition (*c.f.* OTS SAM formation; see Section 3.2.1).

Aminosilane film growth under anhydrous conditions occurs by a similar mechanism to the formation of smooth OTS SAMs (see Section 3.2.1) with hydrolysis of the APTMS molecules limited to the Si/SiO_2 substrate surface (upon which a thin water layer is present). The hydrolysed molecules adsorb to the substrate surface and can form crosslinked networks through nucleophilic substitution reactions occurring between the silane headgroups to form Si–O–Si linkages.

AFM analysis of the ATPMS films reveals the presence of a uniform surface with a typical rms roughness of 0.3 ± 0.1 nm over 5 x 5 μm^2 surface regions, Figure 74. Particulates, observed to be sparsely distributed across the film surface, as highlighted in Figure 74 (blue arrows), are thought to be aggregates of APTMS molecules bound to the aminosilane film surface. The formation of such aggregates is likely to arise from a limited degree of excessive polymerisation of the APTMS molecules, onset by traces of moisture in the APTMS solution.

An increase in the number of aggregates populating the APTMS surface is generally observed in comparison to previous OTS SAMs produced (see Section 3.2.1). The film quality of APTMS surfaces was also found to show a significant dependency upon the reaction time, with surfaces prepared over 24 hour periods commonly resulting in highly rough surfaces (a typical surface reaction time was limited to 3 - 4 hours). This film growth behaviour is explained by the basic amine groups present in the APTMS molecules self-catalysing the hydrolysis reactions, resulting in more facile silanisation of the substrate surface.[62] The aminosilane molecules can also form zwitterions in solution (through interactions between the amine and silane groups)[283] which can lead to increased binding of the molecules at the substrate surface, with multilayer film formation possible.

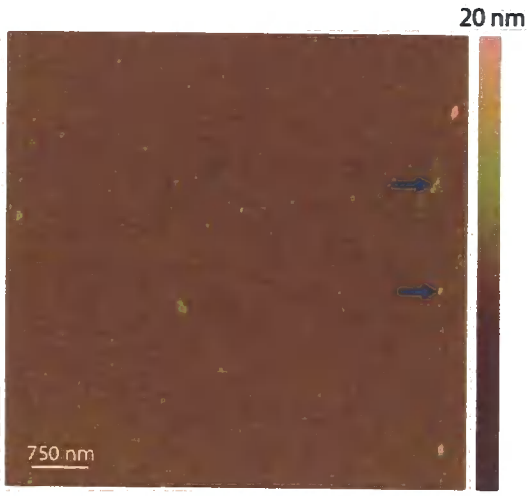

Figure 74. TappingMode™ AFM image of 6 x 6 μm^2 region of an APTMS film prepared upon a Si/SiO$_2$ substrate. The blue arrows highlight surface bound particulates of physisorbed aggregates of polymerised APTMS.

Static contact angle values reveal the modified substrate to be relatively hydrophobic in character (94 ± 2°). This suggests an appreciable degree of disorder associated with the surface bound aminosilane molecules, with the C$_3$-hydrocarbon chains of the molecules exposed at the film-air interface. Disordering within the molecular structure of the film is not surprising with the amine groups able to undergo hydrogen bonding, or accept a proton from the surface silanol groups to form a quaternary amine.[65] Bending within the molecular structure can also allow for both the silane and amine groups to orientate towards the substrate surface, Figure 75a.[66] An idealised APTMS film structure would be expected to exhibit lower contact angle values due to the amine groups being orientated towards the film exterior (forming hydrogen bonds with the H_2O molecules, Figure 75b).

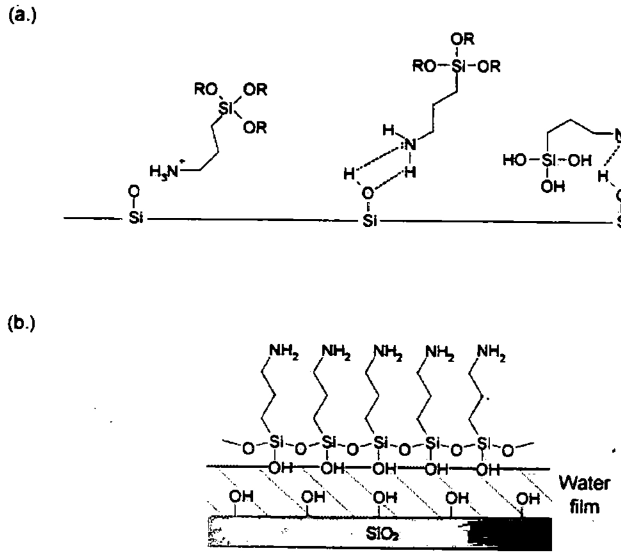

Figure 75. (a) Schematic of the possible interactions of the amine group of the aminosilane molecules with the silanol groups of a Si/SiO_2 substrate, through amine protonation (left), hydrogen bonding (middle), and hydrogen bonding coupled with bending of the molecule leaving both the head and tail group orientated towards the substrate surface (right). (b) Schematic of the idealised structure of an APTMS film.

XPS analysis of the aminosilane film surface confirms the presence of carbon (C 1s, 285.00 eV), oxygen (O 1s, 532.1 eV), nitrogen (N 1s, 401.8 eV, 399.90 eV), and chlorine (Cl 2p, 197.9 eV, 199.5 eV).

An idealised aminosilane film, in which complete hydrolysis of the APTMS molecules has taken place with all three methoxy groups replaced by the formation of Si–O–Si bonds, would provide a carbon to nitrogen ratio of 3 : 1. However, significantly higher C : N ratios (7 : 1) are observed, thought to occur due to incomplete hydrolysis of the Si–OMe groups of the APTMS molecules arising from the anhydrous conditions employed during the silanisation process, and the presence of adventitious carbon at the film surface.

The N 1s signal shows two peaks centred at 399.9 eV and 401.7 eV indicating the presence of the APTMS molecules upon the substrate surface. The peak at 399.9 eV was assigned to the free amino groups, while the signal at higher binding energy suggests the presence of hydrogen bonded or protonated amine groups.[284,285,286] The C 1s signal, centred at 285.0 eV, also shows a shoulder at a higher binding energy, Figure 76. The appearance of this peak is attributed to the presence of three carbon signals arising from the CH_2 (Si–CH_2–, and –CH_2–) groups in the in ATPMS molecule centred at 285.0 eV, and the CH_2 group bonded to the amine (H_2N–CH_2–) centred at 286.0 eV, and also a 288.9 eV.

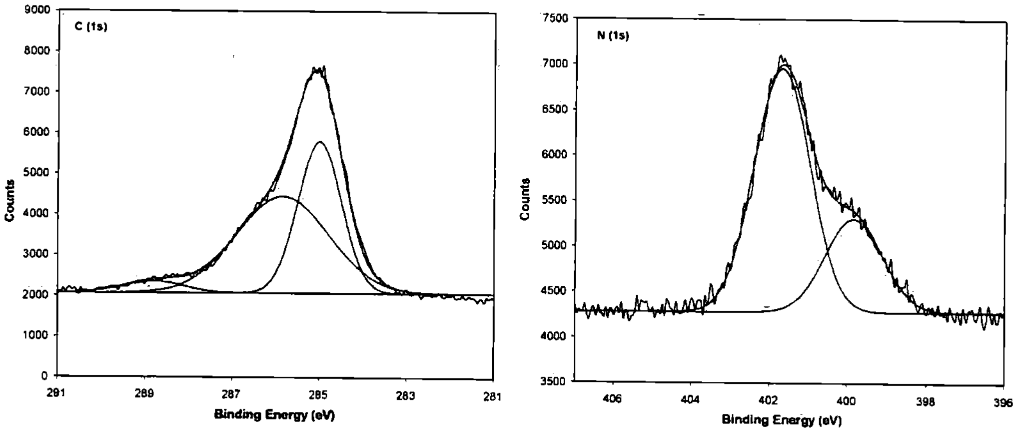

Figure 76. XPS C 1s (left) and N 1s (right) spectra of an APTMS film supported upon a Si/SiO_2 substrate.

The protonated/hydrogen bonded amines dominate the surface of the aminosilane film with the ratio to the free amine determined to be 5 : 2. Though it is intuitive to attribute hydrogen bond formation to taking place between the amine groups at the film exterior (as would be expected if the film formation resulted in a highly ordered monolayer), interactions between the amine and surface silanol groups are also known to take place through orientation of the amine group towards the substrate surface as discussed previously in this section.[65,66] Both the formation of hydrogen bonds and amine protonation (through donation of the silanol proton, see Figure 75a) at the substrate surface, as well as hydrogen bonding between amine groups of the APTMS molecules, will contribute to the N 1s signal at higher binding energy.

Further amine protonation is also believed to arise from the presence of residual HCl, originating from the pretreatment cleaning of the Si/SiO_2 substrate (1 : 1 H_2O_2/HCl solution treatment of substrate at room temperature) prior to aminosilane film formation. This theory is supported by the presence of chlorine (Cl 2p, 197.9 eV, 199.5 eV) in the film structure, probably from $RNH_3^+Cl^-$ salt formation.

6.2.2 Langmuir-Blodgett deposition of metal-octadecylphosphonate monolayers

"Tail-down" deposition of octadecylphosphonic acid (ODP-H_2) LB monolayers upon the APTMS-modified Si/SiO_2 substrates was carried out upon both pure H_2O and a 0.25 mM $CaCl_2$ aqueous subphase surface at 22 mN/m surface pressure, see Scheme 7. The hydrophobic character exhibited by the aminosilane films, as indicated by the static contact angle measurements (94 ± 2 °, see Section 6.2.1) allows for successful "tail-down" deposition of LB films upon the modified substrate surface. Stabilisation of the deposited film was provided by treatment in 0.5 mM aqueous $ZrOCl_2 \cdot 8H_2O$ solution, forming a polymeric zirconium film which acts to crosslink the underlying LB film (see Chapter 3).

π–A isotherms produced upon the Ca^{2+} subphase show an expansion of the monolayer film (average molecular area: 28.8 ± 2.5 Å^2) in comparison to ODP-H_2 monolayers prepared upon pure H_2O (24.7 ± 2.5 Å^2), Figure 77. This increase in the average molecular area is suggested to occur due to the association of the Ca^{2+} ions between the monolayer headgroups.

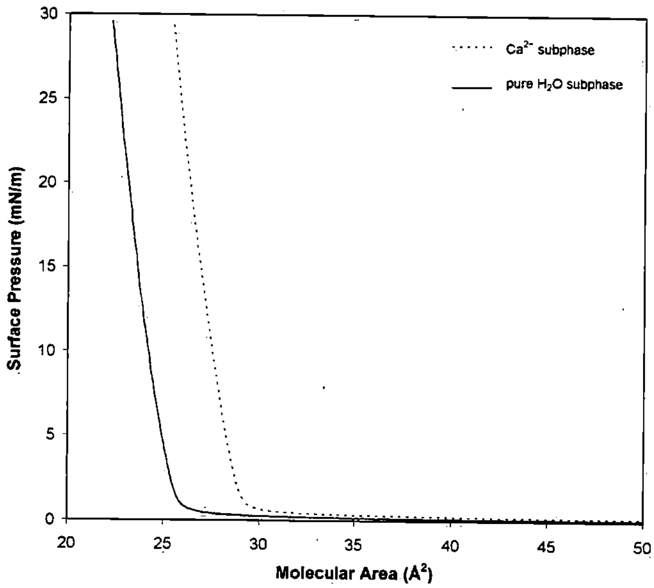

Figure 77. π–A isotherms of ODP monolayers prepared upon a pure H_2O subphase (solid line), and a 0.25 mM $CaCl_2$ subphase (dashed line).

Subphases containing metal ions were employed during Langmuir film formation to circumvent problems of the low quality LB film deposition observed on the APTMS-modified Si/SiO_2 substrates when carried out upon a pure H_2O subphase. AFM images show the ODP-H_2 monolayers (following Zr^{4+} treatment) transferred from pure H_2O subphases contained numerous defects at the island-island interfaces in the LB film, see Figure 78 (blue arrows). Defects were also seen to frequently occur within the interior regions of the island domains, Figure 78 (red arrows). The occurrence of these defects is thought to be a consequence of the surface properties of the aminosilane film rather than from the LB procedure, as similar monolayers deposited from a pure H_2O subphase upon OTS SAMs have previously been demonstrated to result in highly uniform, low defect films (see Section 3.2.2). A reduction in the efficiency of the film transfer to the amine surface can be expected due to the reduced hydrophobic character of the APTMS SAM (relative to the OTS-modified Si/SiO_2 substrates).

The cross section profile of the film surface (Figure 78) reveals a typical depth of 4.6 ± 0.4 nm associated with the defects, consistent with the thickness of Zr-ODP films deposited upon OTS SAMs (see Section 3.2.2).

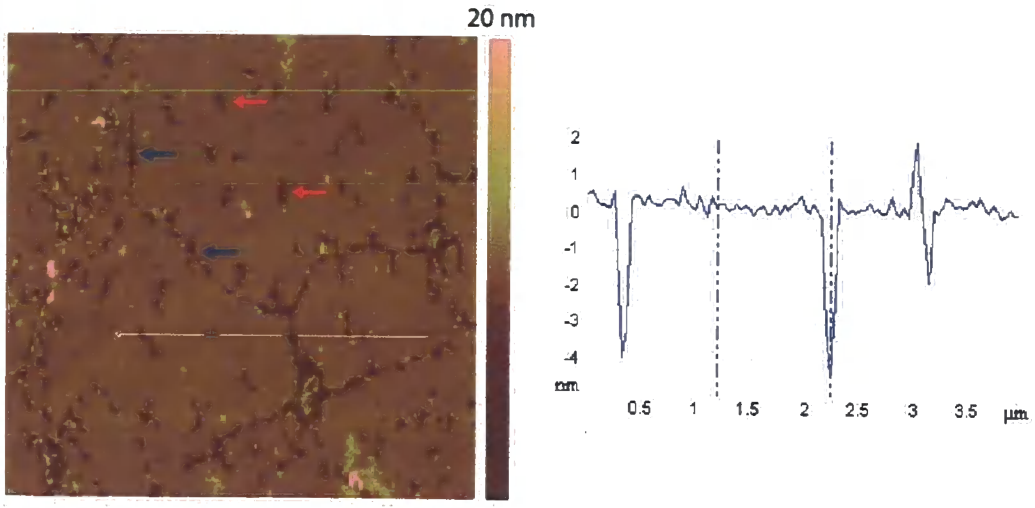

Figure 78. TappingMode™ AFM image (left) of 6 x 6 μm^2 region of Zr-ODP LB monolayer transferred from a pure H_2O subphase to an ATPMS-modified Si/SiO_2 substrate, and a corresponding cross section of the film surface (right).

LB films transferred to the APTMS-modified Si/SiO_2 substrates from a Ca^{2+} subphase show a significant reduction in the number of defects observed both at the interfaces between the island domains in the LB film structure, and within the interior of the islands structures, Figure 79. The film Zr-ODP surface typically show a small increase in the rms roughness (0.5 ± 0.1 nm) in comparison to previous metal-ODP LB films prepared upon OTS SAM surfaces as described in Chapter 3.

The cross section profiles of the surface reveals a small increase in the film thickness (4.9 ± 0.4 nm) as determined from the depth of the film defects. The reason for this small increase in the film thickness is currently unclear, though may be a consequence of the presence Ca^{2+} ions which may contribute to the film thickness either through binding to the monolayer headgroups, or becoming incorporated into, or influencing the growth of the zirconium layer upon the LB film surface. A reduction in the subphase pH as a result of the addition of $CaCl_2$ for example, may influence the nature of the polymerisation and growth of the zirconium ion layer.

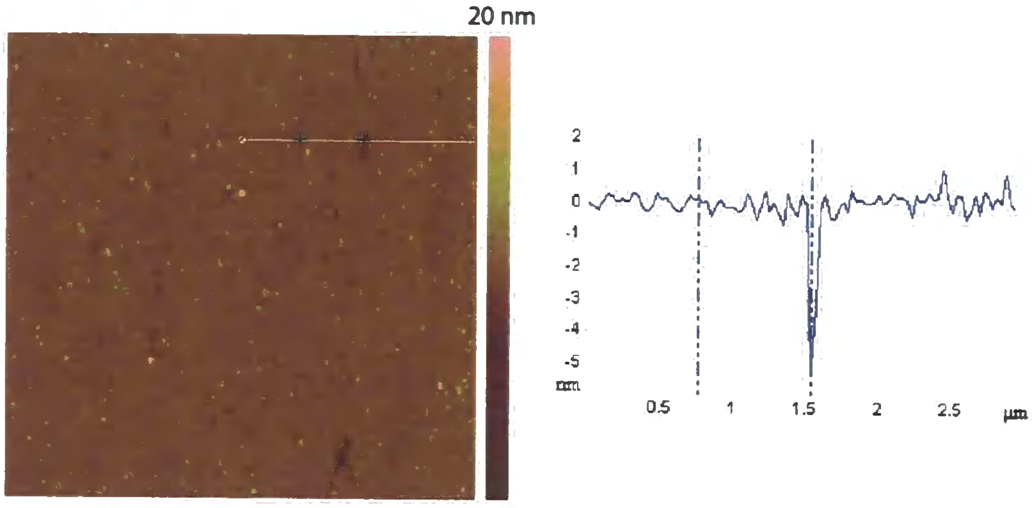

Figure 79. TappingMode™ AFM image (left) of 6 x 6 μm^2 region of Zr-ODP LB monolayer transferred from a 0.25 mM Ca^{2+} aqueous subphase surface to an ATPMS-modified Si/SiO_2 substrate, and a corresponding cross section of the film surface (right).

6.3 Nanopatterning of APTMS-supported LB films

AFM nanodisplacement patterning techniques previously described (see Chapter 5) provide a convenient route to creating spatially resolved patterns of amine functionality within the Zr-ODP LB film structure.

However, prior to nanodisplacement patterning, "capping" of the Zr-ODP surface (producing an ODP-Zr-ODP bilayer structure) was carried out through treatment of the deposited LB film surfaces in 1 mM solutions of ODP-H_2 prepared in ethanol. The high affinity of oxophilic Zr^{4+} ions towards the phosphonates was exploited, facilitating ODP monolayer film formation upon the Zr-ODP LB film surface. This additional surface modification step was carried out to provide greater chemical contrast between the LB film surface and the underlying amino-functionalised film which is exposed at the film-air interface in regions where AFM nanodisplacement patterning has been carried out. Enhancing the contrast of the physical properties between the deposited Zr-ODP LB film surface and the patterned amine regions is expected to aid selective binding of materials upon the patterned surface regions, as discussed later (see Section 6.4). Following ODP-H_2 solution treatment, AFM analysis showed little evidence of film capping however, with defect depths within the LB film layers remaining unchanged. In contrast to this though, static contact angle values were indicative of film capping having taken place with an increase in the hydrophobic character (96 ± 2 °) of the film surface observed (*c.f.* surface prior to capping showed static contact angle values of 75 ± 3 °). It is thought that the ODP "capping" of the Zr-ODP film surface leads to the formation of a highly disordered ODP monolayer, where the alkyl chains of the ODP molecules are lying with a high degree of tilt upon the LB film surface. For clarity the capped Zr-ODP films, will be referred to from here on as ODP-Zr-ODP LB films.

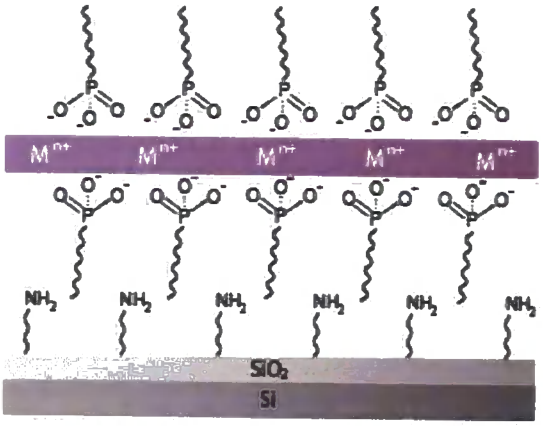

Figure 80. Cartoon representation of Zr-ODP LB monolayer, supported upon an APTMS-modified Si/SiO$_2$ substrate, following capping of the Zr-terminated surface with an ODP monolayer through solution treatment in a 1mM ODP-H$_2$ solution.

The nanodisplacement procedures used were similar to those employed previously with OTS-supported metal-ODP LB films, being carried out in contact mode AFM operation, using an AFM probe with a cantilever spring constant of 0.58 N/m or 0.32 N/m, and a Si$_3$N$_4$ tip. Calculation of the vertical forces applied upon the LB film surface were again calculated using Hookes Law (F = - k·x), with the cantilever displacement (*i.e.* cantilever deflection) determined using force curves.

Figure 81 shows an AFM image of a typical "grid" pattern produced by AFM nanodisplacement, exhibiting line widths of 210 nm creating an array of 1 x 1μm^2 ODP-Zr-ODP square domains. The shaved regions, produced by selective nanodisplacement of the LB layer, reveal the underlying aminosilane film surface (dark brown regions). The required patterning parameters for efficient nanodisplacement within the LB film proved consistent with those used in nanodisplacement studies of Zr-ODP LB films prepared upon OTS SAMs, with a vertical force threshold of *ca.* 40 nN calculated (*c.f.* vertical force threshold hold of *ca.*

40 nN required for patterning of Zr-ODP and Hf-ODP films upon OTS SAMs, see Sections 5.2.1 and 5.2.2).

The blue arrows on the AFM image in Figure 81 highlight material displaced from the LB layer during the patterning process which have subsequently redeposited around the periphery of the shaved features. The small amounts of material deposited around the patterned features suggests much of the displaced material transfers to the AFM tip, consistent with previous patterning of Zr-ODP films upon OTS SAM surfaces (see Section 5.2.1). The cross section profile of the image reveals the depth of the shaved patterns (4.8 ± 0.4 nm) to be consistent with that of the defects (4.9 ± 0.4 nm, see Figure 79) observed in the film structure, indicating the underlying aminosilane film is undisrupted by the nanodisplacement process.

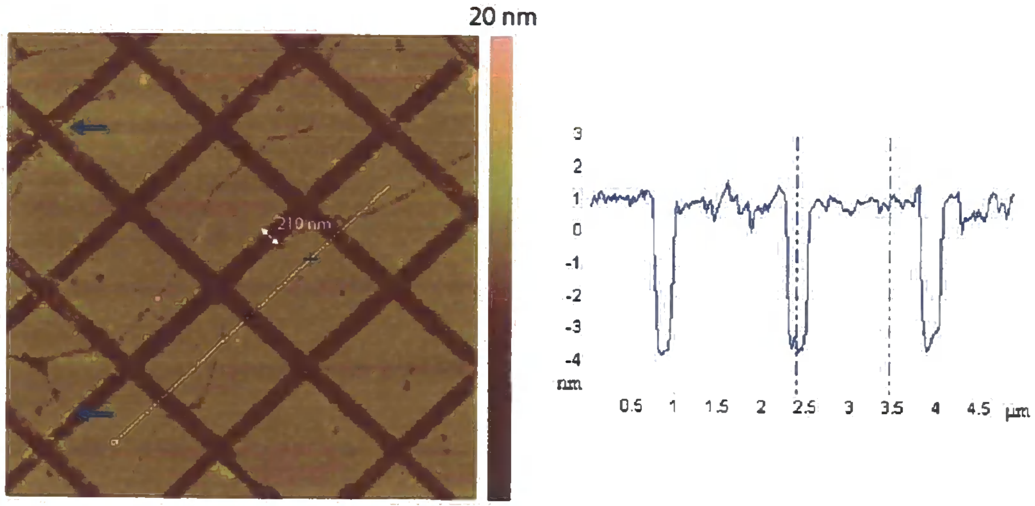

Figure 81. Contact mode AFM image (left) of 6 x 6 µm^2 region of a patterned ODP-Zr-ODP LB monolayer upon an APTMS-modified Si/SiO$_2$ substrate, with the blue arrows highlighting regions where the displaced LB film material from the patterning process has been redeposited on the film surface. The value on the image indicates the line widths of the patterns produced. A corresponding cross section profile of the film surface (right) is also shown.

Pattern resolutions achieved upon the APTMS/ODP-Zr-ODP film systems proved similar to those obtained with an OTS/metal-ODP systems, with line widths down to *ca.* 80 nm demonstrated. Figure 82 (left image) shows 6 x 6 μm^2 region of a grid network of 80 nm wide lines shaved into the Zr-ODP film, produced through passing the AFM probe over each pattern area a single time only. The second image in Figure 82 (right) shows the corresponding friction force image (with retrace image subtracted from the trace image to remove topographical contributions from the data) of the patterned LB film region, highlighting the chemical contrast between the shaved (exposed amine surface) and non-shaved film (Zr-ODP LB film surface) regions.

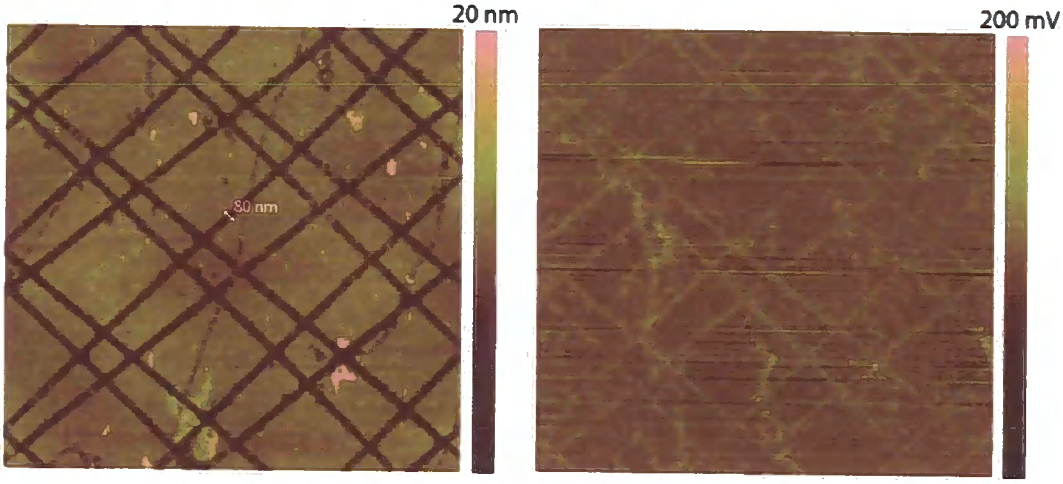

Figure 82. Contact mode AFM image (left) of a 6 x 6 μm^2 region of a patterned ODP-Zr-ODP LB monolayer upon an APTMS-modified Si/SiO$_2$ substrate. Resolutions of *ca.* 80 nm are demonstrated in the patterned features. The corresponding friction force image (right) highlights the compositional differences across from the film surface arising from the different frictional properties of the ODP-Zr-ODP LB film and underlying aminosilane film surface revealed in the patterned regions.

6.4 Amine template-directed binding of Au nanoparticles

The fabrication of chemically-modified substrates possessing alternative surface functionalities within spatially defined regions allows surfaces to be tailored for spatially resolved selective binding of desired materials. Here, efforts have focussed upon amine template-directed binding of citrate-stabilised AuNP (10 nm diameter) upon patterned the Zr-ODP LB/APTMS hybrid films. Au binding to amino-functionalised regions is a pH dependent process, taking place through electrostatic interactions between the negatively charged citrate ions upon the Au surface, and positively charged protonated amine groups,[287] Scheme 8.

Though XPS analysis confirms the presence of protonated quaternary amine groups at the APTMS SAM surface (see Section 6.2.1), AuNP treatment was carried out in solutions buffered to pH 4 to protonate any remaining free amine groups and maximise the positive charge character at the amine surface. Stock solutions of the Au colloids (*ca.* 0.01% $HAuCl_4$, *ca.* 0.75 A520 units/mL) were typically diluted with *ca.* x 37 volumes of H_2O prior to surface treatment (the use of higher concentrations of AuNP suspensions (x 0 - 2 water dilution) was found to commonly lead to indiscriminate binding of the nanoparticles across the patterned surfaces).

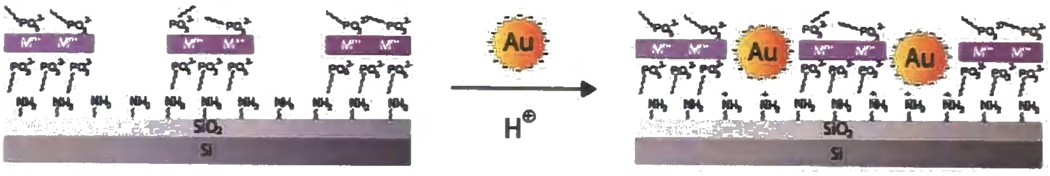

Scheme 8. Schematic showing selective binding of AuNPs in the patterned amine regions. Acidic suspensions (pH 4) of citrate-stabilised AuNPs leads to protonation of the amine groups enabling Au binding through electrostatic interactions between the positively charged ammonium groups and the negative charges on the Au surface (arising from the citrate species).

Some difficulty was encountered in consistently achieving successful deposition of the AuNPs, with them often being absent from the patterned surfaces (in both Zr-ODP and APTMS film regions) following treatment with the AuNP solutions. Failure of the AuNPs to bind to the APTMS surface regions is thought to be related to the availability of the amine groups at the aminosilane film surface. The disorder commonly exhibited in aminosilane films is well known, as discussed in Section 6.2.1, with potential interactions of the amine groups with the surface silanol groups of the Si/SiO_2 substrate (through hydrogen bond formation and $Si–O^- \, ^+H_3NR$ electrostatic interactions), leaving the amine orientated away from the film surface and towards to the substrate (as indicated by the peak at 401.8 eV in the N 1s XPS spectrum). Such orientations associated with the APTMS molecules will inhibit the availability of the amine groups to interact with other molecules in the environment above the aminosilane film surface. The morphology of the aminosilane film is strongly dependent upon the silanisation conditions such as concentration, solvent quality, temperature and reaction time.[268,288] It is subtle changes in the reaction conditions which are believed to influence the final aminosilane film structure which have resulted in the inconsistency of the AuNP binding process.

Figure 83 highlights two examples of successful template-directed binding of the AuNPs upon the patterned APTMS/ODP-Zr-ODP films, showing both before and after the AuNP solution treatment. The AFM images of the patterned film surface show high levels of selectivity to be exhibited in the Au binding process, taking place almost exclusively upon the exposed amino-functionalised surface regions. The ODP-Zr-ODP LB film regions are distinguished by an absence of AuNPs. The Au binding observed here is thought to be facilitated by the electrostatic interactions between the negative charges (from the citrate species) on the AuNP surfaces, and the positive charge of the protonated amines.[274]

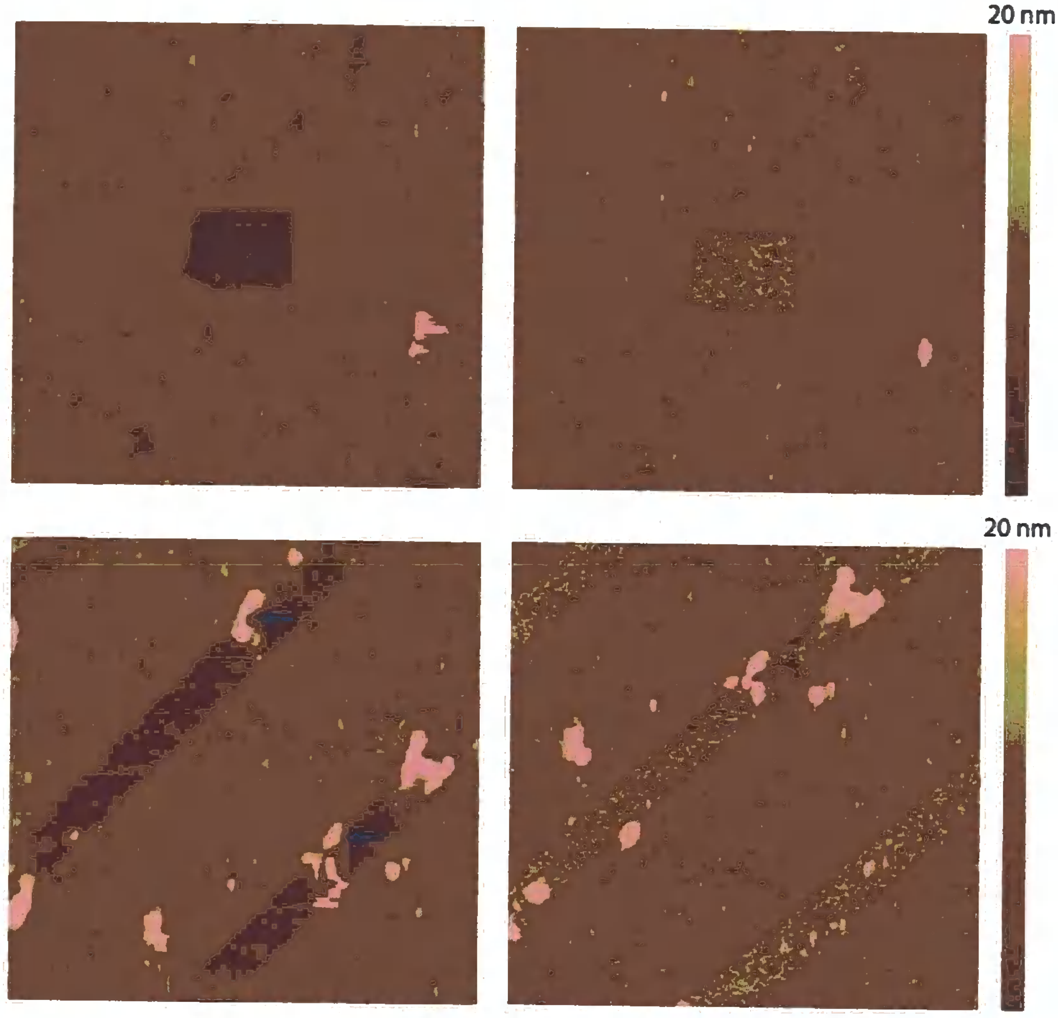

Figure 83. TappingMode™ AFM images showing two 6 x 6 μm² regions (left hand images) of a patterned ODP-Zr-ODP LB film (prepared upon a pure H_2O subphase) deposited upon an APTMS-modified Si/SiO_2 substrate. The blue arrows highlight regions in which the displaced LB film material from the nanodisplacement process have redeposited upon the film surface. The corresponding images (right hand side) show the patterned regions follow treatment in a buffered (pH 4) suspension of AuNPs (10 nm diameter), demonstrating the selective binding of the nanoparticles upon the amino-functionalised surface regions.

Evidence of significant protonation of the amine groups in the aminosilane film prior to LB deposition was previously confirmed by XPS (see Section 6.2.1). In addition, the pH control of the AuNP solution (pH 4) also ensures the presence of a positively charged amine surface.

6.5 Conclusions

The fabrication of patterned substrate surfaces containing spatially resolved surface regions of specific chemical functionality has been described through the preparation of metal-ODP LB films upon Si/SiO_2-supported aminosilane (APTMS) films. AFM nanodisplacement patterning of the LB layer has been demonstrated with nanoscale resolution (down to 80 nm line width) to reveal the underlying amine functionality in well-defined surface domains.

APTMS-modified Si/SiO_2 substrates were found to exhibit sufficient hydrophobic character (static contact angle values of $94 \pm 2\ ^{o}$ attributed to disorder in the film structure) to allow for "tail-down" LB deposition of metal-ODP films upon the amine surface. However, LB film quality onto such functionalised surfaces was found to be of lower quality than corresponding films deposited upon highly hydrophobic OTS SAM surfaces (static contact angle values of $106 \pm 3\ ^{o}$). This was thought to be due to the lower hydrophobic character of the aminosilane film surface. Subsequent improvements in the LB film quality were achieved through deposition of the ODP-H_2 LB monolayer from a Ca^{2+}-modified aqueous subphase. Association of the Ca^{2+} ions to the monolayer headgroups is thought to help stabilise the monolayer and increase the efficiency of the film transfer process.

The patterning processes of aminosilane-supported metal-ODP films proved consistent with that carried out upon OTS/metal-ODP film systems, with a vertical force threshold of *ca.* 40 nN required for efficient pattern formation.

Selective deposition of AuNPs within the patterned amino-functionalised surface regions has also been successfully shown, by simple solution treatments of the patterned surface in a citrate-stabilised AuNPs. By control of the pH of the AuNP solutions (pH 4), binding of the nanoparticles to the amine surface was facilitated through electrostatic interactions between the positively charged protonated amine groups at the exposed aminosilane surface regions, and the negatively charged AuNP (due to citrate species present at the Au surface).

The ability for selective binding of materials (*e.g.* AuNPs) upon such patterned surfaces highlights the potential of the methodology described here as a viable route towards the production of miniaturised technologies for use in biodiagnostics,[275,276] as well as in electronic[277,278] and photonic[279] devices.

Chapter 7

7. *Future work*

Much scope remains for the development of nanopatterned metal-stabilised LB films and ultra-thin metal oxide films based upon the fabrication techniques described here. Integration of these nanoscale systems into practical devices in particular, will pose significant challenges and be an important step forward in the progression of these surface modification techniques. Further characterisation of the ZrO_2 and HfO_2 produced for example (see Chapter 3), in particular investigating their electrical properties, will be important in evaluating their suitability as high dielectric materials for potential use in nanoelectronic devices (*e.g.* as gate oxides in metal oxide semiconductor field effect transistors).

The potential role of nanopatterned LB/SAM systems in the production of nanoscale devices has also been described, with template-directed binding of AuNPs upon amino-functionalised (SAM) surface domains confined within a LB film (see Chapter 6). Extension of these studies into the selective binding of alternative materials will broaden the potential range of applications of these surfaces. Amine template-controlled placement of proteins[289] and carbon nanotubes[290] for example, will offer potential use in biosensing technology[291] and nanoelectronic devices.[292]

Patterned OTS SAM-supported LB films (see Chapters 3 and 4), providing CH_3-terminated surface domains within the LB film structure, may also offer a route to selective binding of biomolecules and nanoparticles. The highly hydrophobic character associated with the OTS surfaces is proposed to hold significant promise in enabling selective adsorption of proteins containing hydrophobic regions at the exterior of their quaternary structure.

The extensive range of SAM chemistry, available upon a variety of different substrate supports (*e.g.* Au, SiO_2, SiH),[13] provides great potential in the fabrication of a range of different SAM/LB hybrid systems offering a range of alternative SAM surface functionalities (*e.g.* thiols,[293] aldehydes[294]). Of particular interest however, may be PO_3H_2-terminated SAM surfaces, which can be readily prepared through phosphorylation of Si/SiO_2-supported ATPMS SAMs.[295] Substrates exhibiting spatially-resolved PO_3H_2-functionalised surface domains, produced by deposition and nanodisplacement patterning of LB films upon phosphorylated aminosilane surfaces, are proposed to provide an indirect route to the formation of metal oxide nanostructures, Scheme 9a. This approach relies upon the high affinity of tetravalent metal ions such as Zr^{4+} and Hf^{4+} towards phosphonates to ensure selective binding of the metal species within the PO_3H_2-modified surface regions. This proposed methodology will provide significant challenges however, requiring an alternative means of LB film stabilisation to the use of metal species, to be devised.

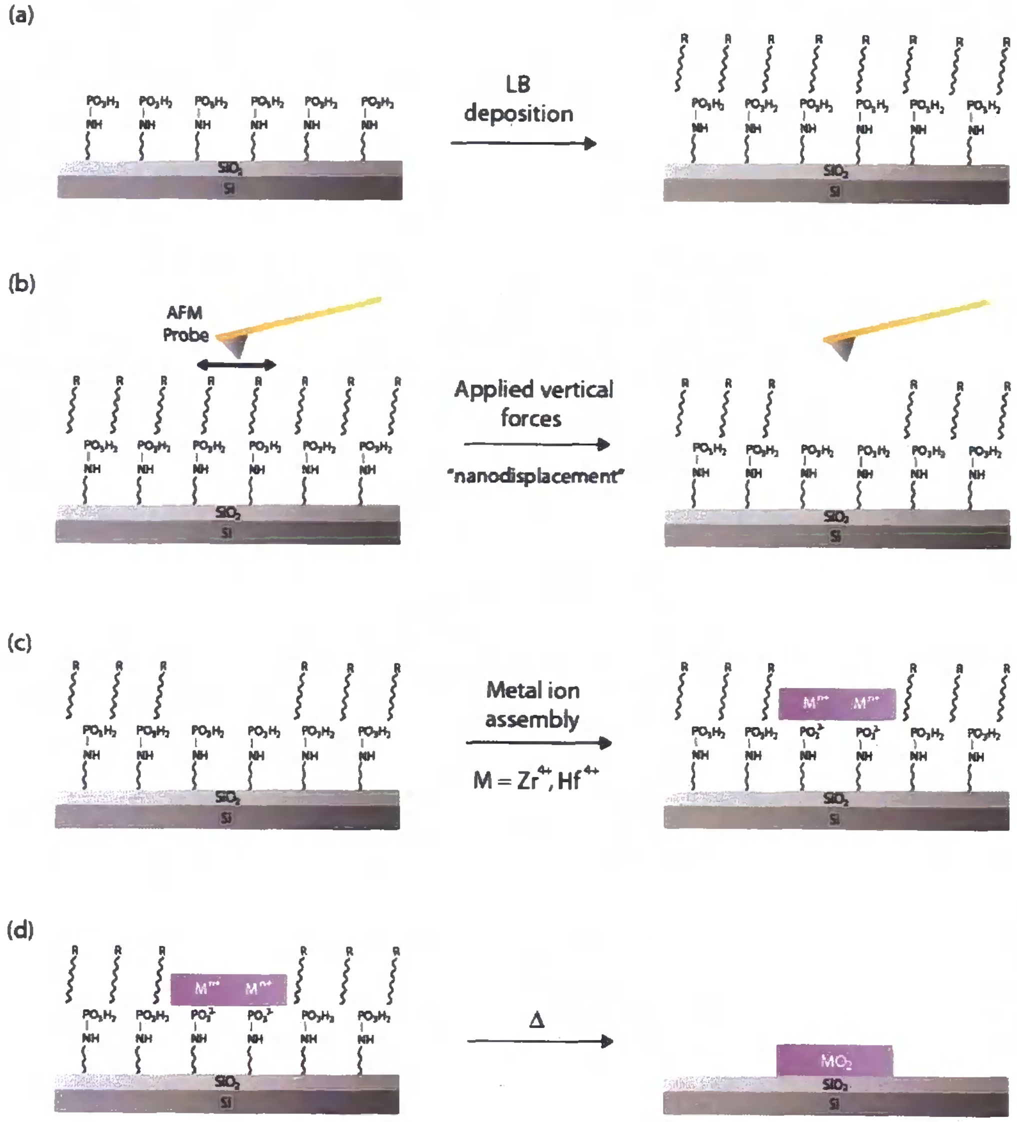

Scheme 9. Schematic representation of proposed route to two dimensional metal oxide nanostructures: (a) Deposition of a LB monolayer upon a PO_3H_2-terminated SAM surface, supported upon a Si/SiO_2 substrate. (b) Controlled application of high vertical forces upon film surface to selectively remove regions of the LB layer, revealing the underlying PO_3H_2 functionality. (c) Exposed PO_3H_2 surface regions "backfilled" through treatment in metal ion solutions. (d) High temperature treatment of surface leads to simultaneous decomposition of organic film components, and calcining of the metal ions to produced two dimensional metal oxide nanostructures.

Finally, the principles described here in the generation of (patterned) metal oxide films are not necessarily limited to application in top-down methodologies. An alternative bottom-up approach to the formation of two dimensional metal oxide nanostructures is suggested, using PO_3H_2-functionalised SAM surfaces in conjunction with dip-pen nanotechnology techniques, Scheme 10. This technique may provide a simple direct-write method for producing solid state nanostructures, without the added requirement of LB procedures.

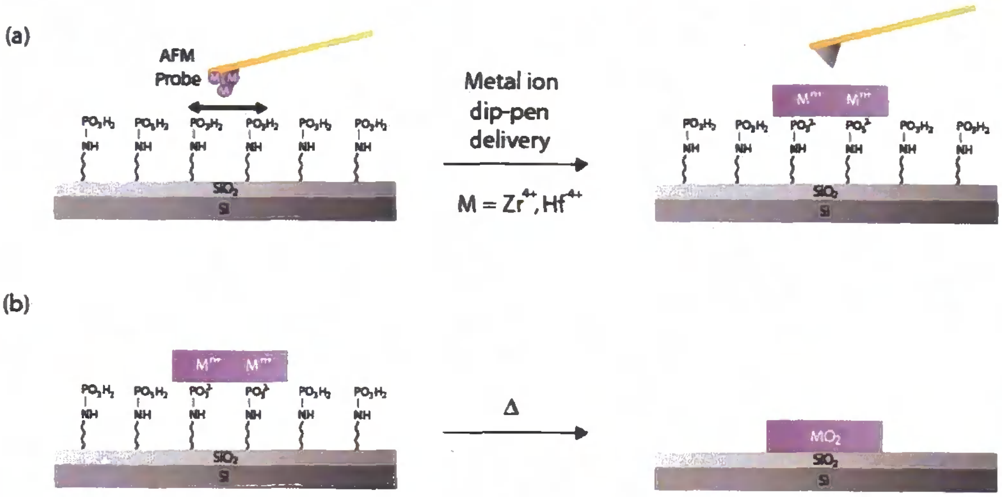

Scheme 10. Schematic representation of DPN methodology to preparation of metal oxide nanostructures: (a) Dip-pen delivery of metal ions from AFM probe to PO_3H_2-functionalised SAM surface. (b) High temperature treatment of surface leads to simultaneous decomposition of organic film components and calcining of metal ions, generating two dimensional metal oxide nanostructures.

Chapter 8

8. *Experimental*

8.1 *Materials*

All reagents were obtained from commercial sources and used as supplied. Octadecyltrichlorosilane (OTS, $C_{18}H_{37}SiCl_3$, 96 %), zirconyl (IV) chloride octahydrate ($ZrOCl_2.8H_2O$, 98%), sodium dodecylsulfate ($CH_3(CH_2)_{11}OSO_3Na$, 85 %), citric acid/sodium citrate/sodium hydroxide buffer solution (pH 4), and sodium borate/sodium hydroxide buffer solution (pH 10) were purchased from Acros Organics. 3-Aminopropyltrimethoxysilane (APTMS, $Si(OMe)_3C_3H_6NH_2$, 97%), hafnium (IV) oxychloride hydrate ($HfOCl_2 \cdot xH_2O$, x = 6 - 8, 98 %), magnesium nitrate hexahydrate ($Mg(NO_3)_2.6H_2O$, 99%), magnesium ethoxide ($Mg(OEt)_2$, 98 %), calcium chloride ($CaCl_2$, > 96%), and Au colloid solutions nanoparticles (*ca.* 0.01% $HAuCl_4$, *ca.* 0.75 A520 units/mL, 8.5 - 12.0 nm mean particle size) were purchased from Aldrich (Gillingham, UK). Octadecylphosphonic acid (ODP-H_2, $C_{18}H_{37}PO_3H_2$, 93+ %) was purchased from Alfa Aesar. Si/SiO_2 (111) wafers (100 mm diameter, 1.0182 - 2.2675 Ω cm resistivity; 500 - 550 μm) were purchased from Cemat Silicon S. A. (Warsaw, Poland). High purity water with a resistivity of 18 MΩ cm (Purite Neptune Purification System, Purite Ltd., Thame, UK) was used for all experiments.

8.2 *Silicon oxide silanisation*

8.2.1 Silicon oxide surface preparation

Prior to use, the silicon wafers were cut into *ca.* 1 x 1 cm^2 pieces using a tungsten-tipped cutting pen before sonication in acetone for 20 minutes, followed by rinsing with 18 MΩ cm purity water. They were then treated in piranha solution (3:1 H_2O_2/H_2SO_4; ***Warning:*** piranha solution should be handled with extreme caution, as it react violently with organic solvents with potential detonation risk) for 45 minutes at 80 °C, followed by thorough rinsing and storage in 18 MΩ cm purity water. Immediately prior to use, the Si/SiO_2 wafers were immersed in a 1:1 H_2O_2/HCl solution for 15 minutes at room temperature, followed by rinsing with copious amounts of 18 MΩ cm purity water and dried in air at 120 °C for *ca.* 20 minutes.

8.2.2 Octadecyltrichlorosilane self-assembled monolayer formation

Sample vials used for OTS monolayer preparation were cleaned in a detergent bath (5 % sodium dodecylsulfate solution in UHP water, at 70 °C) followed by thorough rinsing with 18 MΩ cm purity water, and oven dried (120 °C). Monolayer modification was carried out upon cleaned Si/SiO_2 wafers by immersion in a 1 mM OTS solution prepared in dry toluene, for 48 hours (the toluene was dried by being passed through a chromatography column filled with activated aluminium oxide). The OTS solutions were prepared under ambient conditions, and the sample vials sealed during the monolayer film formation upon the Si/SiO_2 wafer. Following monolayer formation, wafers were sonicated in two volumes of toluene, followed by two volumes of $CHCl_3$ for 10 minutes each (each volume *ca.* 15 cm^3), and given a final wash in 18 MΩ cm purity water.

8.2.3 3-Aminopropyltrimethoxysilane film formation

Sample vials used for APTMS film preparation were cleaned in a detergent bath (5 % sodium dodecylsulfate solution in 18 MΩ cm purity water, at 70 °C) followed by thorough rinsing with 18 MΩ cm purity water, and oven dried (120 °C). Clean Si/SiO_2 wafers were treated in 1 mM APTMS solutions, prepared in dry toluene, for 3 - 4 hours. APTMS solutions were made up under ambient conditions, and sample vials sealed during film formation. Following APTMS treatment, the modified Si/SiO_2 wafers were sonicated for x 2 volumes of $CHCl_3$, followed by x 2 volumes of hexane, for 10 minutes in each (each volume *ca.* 15 cm^3). Wafers were given a final wash in 18 MΩ cm purity water.

8.3 Langmuir-Blodgett deposition

8.3.1 Metal-octadecylphosphonate monolayers upon octadecyltrichlorosilane monolayers

8.3.1.1 Zirconium and hafnium-octadecylphosphonate

LB deposition of ODP-H_2 films upon OTS-modified Si/SiO_2 wafers was performed on a 611D Teflon-coated Langmuir dipping trough (Nima Instruments, Coventry, UK), equipped with a Teflon barrier, DL1 dipping mechanism and a Wilhelmy plate PS4 pressure sensor equipped with filter paper strips (1 x 2 cm^2) to measure the surface pressure. Single-barrier "pressure versus area" (π – A) isotherms were recorded using Nima Instruments Langmuir Trough software, version 5.16. 18 MΩ cm purity water was used for the subphase in the Langmuir trough. A glass sample vial was placed under the subphase in the well of the trough. ODP-H_2 was spread on the subphase surface, typically from 0.3 - 0.5 mg/ml $CHCl_3$ solutions, and left for 15 minutes to allow evaporation of the $CHCl_3$ solvent. The film was compressed at a rate of 40 cm^2/min to a target surface pressure of 20 mN/m *via* x 1.5 isotherm compression cycles. LB film transfer was achieved by passing the hydrophobic substrate downwards through the subphase-supported monolayer into the sample vial at a rate of 8 mm/min, whilst maintaining the target surface pressure. The remaining monolayer film upon the subphase was removed by vacuum suction, and the barrier fully opened. The sample vial containing the modified Si/SiO_2 wafer was removed from the trough and solutions of zirconyl chloride octahydrate or hafnium chloride hydrate added to the vial to a concentration of *ca.* 5 mM. The substrates remained immersed in the ionic metal solution for 1 hour. Prior to hafnium treatment, the hafnium chloride hydrate solutions were typically allowed to age for 48 hours. Zirconyl chloride solutions were aged for only 1 hour before use.

Following Zr/Hf treatment, the modified wafer was removed from the sample vial and washed thoroughly in two fresh volumes (*ca.* 15 cm^3 each) of 18 MΩ cm purity H_2O. Defective monolayer films of both Zr and Hf-ODP were prepared as described above, employing a reduced target surface pressure of 10 mN/m during LB deposition.

8.3.1.2 Magnesium-octadecylphosphonate

Monolayer films of Mg-ODP were prepared using the LB deposition procedures described in Section 8.3.1.1, with Mg^{2+} ions incorporated into the film, prior to substrate transfer, through use of a 0.5 mM $Mg(NO_3)_2$ aqueous subphase.

8.3.1.3 Magnesia-octadecylphosphonate

Monolayer films of magnesia-ODP were prepared as described in Section 8.3.1.1, using both 18 MΩ cm purity H_2O, and 0.5 mM $Mg(NO_3)_2$ aqueous subphases, with magnesia assembly carried out through treatment of the deposited film with a saturated $Mg(OEt)_2$ aqueous solution. The $Mg(OEt)_2$ solution was prepared at pH 10 using a 6 : 4 ratio of sodium borate buffer/18 MΩ cm purity water.

8.3.2 Metal-octadecylphosphonate bilayers upon octadecyltrichlorosilane self-assembled monolayers

8.3.2.1 Magnesium-octadecylphosphonate

LB deposition of ODP-Mg-ODP bilayer films upon OTS-modified Si/SiO_2 wafers was carried out by spreading of a 0.3 - 0.5 mg/ml $ODP\text{-}H_2$ solution, prepared in $CHCl_3$, upon a 0.5 mM $Mg(NO_3)_2$ aqueous subphase, and left for 15 minutes to allow evaporation of the $CHCl_3$ solvent. The film was compressed at a rate of 40 cm^2/min to a target surface pressure of 20 mN/m *via* x 1.5 isotherm compression cycles. LB film transfer was achieved by passing the hydrophobic substrate downwards through the subphase-supported monolayer, whilst maintaining the target surface pressure. Upon completion of the downstroke deposition, the substrate was vertically withdrawn from the subphase through the monolayer film to produce the bilayer film.

8.3.3 Metal-octadecylphosphonate multilayers upon octadecyltrichlorosilane self-assembled monolayers

8.3.3.1 Zirconium and hafnium-octadecylphosphonate

Following the formation of the Zr/Hf-ODP monolayers upon the OTS-modified Si/SiO_2 substrate as described in Section 8.3.1.1, subsequent layers of $ODP\text{-}H_2$ were deposited by vertical withdrawal of the substrate from an 18 MΩ cm H_2O subphase at a rate of 8 mm/min, with the supported monolayer maintained at a target surface pressure of 20 mN/m. This was followed by passing the now hydrophobic substrate back through the subphase-supported monolayer into a sample vial in the subphase. The substrate and vial were then removed from the trough and the appropriate zirconyl chloride octahydrate/hafnium chloride hydrate solution was added to the vial to a concentration of *ca.* 0.5 mM. The substrate remained immersed in the Zr^{4+}/Hf^{4+} solution for 1 hour after which time it was removed and washed thoroughly in two fresh volumes (*ca.* 15 cm^3 each) of high purity water. The process was then repeated for additional layers.

8.3.3.2 Magnesium-octadecylphosphonate

Multilayer Mg-ODP films were prepared using repeated LB bilayer depositions of ODP-H_2 from a 0.5mM $Mg(NO_3)_2$ aqueous subphase, as described in Section 8.3.2.1.

8.3.3.3 Magnesia-octadecylphosphonate

Multilayer films of magnesia-ODP were prepared using the LB deposition procedures described in Section 8.3.3.1, with ODP-H_2 monolayers formed upon an 0.5 mM $Mg(NO_3)_2$ aqueous subphase. Magnesia assembly was carried out using a saturated aqueous solution of $Mg(OEt)_2$, prepared at pH 10 as described in Section 8.3.1.3.

8.3.4 Metal-octadecylphosphonate monolayers upon 3-aminopropyltrimethoxysilane films

8.3.4.1 Zirconium-octadecylphosphonate

Deposition LB monolayers of ODP-H_2 upon APTMS-modified Si/SiO_2 wafers were carried out using both 18 MΩ cm H_2O and 0.25 mM $CaCl_2$ aqueous subphases. LB transfer of the ODP-H_2 monolayer to the substrate surface was carried out using the LB procedures described in Section 8.3.1.1 with the exception of the target surface pressure employed, using a value of 22 mN/m here. Following deposition, the LB monolayers were treated in a *ca.* 0.5 mM zirconyl chloride octahydrate solution for 1 hour, before washing in x 2 volumes (each *ca.* 15 cm^3) of 18 MΩ cm purity H_2O. Capping of the Zr-ODP surface was carried out through treatment of the modified Si/SiO_2 wafer in 1 mM ODP-H_2 solution prepared in EtOH for 1 hour, before removal and washing in x 1 volume of EtOH and x 1 volume H_2O (*ca.* 15 cm^3 each).

8.4 Metal oxide film formation

ZrO_2, HfO_2 and MgO films were prepared through thermal treatment of the corresponding metal-ODP LB films, prepared upon an OTS-modified Si/SiO_2 wafers, at 500 °C in air for *ca.* 16 hours in a furnace.

8.5 Au nanoparticle deposition.

250 μL^3 of the Au colloid stock solution was added to 9 mL of 18 MΩ cm purity H_2O, and 200 μL^3 of citric acid/sodium citrate/sodium hydroxide (pH 4) buffer. Following patterning of the ODP-Zr-ODP films prepared upon the APTMS-modified Si/SiO_2 wafers (see Section 8.4.2); the surfaces were treated in the diluted Au colloid solution for 90 minutes. The modified wafers were removed from the solution and briefly washed in 18 MΩ cm purity H_2O (*ca.* 15 cm^3).

8.6 Atomic force microscopy

8.6.1 Atomic force microscopy imaging

AFM imaging of OTS and APTMS-modified Si/SiO_2, and deposited LB monolayer and bilayer films was carried out in both contact and TappingMode^{TM} on a Multimode AFM equipped with a NanoscopeIV controller (Digital Instruments, Santa Barbara, CA, USA), and Nanoscope Version 6.12r1 software. Contact mode operation was carried out using sharpened silicon nitride tips (NPS) with a cantilever spring constant of 0.58 N/m or 0.32 N/m. (Veeco Instruments Ltd., Cambridge, UK). TappingMode^{TM} operation was carried out with either etched silicon probes (OTESPA), with a spring constant of 42 N/m (Veeco Instruments Ltd., Cambridge, UK), or etched silicon probes (Tap300) with a spring constant of 40 N/m (BudgetSensors, Windsor Scientific Ltd., Slough, UK). Contact mode images were recorded with the applied vertical forces minimised (< 5 nN), using 256 scan lines, and with the integral and proportional gains adjusted appropriately for optimised imaging. TappingModeTM images were acquired through adjustment of the setpoint amplitude, integral and proportional gains to appropriate values for optimum imaging, using 256 scan lines. Friction force images were recorded using in contact mode, employing a probe scanning angle of 90 °.

AFM data was processed using Nanoscope v6.12r1 software, with a first order flatten applied to the images. When necessary, glitches in the images (arising from unstable contact of the AFM probe upon the sample surface) were processed using a horizontal line erase.

8.6.2 Atomic force microscopy nanodisplacement patterning

Shaving, or nanodisplacement of the Zr/Hf/Mg-ODP LB monolayer films was carried out by contact mode AFM, using sharpened silicon nitride tips (NPS) with a cantilever spring constant of 0.32 N/m or 0.58 N/m, and tips with nominal radius of curvature of 20 nm (as stated by the manufacturer). Force curves generated and monitored with the Nanoscope 6.12r1 software were used to determine the applied vertical forces of the AFM probe tip upon the LB film surfaces, through monitoring the cantilever deflection. The spring constant values reported by the manufacturer (and which have not been normalised for tip radius) were used with the cantilever deflection in accordance with "Hookes Law" ($F = -k \cdot x$) to calculate a vertical force value.

Nanodisplacement within the LB films was typically carried out using scan rates of 10 - 12 Hz and with applied vertical forces above the film displacement threshold (as determined from the force curve measurements). Square pattern shapes were typically shaved into the films using an 1 : 1 aspect ratio, with scan areas ranging from 0 x 0 - 1 x 1 μm^2. High aspect ratio patterns were produced using aspect ratios ranging from "1 : 32" - "1 : 256", with patterns up to 20 µm in length, and 0, 45, and 90 ° scan angles employed. High aspect ratio patterns were also produced through the use of reduced number of scan lines (typically 16 or 32) over the scan region. Integral and proportional gains were typically set at values of 2.0 and 3.0 (below), respectively during all patterning experiments.

Imaging of shaved regions was typically carried out either the same contact probe, using force curves to again minimise the vertical forces (< 5 nN), and employing scan rates of *ca.* 1 Hz or below. Integral and proportional gains were appropriately varied to optimise the image quality. Further imaging in both contact and TappingMode^{TM}, using probes which have not been used in nanodisplacement procedures was often carried out.

8.7 X-ray photoelectron spectroscopy

X-ray photoelectron spectroscopy (XPS) was carried out using a Scienta ESCA 300 with an Al Kα X-ray source (1486.6 eV) at the National Centre for Electron Spectroscopy and Surface Analysis (NCESS), Daresbury Laboratory, UK. Take off angles of 10 ° and 45 ° were typically used for sample analysis. The modified silicon substrates were mounted on sample stubs with conductive carbon tape. All peaks were fitted with Gaussian-Lorentz peaks using in-house software to obtain peak area information. A linear base line was used in fitting processes.

8.8 Ellipsometry

Film thickness measurements were carried out using a SE 500 Model ellipsometer (Sentech Instruments GmbH, Berlin, Germany) employing an angle of incidence of 70° with a HeNe laser, λ = 632.8 nm, as the light source. Film thickness values were calculated from the n, ψ, and Δ using simulation software accompanying the SE 500. The refractive index, n, of the OTS were assumed as n =1.450.[51] Zr-ODP and Mg-ODP (containing Mg^{2+} and/or magnesia inorganic film components) and LB films were assumed to be n = 1.49 and n = 1.62 respectively, based upon literature values.[90,86] Hf-ODP films were assumed to have a same refractive index as the Zr-ODP films. The silicon oxide layer on the silicon wafers was measured prior to measurement of film thickness values, using an assumed refractive index of n = 1.460.

8.9 X-ray reflectometry

Thickness measurements of monolayers and multilayers on silicon wafers were carried out by X-ray reflectometry with a D5000 Diffractometer (Siemens, Germany) using a graphite monochromated Cu Kα, λ = 1.5418 Å, X-ray source. Data collection and processing was performed using software accompanying the D5000.

8.10 Specular reflectance fourier transform infra-red spectroscopy

Specular reflectance FTIR spectra were recorded with Nicole 860 FT-IR spectrometer, using a liquid nitrogen cooled HgCdTe detector. A Spec-Ac monolayer accessory was used for the specular reflectance experiments. All spectra consist of 512 scans at 4cm^{-1} resolution. Data acquisition and analysis was carried out using Omnic^{TM} v5.1 software, with baseline corrections and smoothing applied to the spectra.

8.11 Static contact angle measurements

Contact angle measurements were carried out at room temperature with a Rame-Hart (Mountain Lakes, New Jersey, USA) NRL Model 100-00 contact angle goniometer. A micropipette pipette was used to dispense 2 µl probe droplets of 18 MΩ cm purity purity water upon the sample surface.

8.12 Quartz crystal microbalance

Film mass measurements were made using a Model QCM 200 quartz crystal microbalance (Stanford Research Systems (SRS), Sunnyvale, California, USA) recorded over a period of 1 hour in air, using SRS software. Films were deposited upon 1 inch AT-cut quartz crystals (Testbourne Ltd., Hampshire, UK), with Au/Cr/Au/SiO_2 electrodes. Prior to use the quartz crystal was cleaned using piranha solution for 15 minutes (as described in Section 8.2.1). An OTS SAM was prepared upon the quartz crystal in a dry box, following the method described for Si/SiO_2 modification in Section 8.2.2. LB modification of the OTS-modified quartz crystal with a Zr-ODP monolayer film was was carried out using the method described in Section 8.3.1.1.

8.13 X-ray diffraction

A Bruker diffractometer operating at 40 kV and 40 mA was used to record the XRD data. The Bruker d8 Advance provides strictly $CuK_{\alpha1}$ radiation using a Ge(111) crystal monochromator. The X-rays pass through a fixed Soller slit and fixed 1 ° divergence slit. A Vantec linear Position Sensitive Detector (PSD) detected the diffracted intensity.

An Anton Paar HTK1200 furnace was used to conduct the high temperature XRD experiments on the d8, with samples heated from room temperature to a maximum temperature of 1473 K. The standard environment used to investigate the presence of phase transitions within materials was under air. The furnace is controlled by Brukers' XRD Commander software.

Appendix 1.

Specular reflectance FTIR spectrum of a Y-type multilayer LB film of seven repeat Hf-ODP bilayers, showing bands resolved at 2918cm^{-1} (asymmetric CH_3 stretch) and 2850 cm^{-1} (symmetric CH_2 stretch) and 2954 cm^{-1} (asymmetric CH_3 stretch).

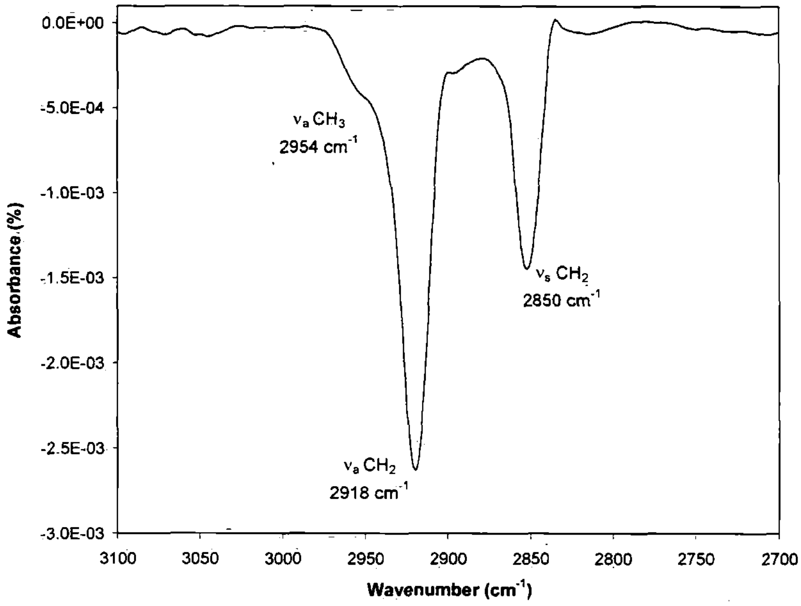

Appendix 2.

Specular reflectance FTIR spectrum of a Y-type multilayer LB film of seven repeat Mg-ODP bilayers, showing bands resolved at 2918cm^{-1} (asymmetric CH_3 stretch) and 2848 cm^{-1} (symmetric CH_2 stretch) and 2956 cm^{-1} (asymmetric CH_3 stretch).

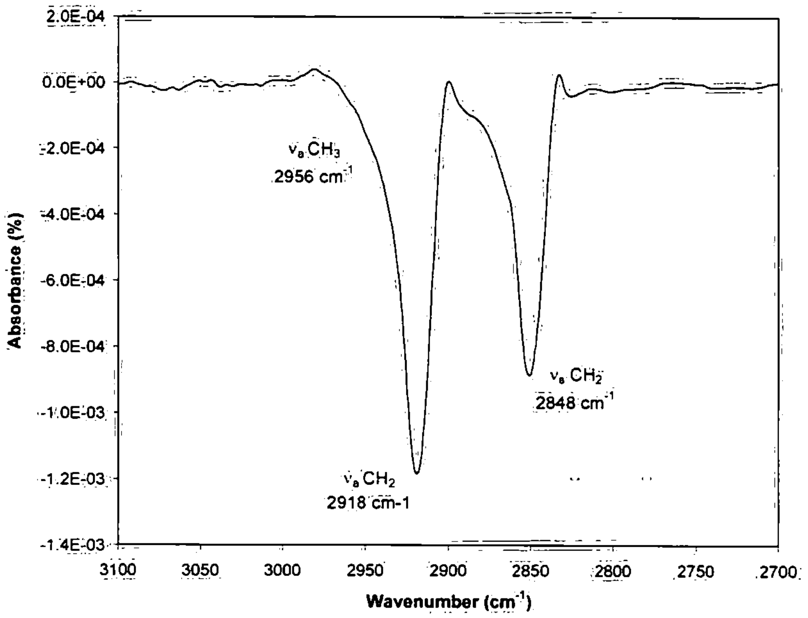

Appendix 3.

Specular reflectance FTIR spectrum of a Y-type multilayer LB film of seven repeat magnesia-ODP bilayers, showing bands resolved at 2958cm^{-1} (asymmetric CH_3 stretch) and 2850 cm^{-1} (symmetric CH_2 stretch) and 2918 cm^{-1} (asymmetric CH_2 stretch).

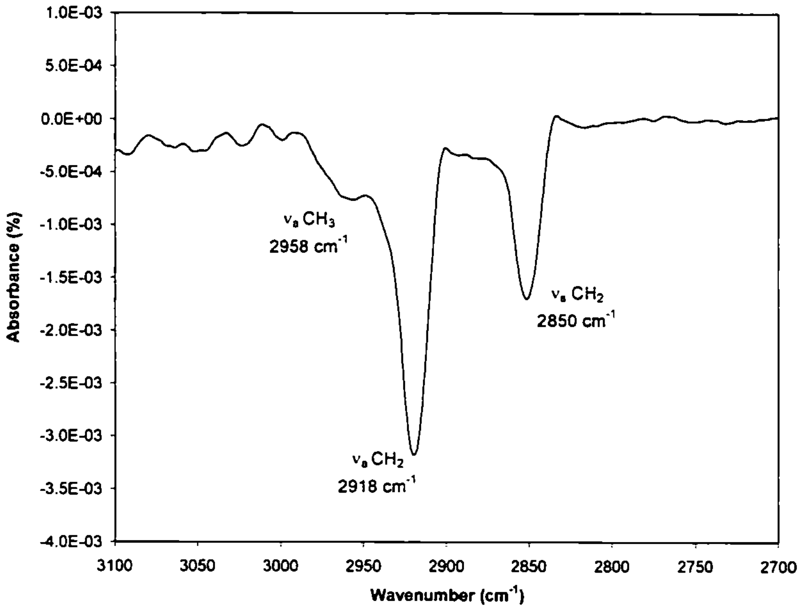

Appendix 4.

Specular reflectance FTIR spectrum of a Y-type multilayer LB film of seven repeat magnesia-ODP bilayers, prepared from a 0.5 mM Mg^{2+} subphase, showing bands resolved at 2956cm^{-1} (asymmetric CH_3 stretch) and 2850 cm^{-1} (symmetric CH_2 stretch) and 2918 cm^{-1} (asymmetric CH_3 stretch).

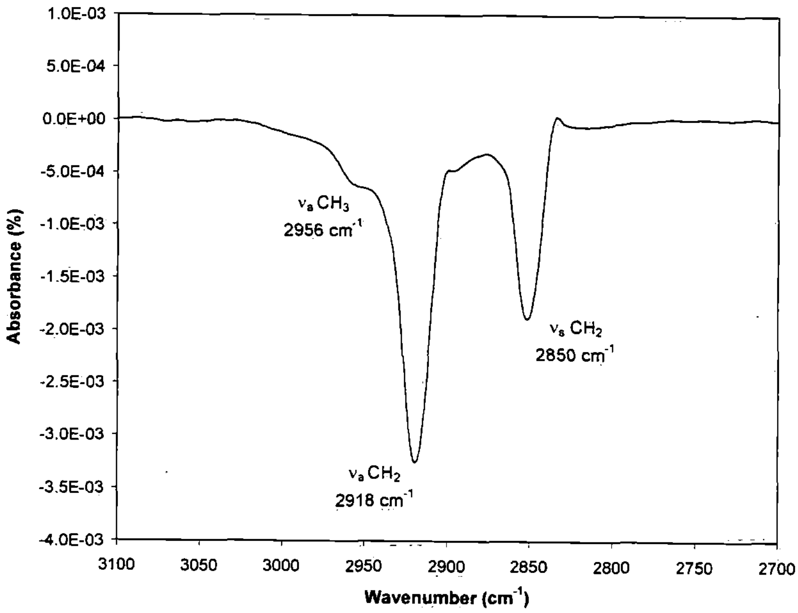

References

---

[1] Braun, E.; Eichen, Y.; Sivan, U.; Ben-Yoseph, G. *Nature*, **391**, 775 (1998)

[2] Ma, H.; Jen, A. K.-Y.; Dalton, L. R. *Adv. Mater.*, **14**, 1339 (2002)

[3] Pirrung, M. C. *Angew. Chem. Int. Ed.*, **41**, 1276 (2002)

[4] Schweitzer, B.; Predki, P.; Snyder, M. *Proteonomics*, **3**, 2190 (2003)

[5] Fazio, F.; Bryan, M. C.; Blixt, O.; Paulson, J. C.; Wong, C. -H. *J. Am. Chem. Soc*, **124**, 14397 (2002)

[6] Daniel, M. C.; Astruc, D. *Chem. Rev.*, **104**, 293 (2004)

[7] Li, G. T.; Bhosale, S.; Wang, T. Y.; Zhang, Y.; Zhu, H. S.; Fuhrhop, K. H. *Angew. Chem. Int. Ed.*, **42**, 3818 (2003)

[8] Xia, Y. N.; Yang, P. D.; Sun, Y. G.; Wu, Y. Y.; Mayers, B.; Gates, B.; Yin, Y. D.; Kim, F.; Yan, Y. Q. *Adv. Mater.*, **15**, 353 (2003)

[9] Iijima, S. *Nature*, **354**, 56 (1991)

[10] Schofield, W. C. E.; McGettrick, J.; Bradley, T. J.; Badyal, J. P. S.; Pryborski, S. *J. Am. Chem. Soc.*, **128**, 2280 (2006)

[11] Lee, K. -B.; Park, S. -J.; Mirkin, C. A.; Smith, J. C.; Mrksich, M. *Science*, **295**, 1702 (2002)

[12] Park, S.; Lee, M. R.; Pyo, S. J.; Shin, I. *J. Am. Chem. Soc.*, **126**, 4812 (2004)

[13] Ulman, A.; *Chem. Rev.*, **96**, 1533 (1990)

[14] Bigelow, W. C.; Pickett, D. L.; Zisman, W. A. *J. Colloid Interface Sci.*, **1**, 513 (1946)

[15] Allara, D. L.; Nuzzo, R. G. *Langmuir*, **1**, 45 (1985)

[16] Ogawa, H.; Chihera, T.; Taya, K. *J. Am. Chem. Soc.*, **107**, 1365 (1985)

[17] Schlotter, N. E.; Porter, M. D.; Bright, T. B.; Allara, D. L. *Chem. Phys. Lett.*, **132**, 93 (1986)

[18] Tao, Y. -T.; Lee, M. -T.; Chang, S. -C. *J. Am. Chem. Soc.*, **115**, 9547 (1993)

[19] Tao, Y. -T.; *J. Am. Chem. Soc.*, **115**, 4350 (1993)

[20] Woodward, J. T.; Ulman, A.; Schwartz, D. K. *Langmuir*, **12**, 3626 (1996)

[21] Hanson, E. L.; Schwartz, J.; Nickel, B.; Koch, N.; Danisman, M. F. *J. Am. Chem. Soc.*, **125**, 16074 (2003)

[22] Gawalt, E. S.; Avaltroni, M. J.; Koch, N.; Schwartz, J. *Langmuir*, **17**, 7536 (2001)

[23] Gao, W.; Dickinson, L.; Grozinger, C.; Morin, F. G.; Reven, L. *Langmuir*, **12**, 6429 (1996)

---

[24] Hoque, E.; DeRose, J. A.; Kulik, G.; Hoffmann, P.; Mathieu, H. J.; Bhushan, B. *J. Phys. Chem. B*, **110**, 10855 (2006)

[25] Neves, B. R. A.; Salmon, M. E; Russell, P. E.; Troughton, Jr., E. B. *Langmuir*, **17**, 8193 (2001)

[26] Silverman, B. M.; Wieghaus, K. A.; Schwartz, J. *Langmuir*, **21**, 225 (2005)

[27] McDermott, J. E.; McDowell, M.; Hill, I. G.; Hwang, J.; Kahn, A.; Bernasek, S. L.; Schwartz, J. *J. Phys. Chem. A*, **111**, 12333 (2007)

[28] Nuzzo, R. G.; Allara, D. L. *J. Am. Chem. Soc.*, **105**, 4481 (1983)

[29] Troughton, E. B.; Bain, C. D.; Whitesides, G. M; Allara, D. L.; Porter, M. D. *Langmuir*, **4**, 365 (1988)

[30] Sabatani, E.; Cohen-Boulakia, J.; Bruening, M.; Rubinstein, I. *Langmuir*, **9**, 2974 (1993)

[31] Bryant, M. A.; Joa, S. L.; Pemberton, J. E., *Langmuir*, **9**, 753 (1992)

[32] Hill, W.; Wehling, B. *J. Phys. Chem.*, **97**, 9451 (1993)

[33] Mielczarski, J. A.; Yoon, R. H. *Langmuir*, 7, 101 (1991)

[34] Uvdal, K.; Bodö, P.; Liedberg, B. *J. Colloid Interface.Sci.*, **149**, 162 (1992)

[35]Edwards, T. R. G.; Cunnane, V. J.; Parsons, R.; Gani, D. *J. Chem. Soc., Chem. Commun.*, 1041 (1989)

[36] Walczak, M. W.; Chung, C.; Stole, S.M; Widrig, C. A.; Porter, M. D. *J. Am. Chem. Soc.*, **113**, 2370 (1991)

[37] Nuzzo, R. G.; Zegarski, B. R.; Dubois, L. H. *J. Am. Chem. Soc.*, **109**, 733 (1987)

[38] Fenter, P.; Eberhardt, A.; Eisenberger, P. *Science*, **266**, 1216 (1994)

[39] Laibinis, P. E.; Whitesides, G. M.; Allara, D. L.; Tao, Y. -T.; Parikh, A. N.; Nuzzo, R. G. *J. Am. Chem. Soc.*, **113**, 7152 (1992)

[40] Laibinis, P. E.; Whitesides, G. M; *J. Am. Chem. Soc.*, **112**, 1990 (1992)

[41] Simazu, K.; Sato, Y.; Yagi, I.; Uosaki, K. *Bull. Chem. Soc. Jpn.*, **67**, 863 (1994)

[42] Stratmann, M. *Adv. Mater.*, **2**, 191 (1990)

[43] Netzer, L.; Iscovici, R.; Sagiv, R.; *J. Thin Solid Films*, **100**, 67 (1983)

[44] Brzoska, J. B.; Azouz, I. B.; Rondelez, F. *Langmuir*, **10**, 4367 (1994)

[45] Xiao, X.; Hu, J.; Charych, D. H.; Salmeron, M. *Langmuir*, **12**, 235 (1996)

[46] Kessell, C. R.; Granick, S. *Langmuir*, **7**, 532 (1991)

[47] Cohen, S. R.; Naaman, R.; Sagiv, J. *J. Phys. Chem.*, **90**, 3054 (1986)

[48] Biebaum, K.; Grunze, M.; Baski, A. A.; Chi, L. F.; Schrepp, W.; Fuchs, H. *Langmuir*, **11**, 2143 (1995)

---

[49] Wasserman, S. R.; Whitesides, G. M.; Tidswell, I. M.; Ocka, B. B.; Pershan, P. S.; Axe, J. D. *J. Am. Chem. Soc.*, **111**, 5852 (1989)

[50] Vallant, T.; Brummer, H.; Mayer, U.; Hoffman, H.; Leitner, T.; Resch, R.; Friedbacher, G. J. Phys. Chem. B, 102, 7190 (1998)

[51] Wasserman, S. R.; Tao, Y. -T.; Whitesides, G. M. *Langmuir*, **5**, 1074 (1989)

[52] Brandriss, S.; Margel, S. *Langmuir*, **9**, 1232 (1993)

[53] Silberzan, P.; Léger, L.; Ausserré, D.; Benattar, J. J. *Langmuir*, **7**, 1647 (1991)

[54] Angst, D. L.; Simmons, G. W. *Langmuir*, **7**, 2236 (1991)

[55] Tripp, C. P.; Hair, M. L. *Langmuir*, **11**, 149 (1995)

[56] Tripp, C. P.; Hair, M. L. *Langmuir*, **11**, 1215 (1995)

[57] Wang, Y.; Lieberman, M. *Langmuir*, **19**, 1159 (2003)

[58] McGovern, M. E.; Kallury, K. M. R.; Thompson, M. *Langmuir*, **10**, 3607 (1994)

[59] Parikh, A. N.; Allara, D. L. *J. Phys. Chem.*, **98**, 7577 (1994)

[60] Choi, S. -H.; Zhang Newby, B. -M. *Surf. Sci.*, **600**, 1391 (2006)

[61] Balasundaram, G.; Sato, M.; Webster, T. J. *Biomaterials*, **27**, 2798 (2006)

[62] Howarter, J. A; Youngblood, J. P. *Langmuir*, **22**, 11142 (2006)

[63] Golub, A. A.; Zubenko, A. I.; Zhmud, B. V.; *J. Colloid Interface Sci.*, **179**, 482 (1996)

[64] Fadeev, A. Y.; McCarthy, T. J. *Langmuir*, **16**, 7268 (2000)

[65] Horr, T. J.; Arora, P. S. *Colloids Surf. A*, **126**, 113 (1997)

[66] Vandenberg, E. T.; Bertilsson, L.; Liedberg, B.; Uvdal, K.; Erlandsson, R.; Elwing, H.; Lundstroem, I. *J. Colloid Interface Sci.*, **147**, 103 (1991)

[67] Brandriss, S.; Margel, S. *Langmuir*, **9**, 1232 (1993)

[68] Gun, J.; Sagiv, J. *J. Colloid Interface Sci.*, **112**, 457 (1986)

[69] Tillman, N.; Ulman, A.; Schildkraut, J. S.; Penner, T. L. *J. Am. Chem. Soc.*, **110**, 6136 (1988)

[70] Carson, G.; Granick, S. *J. App. Poly. Sci.*, **37**, 2767 (1989)

[71] Blodgett, K. B. *J. Am. Chem. Soc.*, **56**, 495 (1934)

[72] Blodgett, K. B. *J. Am. Chem. Soc.*, **57**, 1007 (1935)

[73] Petty, M. C. *Langmuir-Blodgett Films An Introduction*, Cambridge University Press, Cambridge (1996)

[74] Elbert, R.; Folda, T.; Ringsdorf, H. *J. Am. Chem. Soc.*, **106**, 7687 (1984)

[75] Vollhardt, D.; *J. Phys. Chem. C*, **111**, 6805 (2007)

---

[76] Marguerettaz, X.; Fitzmaurice, D. *Langmuir*, **13**, 6769 (1997)

[77] Peng, J. B.; Prakash, M.; MacDonald, R.; Dutta, P.; Ketterson, J. B. *Langmuir*, **3**, 1096 (1987)

[78] Peng, J. B.; Barnes, G. T; Gentle, I. R. *Adv. Coll. Inter. Sci.*, **91**, 163 (2001)

[79] Schwartz, D. K. *Surface Sci. Reports*, **27**, 241 (1997)

[80] Vogel, C.; Corset, J.; Dupeyrat, M. *J. Chim. Phys.*, **76**, 903 (1979)

[81] Amm, D. T.; Johnson, D. J.; Laursen, T.; Gupta, S. K. *Appl. Phys. Lett.*, **61**, 522 (1992)

[82] Ganguly, P.; Paranjape, D. V.; Sastry, M.; Chaudari, S. K.; Patil, K. R. *Langmuir*, **9**, 487 (1993)

[83] Zotova, T. V.; Arslanov, V. V.; Gagine, I. A. *Thin Solid Films*, **326**, 223 (1998)

[84] Silva, R. F.; Zaniquelli, M. E. D.; Serra, O. A.; Torriani, I. L.; de Castro, S. G. C. *Thin Solid Films*, **324**, 245 (1998)

[85] Seip, C. T.; Talham, D. R. *Mater. Res. Bull.*, **34**, 437 (1999)

[86] Seip, C. T.; Granroth, E. G.; Meisel, M. W.; Talham, D. R. *J. Am. Chem. Soc.*, **119**, 7084 (1997)

[87] Cao, G.; Lynch, V. M.; Swinnea, J. S.; Mallouk, T. E. *Inorg. Chem.*, **29**, 2112 (1990)

[88] Cao, G.; Lynch, V. M.; Yacullo, L. N.; *Chem. Mater.*, **5**, 1000 (1993)

[89] Fanucci, G. E.; Talham, D. R. *Langmuir*, **15**, 3289 (1999)

[90] Byrd, H.; Pike, J. K.; Talham, D. R. *Chem. Mater.* **5**, 709 (1993)

[91] Byrd, H.; Pike, J. K.; Talham, D. R. *J. Am. Chem. Soc.*, **116**, 7903 (1994)

[92] Clearfield, A.; Smith, G. D. *Inorg. Chem.*, **8**, 431 (1969)

[93] Culp, J. T.; Park, J. -H.; Benitez, I. O.; Huh, Y. -D.; Meisel, M. W.; Talham, D. R. *Chem. Mater.*, **15**, 3431 (2003)

[94] Smith, R. C.; Ma, T.; Hoilien, N.; Lancy, T. Y.; Bevan, M. J.; Colombo, L.; Roberts, J.; Campbell, S. A.; Gladfelter, W. L. *Adv. Mater. Opt. Electron.*, **10**, 105 (2000)

[95] Hausmann, D. M.; Kim, E.; Becker, J.; Gordon, R. G. *Chem. Mater.*, **14**, 4350 (2002)

[96] Atanassov, G.; Thielsch, R.; Popov, D. *Thin Solid Films*, **223**, 288 (1993)

[97] Bonnet, G.; Lachkar, M.; Larpin, J. P.; Colson, J. C. *Solid State Ionics*, **72**, 344 (1994)

[98] Choy, K. L. *Prog. Mater. Sci.*, **48**, 57 (2003)

[99] Leskelä, M.; Ritala, M. *Thin Solid Films*, **409**, 138 (2002)

[100] Jones, A. C.; Chalker, P. R. *J. Phys. D: Appl. Phys.*, **36**, R80 (2003)

[101] George, S. M.; Ott, A. W.; Klaus, J. W. *J. Phys. Chem.*, **100**, 13121 (1996)

[102] Bedja, I.; Hotchandani, S.; Kamat, P. V. *J. Phys. Chem.*, **98**, 4133 (1994)

[103] Moriguchi, I.; Maeda, H.; Teraoka, Y.; Kagawa, S. *J. Am. Chem. Soc.*, **117**, 1139 (1995)

---

[104] Niinistö, J.; Putkonen, M.; Niinistö, L. *Chem. Mater.*, **16**, 2953 (2004)

[105] Chang, J. P.; Lin, Y. S. *J. Appl. Phys.*, **90**, 2964 (2001)

[106] Gordon, R. G.; Becker, J.; Hausmann, D.; Suh, S. *Chem. Mater.*, **13**, 2463 (2001)

[107] Zhao, Z. W.; Tay, B. K.; Huang, L.; Yu, G. Q. *J. Phys. D: Appl. Phys.*, **37**, 1701 (2004)

[108] Khawaja, E. E.; Bouamrane, F.; Hallak, A. B.; Daous, M. A.; Salim, A. M. *J. Vac. Sci. Technol. A*, **11**, 580 (1993)

[109] Ehrhart, G.; Capoen, B.; Robbe, O.; Boy, Ph.; Turrell, S.; Bouazaoui, M. *Thin Solid Films*, **496**, 227 (2001)

[110] Ben Amor, S.; Rogier, B.; Baud, G.; Jacquet, M.; Nardin, M. *Mater. Sci. Eng. B*, **57**, 28 (1998)

[111] Matsuura, N.; Johnson, D. J.; Amm, D. T. *Thin Solid Films*, **295**, 260 (1997)

[112] Kalachev, A. A.; Mathauer, K.; Höhne, U.; Möhwald, H.; Wegner, G. *Thin Solid Films*, **228**, 307 (1993)

[113] Mirley, C. L.; Koberstein, J. T. *Langmuir*, **11**, 1049 (1995)

[114] Mirley, C. L.; Koberstein, J. T. *Langmuir*, **11**, 2837 (1995)

[115] Gang, Z.; Kun, F.; Pingsheng, Haizeng, S. *J. Mater. Chem.*, **12**, 2998 (2002)

[116] Brandl, D.; Schoppmann, C.; Tomaschko, C.; Markl, J.; Vost, H. *Thin Solid Films*, **249**, 113 (1994)

[117] Amm, D. T.; Johnson, D. J.; Matsuura, N.; Laursen, T.; Palmer, G. *Thin Solid Films*, **242**, 74 (1994)

[118] Taylor, D. M.; Lambi, J. N. *Thin Solid Films*, **243**, 384 (1994)

[119] Tippmann-Krayer, P.; Mohwald, H.; Schreck, M.; Gopel, W. *Thin Solid Films*, **213**, 136 (1992)

[120] Xia, Y.; Whitesides, G. M. *Angew. Chem. Int. Ed.*, **37**, 550 (1998)

[121] Bai, P.; *IEDM Tech. Dig.*, 197 (2004)

[122] Yasin, S.; Hasko, D. G.; Ahmed, H. *Appl. Phys. Lett.*, **78**, 2760 (2001)

[123] Bain, C. D.; Whitesides, G. M. *Science*, **240**, 62 (1988)

[124] Jeon, N. L.; Finnie, K.; Branshaw, K.; Nuzzo, R. G. *Langmuir*, **13**, 3382 (1997)

[125] Kumar, A.; Biebuyck, H. A.; Whitesides, G. M. *Langmuir*, **10**, 1498 (1994)

[126] Yu, M.; Lin, J.; Wang, Z.; Fu, J.; Wang, S.; Zhang, H. J.; Han, Y. C. *Chem. Mater.*, **14**, 2224 (2002)

[127] Seraji, S.; Wu, Y.; Jewell-Larson, E.; Forbess, M. J.; Limmer, S. J.; Chou, T. P.; Cao, G. *Adv. Mater.*, **12**, 1421 (2000)

[128] Kim, E.; Xia, Y.; Whitesides, G. M. *Nature*, **376**, 581 (1995)

[129] Yan, X.; Yao, J.; Lu, G.; Chen, X.; Zhang, K.; Yang, B. *J. Am. Chem. Soc.*, **126**, 10510 (2004)

[130] Kumar, A.; Whitesides, G. M. *Appl. Phys. Lett.*, **62**, 2002 (1994)

---

[131] Delamarche, E.; Geissler, M.; Wolf, H.; Michel, B. *J. Am. Chem. Soc.*, **124**, 3834 (2001)

[132] Xia, Y.; Kim, E.; Zhao, X. -M.; Rogers, J. A.; Prentiss, M.; Whitesides, G. M. *Science*, **273**, 347 (1996)

[133] Zhao, X. -M.; Xia, Y.; Whitesides, G. M. *Adv. Mater.*, **8**, 837 (1996)

[134] Kim, E.; Xia, Y.; Zhao, X. -M.; Whitesides, G. M. *Adv. Mater.*, **9**, 651 (1997)

[135] Geissler, M.; Wolf, H.; Stutz, R.; Delamarche, E.; Grummt, U. -W.; Michel, B.; Bietsch, A. *Langmuir*, **19**, 6301 (2003)

[136] Guo, L. J. *Adv. Mater.*, **19**, 495 (2007)

[137] Chou, S. Y *Science* 272, 85 (1996)

[138] Gates, B. D.; Xu, Q.; Stewart, M.; Ryan, D.; Wilson, C. G.; Whitesides, G. M. *Chem. Rev.*, **105**, 1171 (2005)

[139] Krämer, S.; Fuirer, R. R.; Gorman, C. B. *Chem. Rev.*, **103**, 4367 (2003)

[140] Binnig, G.; Rohrer, H.; Gerber, C.; Weibel, E. *Appl. Phy Lett.* **40**, 178 (1982)

[141] Camillone III, N.; Eisenberger, P.; Leung, T. Y. B.; Schwartz, P.; Scoles, G.; Poirier, G. E.; Tarlov, M. J. *J. Chem. Phys.*, **101**, 11031 (1994)

[142] Duerig, U.; Zueger, O.; Michel, B.; Haeussling, L.; Ringsdorf, H. *Phys. Rev. B*, **48**, 1711 (1993)

[143] Lercel, M. J.; Redinbo, G. F.; Craighead, H. G.; Sheen, C. W.; Allara, D. L. *Appl. Phys. Lett.*, **65**, 974 (1994)

[144] Kim, Y. T.; Bard, J. A. *Langmuir*, **8**, 1096 (1992)

[145] Sugimura, H.; Nakagiri, N. *Langmuir*, **11**, 3623 (1995)

[146] Schoer, J. K.; Zamborini, F. P.; Crooks, R. M. *J. Phys. Chem.*, **100**, 11086 (1996)

[147] Schoer, J. K.; Crooks, R. M. *Langmuir*, **13**, 2323, (1997)

[148] Schoer, J. K.; Ross, C. B.; Crooks, R. M.; Corbitt, T. S.; Hampden-Smith, M. J. *Langmuir*, **10**, 615 (1994)

[149] Gorman, C.B.; Carroll, R. L.; He, Y.; Tian, F.; Fuierer, R. *Langmuir*, **16**, 6312, (2000)

[150] Day, H. C.; Allee, D. R. *Appl. Phys. Lett.*, **62**, 2691 (1993)

[151] Sugimura, H.; Okiguchi, K.; Nakagiri, N.; Miyashita, M. *J. Vac. Sci. Technol., B*, **14**, 4140 (1996)

[152] Zhao, J. W.; Uosaki, K. *Langmuir*, **17**, 7784 (2001)

[153] Ara, M.; Graaf, H.; Tada, H. *Appl. Phys. Lett.*, **80**, 2565 (2002)

[154] Lee, H.; Kim, S. A.; Ahn, S. J.; Lee, H. *Appl. Phys. Lett.*, **81**, 138 (2002)

---

[155] Tully, D. C.; Trimble, A. R.; Fréchet, J. M. J.; Wilder, K.; Quate, C. F. *Chem. Mater.*, **11**, 2892 (1999)

[156] Tully, D. C.; Wilder, K.; Fréchet, J. M. J.; Trimble, A. R.; Quate, C. F. *Adv. Mater.*, **11**, 314 (1999)

[157] Sugimura, H.; Nakagiri, N. *J. Am. Chem. Soc.*, **119**, 9226 (1997)

[158] Zheng, J. W.; Zhu, Z. H.; Chen, H. F.; Liu, Z. F. *Langmuir*, **16**, 4409 (2000)

[159] Maoz, R.; Cohen, S.; Sagiv, J. *Adv. Mater.*, **11**, 55 (1999)

[160] Pavlovic, E.; Oscarsson, S.; Quist, A. P; *Nano Lett.*, **3**, 779 (2003)

[161] Fresco, A. M.; Fréchet, J. M. J. *J. Am. Chem. Soc.*, **127**, 8303 (2005)

[162] Backer, S. A.; Suez, I.; Fresco, Z. M.; Rolandi, M.; Fréchet, J. M. J. *Langmuir*, **23**, 2297 (2007)

[163] Liu, G.; Salmeron, M. B. *Langmuir*, **10**, 367 (1994)

[164] Kelley, S. O.; Barton, J. K.; Jackson, N. M.; McPherson, L. D.; Potter, A. B.; Spain, E. M.; Allen, M. J.; Hill, M. G. *Langmuir*, **14**, 6781 (1998)

[165] Zhao, J. W.; Sinniah, K.; Abell, C.; Rayment, T. *Langmuir*, **18**, 8278 (2002)

[166] Xiao, X. D.; Liu, G. Y.; Charych, D. H.; Salmeron, M. *Langmuir*, **11**, 1600 (1995)

[167] Headrick, J. E.; Armstrong, M.; Cratty, J.; Hammond, S.; Sheriff, B. A.; Berrie, C. L. *Langmuir*, **21**, 4117 (2005)

[168] Xu, S.; Liu, G. *Langmuir*, **13**, 127 (1997)

[169] Wadu-Mesthridge, K.; Xu, S.; Amro, N. A.; Liu, G. Y. *Langmuir*, **15**, 8580 (1999)

[170] Kenseth, J. R.; Harnisch, J. A.; Jones, V. W.; Porter, M. D. *Langmuir*, **17**, 4105 (2001)

[171] Amro, N.A.; Xu, S.; Liu, G. *Langmuir*, **16**, 3006 (2000)

[172] Piner, R. D.; Zhu, J.; Xu, F.; Hong, S.; Mirkin, C. A. *Science*, **283**, 661 (1999)

[173] Ewing, A. C.; *The Fountain Pen: A Collector's Companion*, RunningPress, Philadelphia, PA (1997)

[174] Ginger, D. S.; Zhang, H.; Mirkin, C. A. *Angew. Chem. Int. Ed.*, **43**, 30 (2004)

[175] Rozhok, S.; Piner, R.; Mirkin, C. A *J. Phys. Chem. B*, **107**, 751 (2003)

[176] Weeks, B. L.; Noy, A.; Miller, A. E.; De Yoreo, J. J. *Phys. Rev. Lett.*, **88**, 255505 (2002)

[177] Sheehan, P. E.; Whitman, L. J. *Phys. Rev. Lett.*, **88**, 156104 (2002)

[178] Ivanisevic, A.; Mirkin, C. A. *J. Am. Chem. Soc.*, **123**, 7887 (2001)

[179] Jung, H.; Kulkarni, R.; Collier, C. P. *J. Am. Chem. Soc.*, **125**, 12096 (2003)

[180] Pena, D. J.; Raphael, M. P.; Byers, J. M. *Langmuir*, **19**, 9028 (2003)

[181] Noy, A.; Miller, A. E.; Klare, J. E.; Weeks, B. L.; Woods, B. W.; De Yoreo, J.J. *Nano Lett.*, **2**, 109 (2002)

---

[182] Maynor, W. B.; Filocamo, S. F.; Grinstaff, M. W.; Liu, J. *J. Am. Chem. Soc.*, **124**, 522 (2002)

[183] Ben Ali, M.; Ondarçuhu, Brust, M.; Joachim, C. *Langmuir*, **18**, 872 (2002)

[184] Wilson, D. L.; Martin, R.; Hong, S.; Cronin-Golomb, M.; Mirkin, C. A.; Kaplan, D. L. *Proc. Natl. Acad. Sci. U. S. A.*, **98**, 13660 (2001)

[185] Lee, K. B.; Lim, J. H.; Mirkin, C. A. *J. Am. Chem. Soc.*, **125**, 5588 (2003)

[186] Agarwal, G.; Sowards, L. A.; Naik, R. R.; Stone, O. *J. Am. Chem. Soc.*, **124**, 580 (2003)

[187] Demers, L. M.; Ginger, D. S.; Park, S. J.; Li, Z.; Chung, S. W.; Mirkin, C. A. *Science*, **296**, 1836 (2002)

[188] Su, M.; Liu, X.; Li, S -Y.; Dravid, V. P.; Mirkin, C. A. *J. Am. Chem. Soc.*, **124**, 1560 (2002)

[189] Fu, L.; Liu, X.; Zhang, Y.; Dravid, V. P.; Mirkin, C. A. *Nano Lett.*, **3**, 757 (2003)

[190] Davis, J. J.; Coleman, K. S.; Busuttil, L.; Bagshaw, C. B. *J. Am. Chem. Soc.*, **127**, 13082 (2005)

[191] Sun, S.; Chong, K. S. L.; Leggett, G. J. *J. Am. Chem. Soc.*, **124**, 2414 (2002)

[192] Sun, S. Q.; Leggett, G. J. *Nano Lett.*, **2**, 1223 (2002)

[193] Sun, S.; Montague, M.; Critchley, K.; Chen, M -S.; Dressick, W. J.; Evans, S. D.; Leggett, G. J.; *Nano Lett.*, **6**, 29 (2006)

[194] Langmuir, I. *Trans. Faraday Soc.*, **15**, 62 (1920)

[195] Martin, R.; Szablewski, M. *Tensiometers and Langmuir-Blodgett Troughs Operating Manual 4th Edition*; Nima Technology Ltd. (1998)

[196] Peng, J. B.; Barnes, G. T; Gentle, I. R. *Adv. Coll. Inter. Sci.*, **91**, 163 (2001)

[197] Yazdanian, M.; Yu, H.; Zografi, G. *Langmuir*, **6**, 1093 (1990)

[198] Binnig, G.; Quate, C. F.; Gerber, C. *Phys. Rev. Lett.*, **56**, 930 (1986)

[199] Zhong, Q.; Innis, D.; Kjoller, K.; Elings, V. B. *Surf. Sci. Lett.*, **290**, L688 (1993).

[200] Atkins, P. W. *Physical Chemistry 6th Edition*, Oxford University Press, Oxford (1998)

[201] Cameron, M. A.; George, S. M. *Thin Solid Films*, **348**, 90 (1999).

[202] Wang, J.; Li, H.-P.; Stevens, R. *J. Mater. Sci.*, **27**, 5397 (1992)

[203] Wallace, R. M.; Wilk, G. D. *Crit. Rev. Solid State Mater. Sci.*, **28**, 231 (2003)

[204] Kingon, A. I; Maria, J-P.; Streiffer, S. K. *Nature*, **406**, 1032. (2000)

[205] Copel, M.; Gribelyuk, M.; Gusev, E. *App. Phys. Lett.*, **76**, 436 (2000)

[206] Cassir, M.; Goubin, F.; Bernay, C.; Vernoux, P.; Lincot, D. *Appl. Surf. Sci.*, **193**, 120 (2002)

[207] Wang, Y.; Lieberman, M. *Langmuir*, **19**, 1159 (2003)

[208] Brandriss, S.; Margel, S. *Langmuir*, **9**, 1232 (1993)

---

[209] Stevens, M. J. *Langmuir*, **15**, 2773 (1999)

[210] Dines, M. B.; DiGiacomo, P. M. *Inorg. Chem.*, **20**, 92 (1981)

[211] C. M. Kozák, P. Mountford, Encyclopedia of Inorganic Chemistry, (http://mrw.interscience.wiley.com/emrw/9780470862100/eic/article/ia263/current/abstract)

[212] Devia, D. H.; Sykes, A. G. *Inorg. Chem.*, **20**, 910 (1981).

[213] Singhal, A.; Toth, L. M.; Lin, J. S.; Affholter, K. *J. Am. Chem. Soc.*, **118**, 11529 (1996)

[214] Ohtsuka, K.; Hayashi, Y.; Suda, M. *Chem. Mater.*, **5**, 1823 (1993)

[215] He, G.; Liu, M.; Zhu, L.Q.; Chang, M.; Fang, Q.; Zhang, L.D. *Surf. Sci.*, **576**, 67-75 (2005)

[216] Porter, M. D.; Bright, T. B.; Allara, D. L.; Chidsey, C. E. D. *J. Am. Chem. Soc.*, **109**, 3559 (1987)

[217] Kim, H. K.; Lee, J. P.; Park, C. R.; Kwak, H. T.; Sung, M. M. *J. Phys. Chem. B*, **107**, 4348 (2003)

[218] McElwee, J.; Helmy, R.; Fadeev, A. Y. *J. Colloid Interface Sci.*, **285**, 551 (2005)

[219] Sinha, S.; Badrinarayanan, S.; Sinha, A. P. B. *J.Less-common Metals*, **125**, 85 (1986)

[220] Morant, C.; Galan, L.; Sanz, J. M. *Surf. Interface Anal.*, **16**, 304 (1990)

[221] ICSD ref: 17-0923

[222] ICSD ref: 37-1484

[223] Hann, R. E.; Suitch, P. R.; Pentecost, J. L. *J. Am. Ceramic Soc.*, **68**, 285 (1985)

[224] Ruh, R.; Corfield, P. W. R. *J. Am. Ceramic Soc.*, **53**, 126 (1970)

[225] Matwiyoff, N. A.; Taube, H., *J. Am. Chem. Soc.*, **90**, 2796 (1968)

[226] Byrd, H.; Pike, J. K.; Talham, D. R. *Thin Solid Films*, **242**, 100 (1994)

[227] Culp, J. T.; Davidson, M.; Duran, R. S.; Talham, D. R. *Langmuir*, **18**, 8260 (2002)

[228] Fanucci, G. E.; Seip, C. T.; Petruska, M. A.; Nixon, C. M.; Ravaine, S.; Talham, D. R. *Thin Solid Films*, **327**, 331 (1998)

[229] Cao, G.; Lynch, V. M.; Swinnea, J. S.; Mallouk, T. E. *Inorg. Chem.*, **29**, 2112 (1990)

[230] Gibaud, A.; Hazra, S. *Curr. Sci.*, **78**, 1467 (2000)

[231] Inoue, Y.; Yasmori, I. *Bull. Chem. Soc. Jpn.* **54**, 1505 (1981)

[232] Nefedov, V. I.; Firsov, M. N.; Shaplygin, I. S. *J. Electron Spectrosc. Relat. Phenom.*, **26**, 65 (1982)

[233] Sasaki, S.; Fujino, K.; Takeuchi, Y. *Proc. Jpn. Acad.*, **55**, 43 (1979)

[234] Taylor, D. M.; Lambi, J. N. *Thin Solid Films*, **243**, 384 (1994)

[235] Tippmann-Krayer, P.; Mohwald, H.; Schreck, M.; Gopel, W. *Thin Solid Films*, **213**, 136 (1992)

[236] Brinker, C. J. ; Scherer, G. W.; *Sol-Gel Science*; Academic Press, New York (1990)

[237] Wen, J.; Wilkes, G. L. *Chem. Mater.*, **8**, 1667 (1996)

---

[238] Avnir, D. *Acc. Chem. Res.*, **28**, 328 (1995)

[239] Elings, J. A.; Ait-Meddour, R.; Clark, J. H. ; Macquarrie, D. J. *Chem. Commun.*, 2707 (1998)

[240] Kurihara, L. K. ; Suib, S. L. *Chem. Mater.*, **5**, 609 (1993)

[241] Pfaff, G. *Chem. Mater.*, **6**, 58 (1994)

[242] Yan, Y.; Chaudhuri, S. R.; Chen, D. -G.; Sarkar, A. *Chem. Mater.*, **7**, 2007 (1995)

[243] Aylott, J. W.; Richardson, D. J.; Russell, D. A. *Chem. Mater.*, **9**, 2261 (1997)

[244] Goh, C.; Coakley, K. M.; McGehee, M. D. *Nano Lett.*, **5**, 1545 (2005)

[245] Tokumoto, M. S.; Pulcinelli, S. H.; Santilli, C. V.; Briois, V. *J. Phys. Chem. B*, **107**, 568 (2003)

[246] Hench, L. L.; West, J. K. *Chem. Rev.*, **90**, 33 (1990)

[247] Portillo, R.; Lopez, T.; Gomez, R.; Morales, B. A.; Novaro, O. *Langmuir*, **12**, 40, (1996)

[248] Wollman, E. W.; Kang, D.; Frisbie, C. D.; Lorkovic, I. M.; Wrighton, M. S. *J. Am. Chem. Soc.*, **116**, 4395 (1994)

[249] Kumar, A.; Abbott, N. L.; Kim, E.; Biebuyck, H. A.; Whitesides, G. M. *Acc. Chem. Res.*, **28**, 219 (1995)

[250] Hong, S.; Zhu, J.; Mirkin, C. A *Langmuir*, **15**, 7897 (1999)

[251] Elghanian, R.; Storhoff, J. J.; Mucic, R. C.; Letsinger, R. L.; Mirkin, C. A. *Science*, **277**, 1078 (1997)

[252] Broers, A. N. *J. Electrochem. Soc.*, **128**, 166 (1981)

[253] Chen, W.; Ahmed, H. *Appl. Phys. Lett.*, **62**, 1499, (1993)

[254] Gates, B. D.; Xu, Q.; Love, J. C.; Wolfe, D. B.; Whitesides, G. M. *Annu. Rev. Mater. Res.*, **34**, 339 (2004)

[255] Solak, H. H.; *J. Phys. D: Appl. Phys.*, **39**, R171 (2006)

[256] Chen, W.; Ahmed, H. *Appl. Phys. Lett.*, **62**, 1499 (1993)

[257] Kumar, A.; Whitesides, G. M. *Science*, **263**, 60 (1994)

[258] Guo, L. J. *J. Phys. D: Appl. Phys.*, **37**, R123 (2004)

[259] Davis, J. J.; Bagshaw, C. B.; Busuttil, K. L.; Hanyu, Y.; Coleman, K. S. *J. Am. Chem. Soc.*, **128**, 14135 (2006)

[260] Marrian, C. R. K.; Perkins, F. K.; Brandow, S. L.; Koloski, T. S.; Dobisz, E. A.; Calvert, J. M. *App. Phys. Lett.*, **64**, 390 (1994)

[261] Mizutani, W.; Ishida, T.; Tokumoto, H. *Langmuir*, **14**, 7197 (1998)

[262] Sun, S.; Chong, K. S. L.; Leggett, G. J. *J. Am. Chem. Soc.*, **124**, 2414 (2002)

[263] Liu, G. Y.; Xu, S.; Qian, Y. L. *Acc. Chem. Res.*, **33**, 457 (2000)

---

[264] Abbott, N. L.; Folkers, J. P.; Whitesides, G. M. *Science*, **257**, 1380 (1992)

[265] Rozsnyai, L. F.; Wrighton, M. S. *Chem. Mater.*, **8**, 309 (1996)

[266] Burton, Z.; Bhushan, B. *Nano Lett.*, **5**, 1607 (2005)

[267] Sullivan, T. P; Huck, W. T. S. *Eur. J. Org. Chem.*, **11**, 17 (2003)

[268] Petri, D. F. S.; Wenz, G.; Schunk, P.; Schimmel, T. *Langmuir*, **15**, 4520 (1999)

[269] Zhang, Z. J.; Hu, R. S.; Liu, Z. F. *Langmuir*, **16**, 1158 (2000)

[270] Petri, D. F. S.; Siqueira, W.; Schunk, P.; Schimmel, T. *Langmuir*, **15**, 4520 (1999)

[271] Cho, Y.; Ivanisevic, A. *J. Phys. Chem. B*, **108**, 15223 (2004)

[272] Naciri, J.; Fang, J. Y.; Moore, M.; Shenoy, D.; Dulcey, C. S.; Shashidhar, R. *Chem. Mater.*, **12**, 3288 (2000)

[273] Ren, S.; Yang, S.; Zhao, Y. *Langmuir*, **19**, 2763 (2003)

[274] He, H. X.; Zhang, H.; Li, Q. G.; Zhu, T.; Li, S. F. Y.; Liu, Z. F. *Langmuir*, **16**, 3846 (2000)

[275] Freeman, R. G.; Grabar, K. C.; Allison, K. J.; Bright, R. M.; Davis, J. A.; Guthrie, A. P.; Hommer, M. B.; Jackson, M. A.; Smith, P. C.; Walter, D. G.; Natan, M. J. *Science*, **267**, 1629 (1995)

[276] He, L.; Musick, M. D.; Nicewarner, S. R.; Salinas, F. G.; Benkovic, S. J.; Natan, M. J.; Keating, C. D. *J. Am. Chem. Soc*, **122**, 9071 (2000)

[277] Feldheim, D. L.; Keating, C. D. *Chem. Soc. Rev.*, **27**, 1 (1998)

[278] Sato, T.; Hasko, D. G.; Ahmed, H. *J. Vac. Sci. Technol., B*, **15**, 45 (1997)

[279] McConnell, W. P.; Novak, J. P.; Brousseau, L. C., III; Fuierer, R. R.; Tenent, R. C.; Feldheim, D. L. *J. Phys. Chem. B*, **104**, 8925 (2000)

[280] Chen, C-F.; Tzeng, S-D.; Lin, M-H.; Gwo, S. *Langmuir*, **22**, 7819 (2006)

[281] Li, Q.; Zheng, J.; Liu, Z. *Langmuir*, **19**, 166 (2003)

[282] Mendes, P. M.; Jacke, S.; Critchley, K.; Nikitin, K.; Palmer, R. E.; Preece, J. A.; Fitzmaurice, D. *Langmuir*, **20**, 3766 (2004)

[283] Golub, A. A.; Zubenko, A. I.; Zhmud, B. V.; *J. Colloid Interface Sci.*, **179**, 482 (1996)

[284] Taton, K. S.; Guire, P. E. *Colloids Surf. B*, **24**, 123 (2002)

[285] Huang, N. P.; Michel, R.; Voros, J.; Textor, M.; Hofer, R.; Rossi, A.; Elbert, D. L.; Hubbell, J. A.; Spencer, N. D. *Langmuir*, **17**, 489 (2001)

[286] Zhang, F.; Srinivasan, M. P. *Langmuir*, **20**, 2309 (2004)

[287] Zhu, T.; Fu, X.; Mu, T.; Wang, J.; Liu, Z. *Langmuir*, **15**, 5197 (1999)

[288] Heiney, P. A.; Grüneburg, K.; Fang, J.; Dulcey, C.; Shashidhar, R. *Langmuir*, **16**, 2651 (2000)

---

[289] Chang, Y.; Ahn, Y. S.; Hahn, H. T.; Chen, Y. *Langmuir*, **23**, 4112 (2007)

[290] Jung, M.-S.; Jung, S.-O.; Jung, D.-H.; Ko, Y. K.; Jin, Y. W.; Kim, J.; Jung, H. -T. *J. Phys. Chem. B*, **109**, 10584 (2005)

[291] Ramachandran, N.; Hainsworth, E.; Bhullar, B.; Eisenstein, S.; Rosen, B.; Lau, A. Y.; Walter, J. C.; LaBaer, J. *Science*, **305**, 86 (2004)

[292] Avouris, P. *Acc. Chem. Res.*, **35**, 1026 (2002)

[293] Horton Jr., R. C.; Herne, T. M; Myles, D. C. *J. Am. Chem. Soc.*, **119**, 12980 (1997)

[294] Hu, M.; Noda, S.; Okubo, T.; Yamaguchi, Y.; Komiyama, H. *Appl. Surf. Sci.*, **181**, 307 (2001)

[295] Katz, H. E.; Schilling, M. L.; Chidsey, C. E. D.; Putvinski, T. M.; Hutton, R. S. *Chem. Mater.*, **3**, 699 (1991)